A Study of the Interstellar Medium towards the VHE gamma-ray sources HESS J1614-518 and HESS J1616-508

Stephanie Pointon

Thesis submitted for the degree of

Master of Philosophy

in

Physics

at

The University of Adelaide

(Faculty of Science)

School of Physical Sciences

January 14, 2016

Contents

List of Tables

List of Figures

Signed Statement

I certify that this work contains no material which has been accepted for the award of any other degree or diploma in my name, in any university or other tertiary institution and, to the best of my knowledge and belief, contains no material previously published or written by another person, except where due reference has been made in the text. In addition, I certify that no part of this work will, in the future, be used in a submission in my name, for any other degree or diploma in any university or other tertiary institution without the prior approval of the University of Adelaide and where applicable, any partner institution responsible for the joint-award of this degree.

I give consent to this copy of my thesis, when deposited in the University Library, being made available for loan and photocopying, subject to the provisions of the Copyright Act 1968.

I also give permission for the digital version of my thesis to be made available on the web, via the University's digital research repository, the Library Search and also through web search engines, unless permission has been granted by the University to restrict access for a period of time.

SIGNED: ..... DATE: .....

Acknowledgements

I would like to thank my supervisor, Gavin, for his guidance through the past two years. I'd also like to thank Bruce, my co-supervisor, Gary and Roger who were also supportive. A special thanks goes to Fabien, Phoebe, James and Rebecca who were all willing to help and support me. I'd also like to thank the Nanten team, the Mopra CO Survey teams and the MALT-45 survey team for providing me with data. I'd also like to thank the high energy astronomy department for helping me to develop my presentation skills at a number of meetings.

Dedication

I would like to dedicate my thesis to my family, Mum, Dad, Michael, Grandma and Grandad who have provided me with amazing support and truly astronomical quantities of chocolate. Simon has also been wonderfully supportive and has kept me calm during the stressful times. I would not have completed this thesis without this support.

Abstract

One of the most intriguing problems in galactic astronomy is the observation of the highest energy photons. Very high energy (VHE) gamma-ray telescopes such as HESS have located sources of TeV (10^{12} eV) gamma-rays which are not associated with any known objects. Whilst these could be a new type of particle accelerator, it is more likely that they are related to supernova remnants (SNRs), pulsar wind nebula (PWN) or massive stellar regions. They may result from high energy cosmic-ray (CR) interactions with interstellar gas (ISM). This project used new radio data which provided information on molecular clouds to model the production of gamma-rays from CR interactions. The densities of protons in these clouds were used in models to determine if potential particle accelerators surrounding the two HESS sources, HESS J1616-508 and HESS J1614-518 were capable of producing the emission. The potential accelerators surrounding HESS J1616-508 were all found to have insufficient gas within their diffusion radius. Thus, it was not possible for those sources to produce gamma-rays through hadronic interactions despite only requiring modest CR energy budgets compared to that provided from a SNR. The same result was also found for WR 73-1 and PSR J1613-5211 near HESS J1614-518. However, Pismis 22 and WR 74 contained CO RoI CO1, CO2 and CO25 within their diffusion radii. The energy in CRs required for each region to generate the overlapping gamma-ray emission was compared to the available energy if a SNR was assumed to be the accelerator. The required energy was found to be less than the energy available. Thus, WR 74 and Pismis 22 could still generate the hadronic gamma-ray emission from HESS J1614-518.

Chapter 1

Introduction

The TeV Gamma-Ray Sky

The TeV (10^{12} eV) gamma-ray sky has been explored by several telescopes over the past several decades. One dedicated survey is the HESS Galactic Plane Survey (HGPS). This survey initially covered a range of $l = \pm 30^o$ and $b = \pm 3^o$ (The HESS Collaboration, 2006) thus covering the inner portion of the galactic plane of the Southern Milky Way. In later years, the area has increased to cover the region defined by $l = 250^o$ to 65° and $b = \pm 3.5^o$ (The HESS Collaboration, 2009; Carrigan et al., 2013). The analysis of the survey discovered many new gamma-ray sources, many of which are yet to be classified. Figure 1.1 shows the current status of the HGPS.

However, not all sources of gamma-rays are found along the galactic plane. Indeed, many point like sources are seen over the entire sky. These have been attributed to active galactic nuclei (AGN). AGN consist of a super massive black hole which accretes matter and generates jets. These sources contain some of the most energetic processes known in the Universe. However, their extreme distance means that any structural features in the emission cannot be resolved by current instruments. Additionally, most objects in this class belong to the blazar sub classification where the jets are parallel to the observation direction. Other extra-galactic sources of gamma-rays include nearby galaxies, starburst

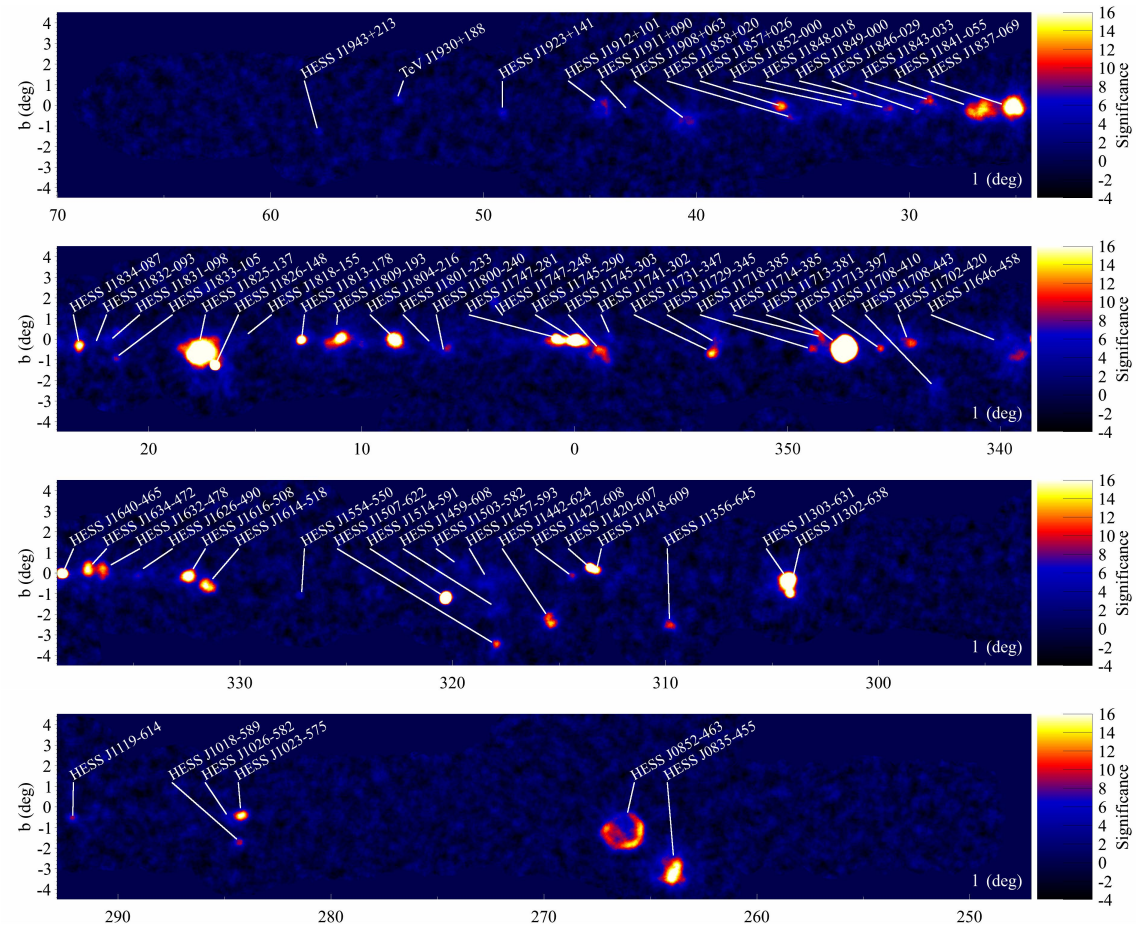

Figure 1.1: The results of the extended HESS galactic plane survey(Carrigan et al., 2013).

galaxies, galaxy clusters, gamma-ray bursts and sources of ultra high-energy (UHE) CRs (Hinton and Hofmann, 2009).

The dominant source of very high-energy (VHE) gamma-rays are pulsar wind nebulae (PWNe) (Carrigan et al., 2013). These sources consist of a powerful pulsar, created by a supernova of a high mass star. A pulsar has intense, rapidly rotating magnetic fields which can accelerate charged particles such as electrons and positrons to very high energies. Sources of charged particles are from the residual charge on the surface of the pulsar or pair-production from gamma-rays near the neutron star. This results in a relativistic wind of electrons and positrons emanating from the pulsar and propagating into the surrounding nebula. The particles can lose energy through Bremsstrahlung radiation and inverse Compton (IC) scattering. At very high energies, particles are more likely to lose proportionally more energy in a single scattering event than at lower energies (Sarazin,

1999). Therefore, for electrons and positrons with high energies, the gamma-ray spectrum will be harder. In addition to gamma-rays, X-ray emission should also be observed. This is due to the presence of strong magnetic fields which the particles spiral around. As they spiral, energy is released as synchrotron radiation. This contribution should decrease with distance from the PWN since the magnetic fields decrease in strength. PWN are very efficient at converting the kinetic energies of the particles into radiation since electrons have a cooling time of 10^3 to 10^4 years in typical magnetic field strengths of $B \approx 10$ to 100 μG (Gunawardhana et al., 2015). In addition, the lifespan of a pulsar is long compared to that of other phenomena such as supernova remnants. These two effects combined, contribute to the fact that PWN gamma-ray associations are more frequent than any other particle accelerator in the galactic plane as shown in Figure 1.2.

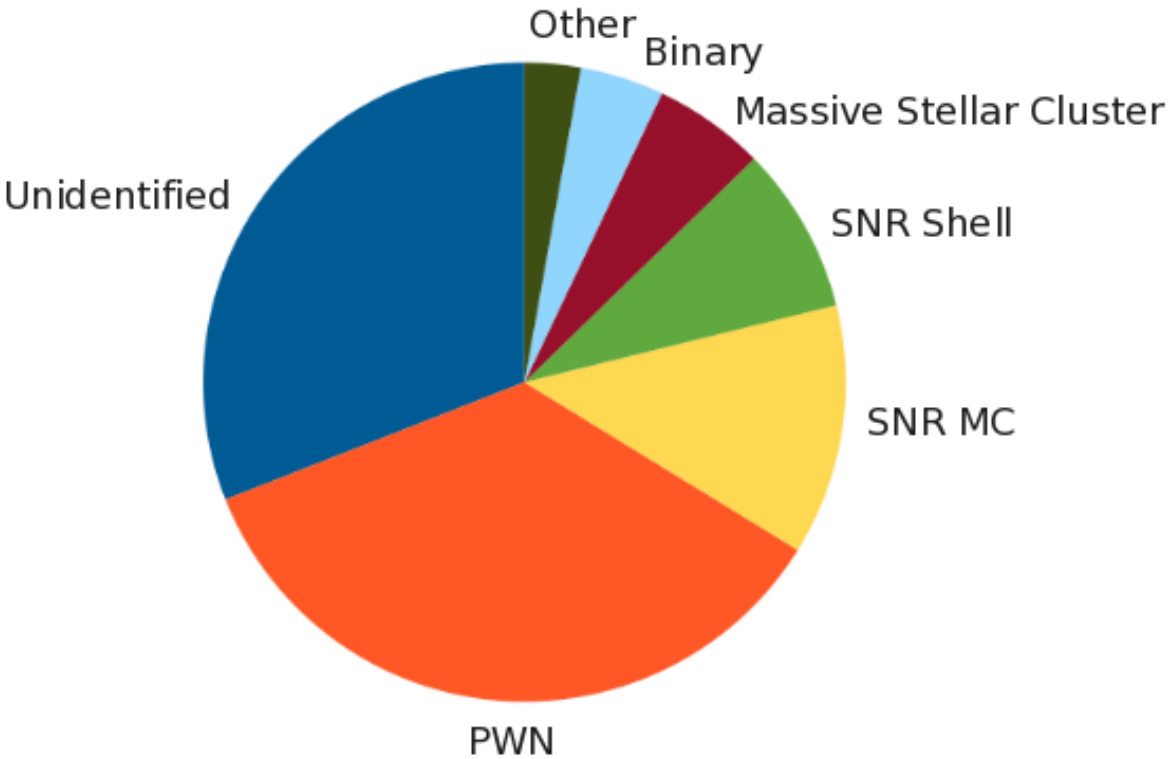

Figure 1.2: The proportion of different particle accelerators which have been associated with HESS TeV emission. The largest categories are PWNe and unidentified or dark accelerators. (Carrigan et al., 2013)

Another galactic source of gamma-rays are supernova remnants (SNR). SNRs are the

product of a supernova, similar to PWN. After a supernova, a SNR shock is formed when the pressure of the ejected matter is balanced by the ambient pressure of interstellar gas. Particles can be further accelerated by crossing the shock front many times until they have sufficient energy to escape. Upon escaping, they can interact with any material outside the shock and release gamma radiation (Fermi, 1954). The shock front or rim of the SNR is usually very bright in gamma-rays. Unlike PWN, there is thought to be a significant hadronic component. Hadrons generally loose energy through collisions with gas atoms and molecules. These collisions have sufficient energies to produce unstable particles such as pions and eta mesons which release gamma-rays in their decay. Secondary leptons are also produced which enhances the electron flux and also suggests that SNR should be a source of neutrinos. The electronic contribution to the emission comes from non-thermal electrons. They also release X-ray emission which has a very similar morphology to the gamma-ray emission. This has lead to suggestions that SNR emission could be accounted for by high energy electrons. Evidence for a hadronic component to the emission would assist theories suggesting that SNR are sources of galactic CR. There are less gamma-ray sources which are classified as SNR than PWNe, suggesting that PWNe phenomena have a longer lifespan (Gabici, 2008).

As discussed, gamma-ray emission is often associated with the aftermath of a massive star. However, it is not only in death that these stars could contribute to gamma-ray emission. Many massive O and B type stars have strong stellar winds with high mass loss rates. Additionally, there is also a tendency for these stars to for in close clusters where interactions between the winds would be possible. While gamma-ray emission from the interaction of stellar winds is possible, few candidate sources have been found(Carrigan et al., 2013). To add to the difficulty, the cluster needs to be checked for PWN or SNR which might also power the emission if it is old enough for stars to have evolved beyond the main sequence.

Dark Accelerators

A significant portion ($\approx 30\%$) of the gamma-ray sources found in the HESS survey have not been classified (Carrigan et al., 2013). Many of these sources do not have obvious counterparts in other wavelengths even when detailed studies are made. These sources are often referred to as dark accelerators since there is no obvious mechanism which accelerates the particles. It has been speculated that they may be an entirely new class of accelerators (Aharonian et al., 2005). However, detailed multiwavelength studies have managed to aid in classification of some previous dark accelerators which suggests that they may be the result of familiar processes in unusual environments.

Difficulty is usually encountered when attempting to classify dark accelerators. Firstly, follow up surveys need to have good sensitivity in order to pick up any faint emission. Additionally, since gamma-ray sources are usually extended, they may contain several plausible candidates which could generate the emission (Acero et al., 2010). Another important factor which is not easily resolved is determining the distance of different emissions towards a source. Within the Galaxy, it is possible to use the Doppler shift of a spectral line to calculate its distance using the Galactic rotation curve (Brand and Blitz, 1993). However, there is some ambiguity involved in this since two solutions for the distance satisfy the conditions. This means, finding emission which corresponds to the distance of the gamma-ray source is difficult.

HESS J1614-518

A currently unclassified source is HESS J1614-518. It was discovered in the initial HESS galactic survey in 2005 and was found to be one of the brighter sources found with a flux at 14% that of the Crab Nebula (The HESS Collaboration, 2006). It is located at a galactic longitude of 331.52^o and a galactic latitude of -0.58^o. However, there is not yet a solid theory on how the gamma emission is produced. The detection of the source was

verified by the CANGAROO-III gamma-ray telescope in 2011 (Mizukami et al., 2011). The morphology of the gamma emission is shown in Figure 1.3. The Figure shows the excess counts of emission above the gamma-ray background.

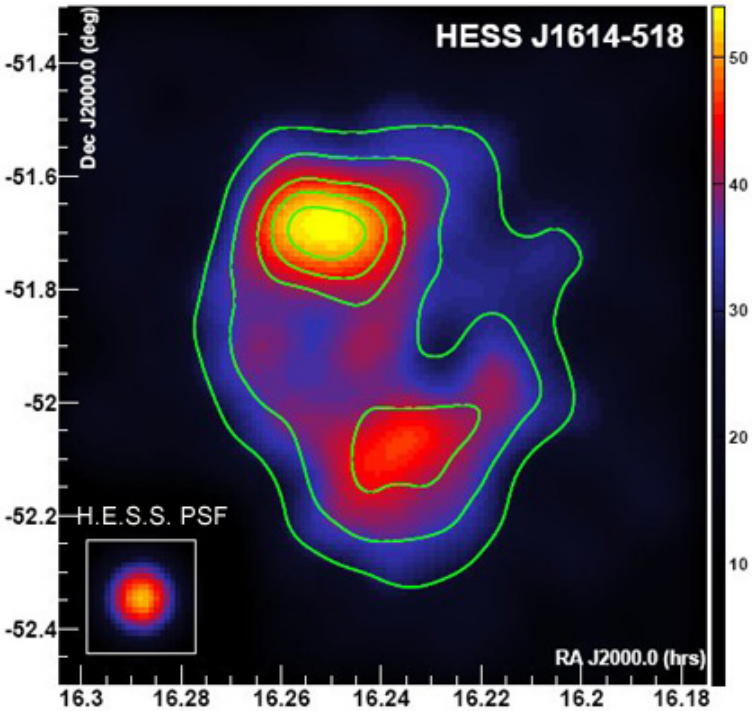

Figure 1.3: The gamma-ray excess counts above background map of the source HESS J1614-518 (Rowell et al., 2008).

HESS J1614-518 is an extended and elongated source characterised by two peaks in the north and the south. Studies have been done to investigate X-ray emission as well as hydrogen gas (Rowell et al., 2008; Lemiere et al., 2005). The gas studies did not find evidence for molecular clouds in the region overlapping the gamma-ray emission. The X-ray emission provided some more positive results. X-ray data was taken from the Suzaku telescope, XMM-Newton and Swift. Swift revealed many point sources while the data from Suzaku and XMM-Newton showed a significant amount of radiation towards the northern peak in gamma-ray emission (Matsumoto et al., 2007). Table 1.1 lists some of the X-ray sources discovered and Figure 1.4 shows their location (Rowell et al., 2008). Several other sources are also listed. These include pulsars, a Wolf-Rayet (WR) star, an open star cluster (Pismis 22) , an X-ray binary system and the Ant planetary nebula.

Object	d [kpc]	L [erg s^{-1}]	[1] $L_{\mathrm{HESSJ1614-518}}$ [erg s^{-1}]
Pismis 22 (Open cluster)[2]	1.0	2.0×10^{36}	4.1×10^{33}
WR 74[2]	4.4	2.0×10^{37}	8.0×10^{34}
4U 1608−52 (LMXRB)9[3]	3.6	2.0×10^{37}	5.4×10^{34}
PSR J1611-5209[4]	3.3	3.4×10^{34}	4.5×10^{34}
PSR J1612-5136	18.2	1.3×10^{33}	1.4×10^{36}
PSR J1613-5211	6.1	7.9×10^{33}	1.5×10^{35}
PSR J1614-5144	9.6	8.1×10^{31}	3.8×10^{35}
PSR J1616-5208	7.4	1.1×10^{33}	2.3×10^{35}
Ant Nebula (RCW 101)	2.7	1.0×10^{38}	3.0×10^{34}
1. EXMS B1609−517			
2. 1RXS J161319.8−514329			
3. *Swift* src 2		†7.9×10^{32}	
4. 1RXS J161340.2−514436			
5. *Swift* src 3 HD145542			
6. *Swift* src 1		†6.5×10^{32}	
7. *Swift* src 4			
8. 1RXS J161431.4−520642			
9. 1RXS J161435.5−513928			
10. *Swift* src 5 HD145703			
11. *Swift* src 6			
Suzaku XIS Src A		‡6.0×10^{31}	4.1×10^{33}
Suzaku XIS Src B		‡4.0×10^{31}	4.1×10^{33}
Suzaku XIS Src C HD145703			

Table 1.1: A list of many of the possible sources of the gamma-ray emission (Rowell et al., 2008).
1. Luminosity of J1614-518 at the object's distance.
2. The luminosity is the kinetic energy of the stellar wind assuming at 20% conversion.
3. The luminosity is the Eddington luminosity with a 10% conversion.
4. Luminosity is the spin down power of the pulsar.

The luminosity of the sources in gamma-rays was found using Equation 1.1:

$$L = 4\pi d^2 F_{\mathrm{TeV}} \tag{1.1}$$

where d is the distance between the object and the Earth. While there are many sources contained with the gamma-ray emission region, a number of them have been excluded as possible sources including the pulsars. A few pulsars are located near the peaks in the gamma-ray emission. However, they do not have a sufficient luminosity to power the gamma-ray emission. The only pulsar possibly capable of producing the emission is PSR J1611-5209. This has been excluded due to the large distance between it and the gamma-ray emission. The same reasoning has been applied to the WR star, the Ant nebula and the X-ray binary.

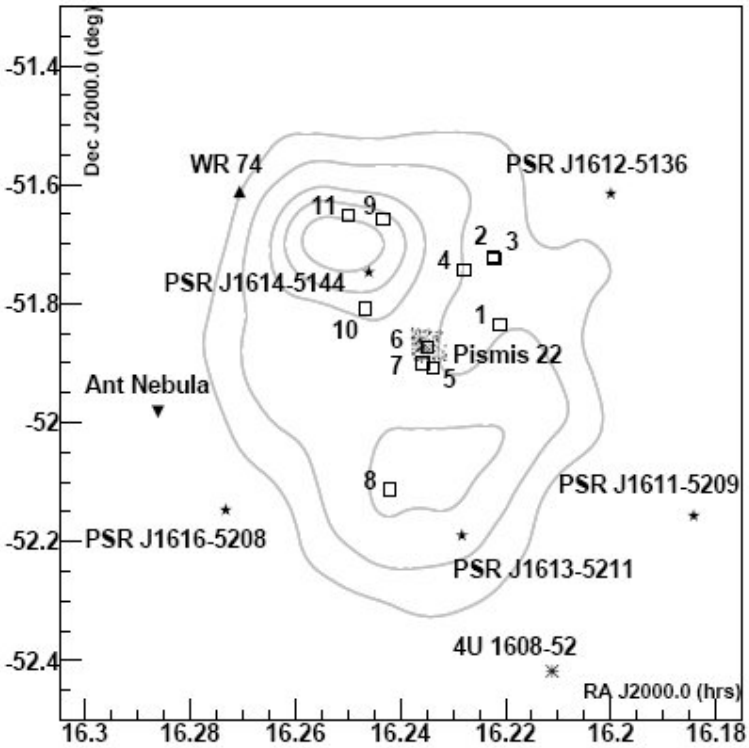

Figure 1.4: A plot of the contours of HESS J1614-518 with the sources listed in the previous table shown (Rowell et al., 2008). Note that the unfilled squares are Swift X-ray sources.

The Swift X-ray sources are generally located in the northern section of the emission. A number are centred on the open cluster Pismis 22. Analysis of the cluster showed that the cluster had an age of 40 ± 15 Myr (Piatti et al., 2000). This indicates that Pismis 22 is old enough to have stars which may have evolved past the main sequence. It has been suggested that the cluster is responsible for the gamma-ray emissions since it is estimated that only 10 B type or 2 O type stars would produce sufficient stellar wind to produce the emission (Rowell et al., 2008). Another possible alternative is that the cluster contains a SNR or a pulsar which has not yet been identified. A later X-ray study with Suzaku did find an X-ray source which was positionally coincident with the Pismis 22 cluster (Sakai et al., 2011). However, they suggest that the two objects are not associated since the predicted distances do not agree. Additionally, they stated that the X-ray emission could not be described by models of stellar winds from O and B type stars.

The only optical study of Pismis 22 did not include an individual spectral analysis of all

the stars within the cluster (Piatti et al., 2000). Additionally, no complex modelling of the region has been undertaken in order to understand how the cluster could generate the gamma-ray emission. This is hindered due to the lack of information about the gas morphology in the region. To present the cluster as a reasonable candidate for the production of the gamma-ray emission, this is required.

HESS J1614-518 is a very mysterious dark accelerator. Various multiwavelength studies have suggested different methods of gamma-ray production but there is no consensus on the nature of the emission. Clearly information is needed regarding the gas morphology of the region to provide some understanding of how the accelerated particles might be interacting to produce gamma-rays. This information could then be used to create a model of the region which could be used as a guide when excluding different possible source candidates.

HESS J1616-508

HESS J1616-508 is another dark accelerator which is located less than a degree away from HESS J1614-518 and was discovered at the same time (Aharonian et al., 2005). Classification of this source has not been as difficult. However, there are still some issues which have not yet been addressed. The source itself is located at a galactic longitude of 332.39^o and a galactic latitude of -0.138^o (The HESS Collaboration, 2006). It is also reasonably extended with an angular diameter of 0.14^o. However, unlike HESS J1614-518, it is approximately spherical. It has a gamma-ray flux of 19% of the Crab nebula. The excess counts of gamma-ray emission above the background of HESS J1616-508 are shown in Figure 1.5 (The HESS Collaboration, 2006). It is clear that no currently recognised source coincides with the center of the gamma-ray emissions. However, this does not necessarily mean that any of these sources could not be generating emission which is offset to its position (Landi et al., 2007). The SNRs, despite having extended X-ray emission are not thought to generate the gamma-ray emission due to their large displacement from

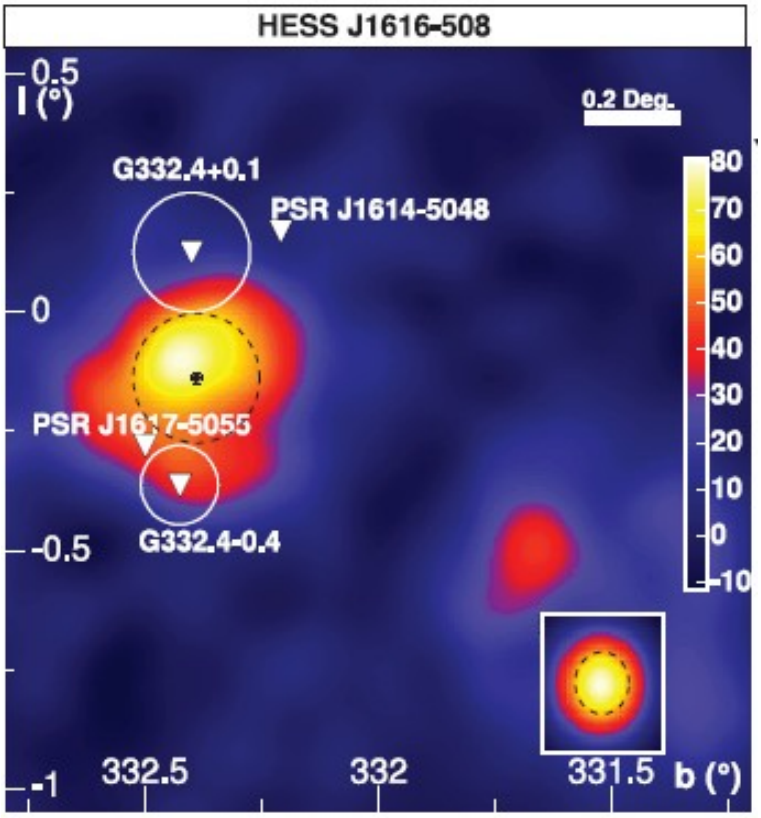

Figure 1.5: An excess counts map of the gamma-ray source HESS J1616-508 (The HESS Collaboration, 2006). The white triangles mark the positions of pulsars PSR J1614-5048 and PSR J1617-5055 as well as SNRs G332.4-0.4 and G332.4+0.1. The SNR are also shown by a white circle which represents their diameter.

HESS J1616-508. This is also the case for the pulsar PSR J1614-5048 (Kargaltsev et al., 2009).

However, it has been suggested that the pulsar PSR J1617-5055 is responsible for the emission since the spin-down power is sufficient to power the level of emission seen from HESS J1616-508 (Landi et al., 2007; Acero et al., 2013). Although the pulsar is offset from the center of the emission, it is still consistent with other PWN associations with HESS TeV sources (Landi et al., 2007). The pulsar is also very bright in hard X-rays as shown in Figure 1.6. The data from the MECS instrument on board the BeppoSAX telescope clearly shows that the PSR J1617-5505 is the main source of X-rays in the region whilst little emission is detected towards HESS J1616-508 (Landi et al., 2007). This is typical of VHE gamma-ray sources where the lower energy particles do not have sufficient energy to diffuse the same distance as the more energetic particles. A survey

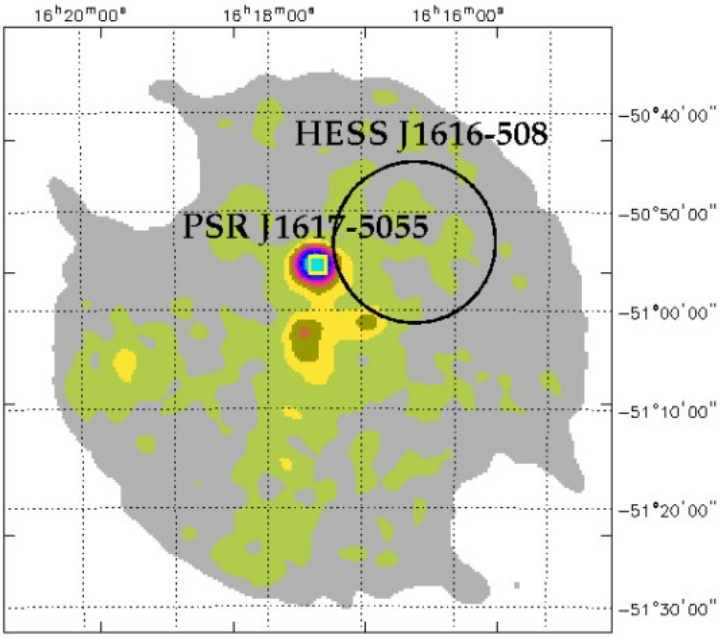

Figure 1.6: The 4-10 keV X-ray emission in the region of HESS J1616-508 observed by the MECS instrument on board the BeppoSAX telescope (Landi et al., 2007).

which used the Chandra X-ray telescope also found that the pulsar was bright in X-rays. They discovered that there was a diffuse nebula surrounding the pulsar which means it could be classified as a PWN (Kargaltsev et al., 2009). The emission detected by the Chandra telescope is shown in Figure 1.7. In general, PWN which are offset from the

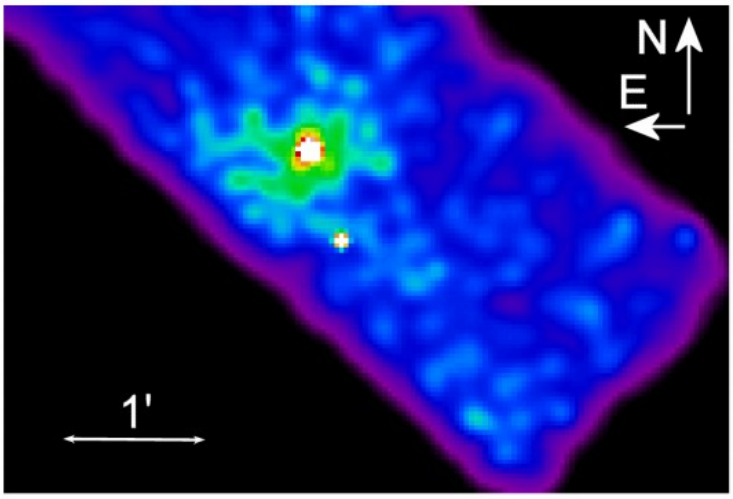

Figure 1.7: Chandra observations of PSR J1617-5055 for energies between 2-8 keV (Kargaltsev et al., 2009). The central white point is the pulsar.

gamma-ray emission have an extension of their X-ray nebula which is directed towards

the peak of the gamma-ray emission (Kargaltsev et al., 2009). However, the Chandra survey found evidence of an X-ray extension towards HESS J1616-518. This lead to the conclusion that PSR J1617-5055 was not entirely responsible for the gamma-ray emission. The study does go on to present a faint, possibly extended X-ray source near the center of the gamma-ray emission. It is also found that there is some diffuse radio emission and an infra-red point source located near the center of HESS J1616-508. The conclusion of the study using Chandra data was that the gamma-ray emission could be associated with the radio and infra-red emission. It was suggested that a SNR or a star forming region could be responsible. It is still possible that some of the emission may be due to the pulsar (Kargaltsev et al., 2009).

The gamma-ray source HESS J1616-508 is an interesting dark accelerator. While it has three possible sources surrounding it, there is not sufficient evidence to suggest that any single one is the cause of the emission. The SNRs in particular are located too far away from the center of the emission. It has been suggested that the southern pulsar may contribute to the emission. However, similarly to the SNRs, it is displaced some distance from HESS J1616-508 and lacks features normally associated with offset PWN.

Summary

The two gamma-ray sources HESS J1614-518 and HESS J1616-508 have been studied in X-rays. However there is a lack of information about the interaction of the interstellar medium (ISM) with potential particle accelerators. Since CR-ISM interactions arise from the collision of VHE CRs on the ISM, probing the gas towards the HESS sources can assist in determining if the emission is from CRs or high energy electrons. Previously, studying the ISM could be done using the Dame CO Survey which has a resolution of $8.5'$ (Dame et al., 2001). Recently, the galactic plane has been observed by the Nanten telescope in Chile and the Mopra telescope in Australia in an effort to produce high resolution maps of CO. The Mopra survey has an angular resolution of $30''$ while Nanten

has an angular resolution of 2.6′. This can be used together with the Southern Galactic Plane Survey (SGPS) of HI, the MALT-45 Survey of CS and additional Mopra 7 mm and 12 mm observations to build a complete understanding of the ISM. The information obtained from this higher resolution data can the be used to probe the possibility of a hadronic origin of either of the two gamma-ray sources using diffusion calculations and a model of the conversion of CRs into gamma-rays.

Chapter 2

The production of VHE gamma-rays and their detection with the HESS telescopes

It is only since the 1980s that studies into the very highest energy processes in the Universe have been possible. The gamma-ray band of the electromagnetic spectrum has been largely unexplored until HESS completed its first galactic plane survey. Since then, many gamma-ray sources have been discovered but many have no obvious counterpart, earning them the title of dark accelerators. Current theory suggests that the highest energy photons are produced by interactions of cosmic ray (CR) protons and electrons interacting with matter, photons and magnetic fields. This chapter discusses the formation of high energy gamma-rays. A brief section follows on the acceleration of cosmic-rays (CRs) by astronomical processes.

2.1 Gamma-ray Astronomy

Gamma-rays are produced when highly energetic charged particles interact with radiation or matter. The emission is often classed into two varieties: hadronic and leptonic. The hadronic component is due to accelerated protons where much of their energy is

lost through interactions with matter. The main interaction through which the protons lose energy and gamma-rays are produced, is the collision of an accelerated proton with a comparatively stationary nucleus of a hydrogen atom. The most important interaction here is the creation of pions, which quickly decay to gamma-ray photons. The leptonic processes are due to electrons either interacting with ambient photons and upscattering them through the Inverse Compton effect or interacting with matter and releasing Bremsstrahlung radiation. Gamma-ray sources which show evidence for hadronic gamma-rays or Bremsstrahlung radiation, have to have some ambient interstellar gas with which the accelerated particles can interact. Thus, gamma-ray astronomy is often used as a tool to understand how CRs are produced. Multi-wavelength studies of gamma-ray sources are very important in order to describe the morphology of the gas which the CRs could be interacting with (Hinton and Hofmann, 2009).

Observing Gamma-Rays on the Ground

Ground-based gamma-ray astronomy is a relatively new field which shows much promise in developing understanding of the highest energy interactions in the universe. Gamma-ray detection can be done using two different types of telescope. The first type, named Imaging Atmospheric Cherenkov Telescopes (IACTs) use large multi-faceted parabolic or spherical mirrors to focus the Cherenkov light emitted by particles to an array of photomultiplier tubes. The track of Cherenkov light can be used to find the initial direction and energy of the gamma-ray. Due to the low flux of Cherenkov emission, the photomultiplier tubes are very sensitive and can only be operated on moonless nights. The first telescope of this type was the Whipple telescope which only used one telescope (Quinn et al., 1996). Modern telescopes use arrays of IACTs working together to achieve better angular resolutions and CR background rejections. For example, HESS was recently upgraded from four to five IACTs to achieve an energy threshold of 30 GeV (The HESS Collaboration, 2012). A future gamma-ray telescope, the Cherenkov Telescope Array, (CTA) will use over 100

IACTs located in Chile and La Palma, Spain to achieve sub arc-minute resolutions. There is another type of gamma-ray telescope named Extensive Air Shower (EAS) arrays. An example is the High-Altitude Water Cherenkov (HAWC) gamma-ray observatory, which detects the products of the atmospheric cascade caused by the gamma-ray. Whilst EAS arrays have poorer resolution and a higher threshold energy than IACTs, they can operate continuously with the additional advantage of a large field of view.

2.2 Production of TeV Gamma-Rays

High energy CRs and electrons are theorised to produce TeV gamma-rays upon interactions with matter and fields. There are four primary methods which are inverse Compton scattering, synchrotron radiation, Bremsstrahlung and proton-proton (CR-ISM) interactions. Inverse Compton scattering, synchrotron radiation and Bremsstrahlung are leptonic processes where high energy electrons interact with photons, magnetic fields and matter respectively. High energy hadrons form gamma-rays primarily through collisions with other hadrons which leads to the production of pions and their subsequent decay into gamma-rays.

2.2.1 Proton-Proton (or CR-ISM) Collisions

The hadronic mechanism for gamma-ray production occurs when a high energy proton collides with ISM matter. The collision, which is often with another proton, results in the production of pions provided there is enough energy released. The interaction's preferred pathway is to a neutral pion which then decays into two gamma-ray photons. However, it is also possible for a negative or positive pion to form. These decay into muons, neutrinos, electrons and their anti-matter components. Gamma-rays can be produced by the decays of these secondary particles or they can interact through leptonic processes described previously.

During neutral pion decay, a comic ray proton collides with a stationary proton. The

energy in the interaction then has to be sufficient to form a neutral pion. Since the particle is unstable, it quickly decays into two gamma-rays which each have equal energy in the rest frame of the pion. As the energy in the interaction is lost to the production of an additional particle, the collision is inelastic. The interaction is shown in Figure 2.1.

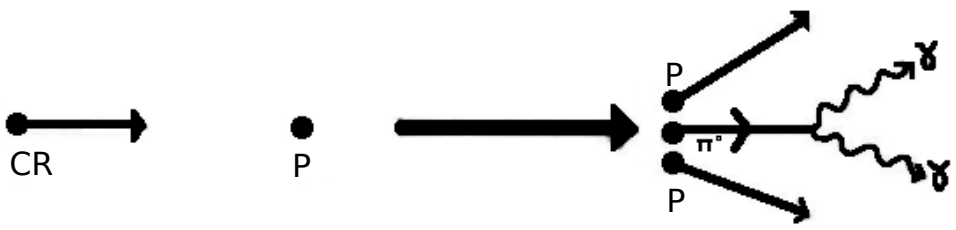

Figure 2.1: Neutral Pion and gamma-ray production from proton collision. The CR protons is incident on the ISM proton. The interaction has sufficient energy to produce a neutral pion which quickly decays into two gamma-rays.

The threshold energy, E_{th}, of the interaction is the minimum amount of energy required for the neutral pion to be created. This is given by the energy of the particles in the center of mass frame where all of the three particles are at rest.

$$E_{th} = (2m_p c^2 + m_{\pi_o} c^2)^2 = 4.044 \text{ GeV}^2 \tag{2.1}$$

The rest mass of the proton is m_p and the rest mass energy of the neutral pion is m_{π_o} while c is the speed of light. The threshold energy of the interaction can then be used to derive the minimum energy that a CR proton would need in order to be able to produce a neutral pion. The result of the derivation (see appendix A) is that the proton must have an energy $E_p > 1.218$ GeV.

Neutral pions produced by the interaction will have a range of energies from only their rest mass to being highly relativistic. Thus, the treatment of the pion decay also lies within the relativistic regime. The production spectrum of the gamma-ray photons resulting from the decay of neutral pions can be derived by using conservation of 4-momentum to

find the power and hence energy emitted in an interaction. The derivation is shown in full in appendix A. Of more interest is the gamma-ray flux, Φ_γ. This is normally calculated numerically but it is known to be dependent on the density of the ISM and the cosmic ray energy spectrum (Aharonian et al., 1994; Aharonian, 1991). The flux of gamma-rays from dense molecular clouds in SNR is given by:

$$\Phi_\gamma(\geq E) = f_\alpha \times 10^{-10} \left(\frac{E}{1 \text{ TeV}}\right)^{-\alpha+1} A \ cm^{-2}s^{-1} \tag{2.2}$$

where:

$$A = \theta \left(\frac{E_{SN}}{10^{51} erg}\right) \left(\frac{d}{1 \ kpc}\right)^{-2} \left(\frac{n}{1 \ cm^{-3}}\right) \tag{2.3}$$

and n is the density of protons, d is the distance to the source, θ is the fraction of the SN energy, E_{SN} available for CRs. The parameter f_α takes on values $f_\alpha \approx 0.9;\ 0.43$ and 0.19 for $\alpha = 2.1; 2.2$ and 2.3 (Aharonian et al., 1994). For high energy CRs which propagate through giant molecular clouds, the flux of gamma-rays can be given by:

$$\Phi(\geq E_\gamma) = 2.85 \times 10^{-13} E^{-1.6} \left(\frac{M_5}{d_{kpc}^2}\right) k \ cm^{-2}s^{-1} \tag{2.4}$$

where M_5 is the mass of the cloud in unit of $10^5 M_\odot$, d_{kpc} is the distance to the cloud and $k = w_{CR}/w_\odot$ where w_{CR} is the energy density of CRs at the cloud and $w_\odot$ is the energy density of CRs in the solar system (Aharonian, 1991).

The density can be obtained using radio spectral lines such as CO and HI. Additionally, if the spectrum of CRs is well described by a power law then so to are the spectra of the neutral pions and the gamma-rays. The spectrum of gamma-rays produced from CR-ISM interactions depends on the model which is used. The model used in this study is further described in Chapter 6.

In addition to neutral pions, charged pions can also be produced in CR-ISM interactions. The first step in their decay results in the production of muons and neutrinos. The muons then go on to decay into electrons or positrons and more neutrinos. The neutrinos can

then be detected by telescopes such as IceCube, located in Antarctica. The secondary electrons and positrons can then go on and interact to produce gamma-rays through Inverse Compton scattering.

2.2.2 Inverse Compton Scattering

High energy electrons can collide with ambient photon fields such as the cosmic microwave background (CMB). In this interaction, the electron can pass energy to the photon resulting in an up-scatter event as shown in Figure 2.2. The energy passed on by the electron is often sufficient to give the photon energies in the TeV range.

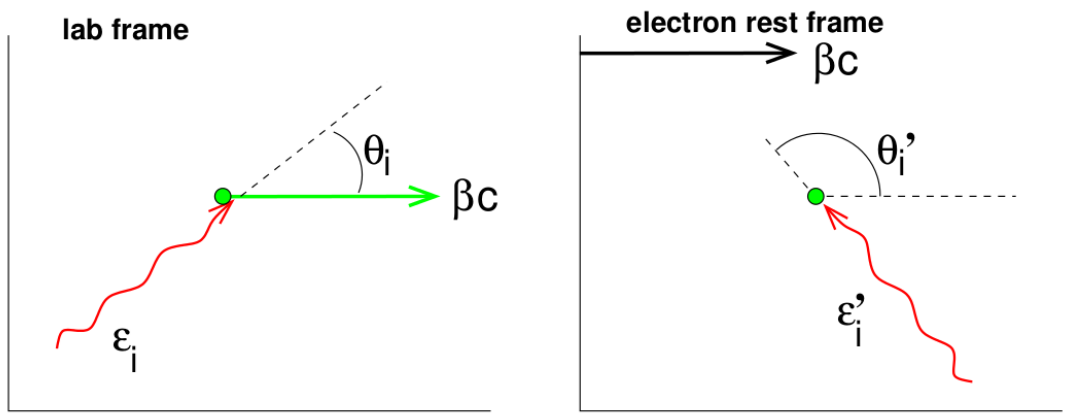

Figure 2.2: A schematic of the Inverse Compton process. (Protheroe)

The spectrum of gamma-rays resulting from the inverse Compton process can be derived using momentum conservation and Lorentz transformations to find the energy spectrum of a population of photons after interactions with a population of electrons.

The energy loss rate of electrons of energy $E_e$for inverse Compton scattering is given in Equation 2.5:

$$\frac{dE_e}{dt} \approx -\frac{4}{3} U_{rad} \sigma_t c \gamma^2 \tag{2.5}$$

where σ_t is the cross-section of the interaction and γ is the Lorentz factor for relativistic electrons. The energy density of radiation, U_{Rad}, is highly dependent on the environment. However, the cosmic microwave background has $U_{rad} = 0.25$ eV cm^{-3}. If it is assumed that the energy spectrum of the electrons is defined by a power law, then the spectrum

of photons is also a power law.

Inverse-Compton scattering events are particularly important in understanding pulsar wind nebulae (PWN) where there are large populations of high energy electrons. It also plays a role in extragalactic gamma-ray sources such as active galactic nuclei (AGN).

2.2.3 Synchrotron Radiation

Synchrotron radiation is normally emitted when a relativistic electron encounters a magnetic field. Provided the electron has a component of velocity perpendicular to the direction of the magnetic field lines, it will undergo circular or helical motion. The acceleration that results from this motion requires that the electron emit radiation.

The energy lost by a population of electrons due to synchrotron effects can then be derived using the Lorentz force to find the acceleration of the electrons which can then be used to find the average power radiated by the electrons. The energy loss rate of electrons with energy E_e is shown in Equation 2.6:

$$\frac{dE_e}{dt} = -\frac{4}{3}\sigma_T c U_B \beta^2 \gamma^2 \tag{2.6}$$

where σ_T is the cross-section of the interaction, β and γ are the Lorentz factors for the relativistic electron and the energy density is given by $U_B = B^2/8\pi$ where B is the magnetic field strength.

Similarly to Inverse Compton processes, the energy spectrum of synchrotron emission is described by a power law provided that the initial electron energy spectrum takes the form of a power law.

Photons emitted by synchrotron emission are often observed at X-ray energies. In some cases, these photons can later be scattered by the electron that emitted them through the inverse-Compton method. Such a process is known as synchrotron self-Compton. Thus, by increasing the energy of the photons, the spectrum of the source does not drop off as expected at higher energies. A shallow drop of rate could indicate the presence of several

regions in the object of interest where self-absorption takes place.

2.2.4 Relativistic Bremsstrahlung

Bremsstrahlung radiation is emitted when a charged particle scatters off of another heavier particle. The change in direction and energy in the interaction releases gamma-rays. In space, the interaction typically involves a high energy electron scattering off interstellar nuclei. The energy loss rate of electrons in Bremsstrahlung interactions has to be considered from a relativistic point of view. The derivation begins by considering the electric and magnetic fields which result from the charge dipole. This can be used to calculate the power emitted which can be converted into the energy lost in an interaction through the use of Fourier theory. The final result is that the energy loss rats of electrons is given by Equation 2.7

$$\frac{dE_e}{dt} = -\frac{n_z Z(Z+1.3)e^6 E_e}{16\pi^3 \hbar \epsilon_o^3 c^4 m_e^2}\left[\ln\left(\frac{183}{Z^{1/3}}\right) + \frac{1}{8}\right] \tag{2.7}$$

where n_z is the number density of interstellar particles with charge Ze, E_e is the energy of an electron and m_e is the mass of the electron. Thus, is it is clear that the energy lost through Bremsstrahlung radiation is proportional to the density of ISM particles, similar to the interaction rate of CR-ISM collisions.

2.3 What are CRs?

Throughout history, astronomy has mainly been performed through the observation of visible light. Recent advances in technology have expanded this view to cover nearly the entire electromagnetic spectrum. However, photons are not the only particle which carries information about the Universe to us. Charged particles such as protons, electrons and nuclei can be accelerated up to very high energies in violent environments where there are intense magnetic fields. As they disperse throughout the universe, they interact with magnetic fields and matter. Unfortunately these interactions often mean that in all but the very highest energy cases, the original direction of the CRs is lost. The presence

of low energy CRs can be inferred from observations of gamma-rays and X-rays. Thus, complementary observations with gamma-ray telescopes such as HESS are vital if the properties of low energy CRs such as their density throughout the Galaxy are to be understood

The energy range of CRs spans from 10^8 eV to 10^{21} eV (Bhattacharjee, 2000). The flux follows an inverted relationship with the energy. That is, there is a high flux of low energy CRs which decreases as the energy increases. Intuitively, the highest energy CRs would require extreme conditions for acceleration and hence are very rare. This means that not many have been observed and thus there are large uncertainties at the high energy end of the CR spectra which is seen in Figure 2.3.

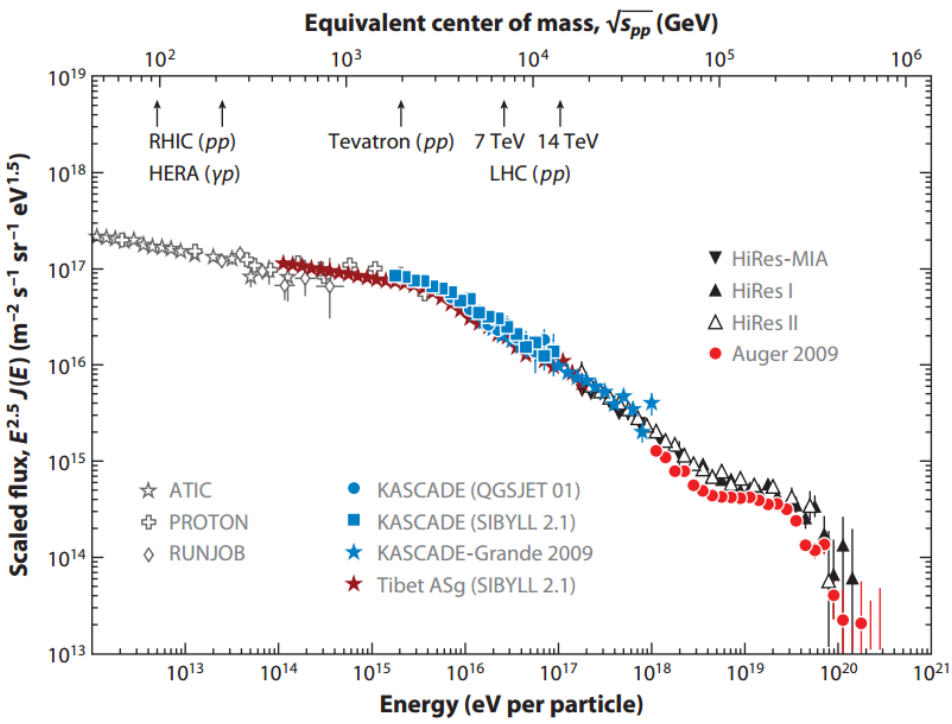

Figure 2.3: The CR energy spectrum spanning the energy range 10^{11} eV to 10^{21} eV (Engel et al., 2011)

It is thought that environments within the Milky Way galaxy are not powerful enough to accelerate particles to above 10^{18} eV (Aloisio et al., 2014). Thus very high energy CRs must come from extragalactic sources. Indeed, the Pierre Auger Observatory, which is the largest ground based CR detector in the world, has found that its results suggest a

correlation between the direction of high energy CRs and active galactic nuclei (AGN) which are the most energetic environments in the universe (Pierre Auger Collaboration, 2007). However, further studies of the correlation have not excluded other possible sources of CRs in favour of AGN (Pierre Auger Collaboration, 2008).

Clearly, CRs are a signpost of astronomical environments where energetic processes are taking place. The energy density of CRs is similar to that of the cosmic microwave background (CMB), starlight, interstellar magnetic fields and gas. Thus knowledge of them is crucial to our understanding of the Universe. Not only are we able to understand environments from the CRs which they produce but their interactions also create gamma-rays and neutrinos. These secondary particles are an important probe of very energetic environments.

2.4 CR Propagation and Transport

The diffusion of CRs and high energy electrons through the Galaxy is a complex problem. To completely model the situation the production rate, escape rate due to energy losses and particle destruction, as well as the diffusion constant need to be known. The distances involved make it difficult to determine any of these parameters with certainty. However, the distance, d that a particle diffuses can be determined using the following equation

$$d = \sqrt{q_i D t} \tag{2.8}$$

where D is the diffusion coefficient, t is the length of time the particle has been travelling and $q_i = 2, 4$ or 6 for one, two or three dimensions respectively. The diffusion of particles is discussed in more detail in Chapter 6.

2.5 CR Acceleration

Since CRs are very high energy charged particles, the theory of how they are accelerated is important to the understanding of the environments where they originate. In general, acceleration is expected to happen in energetic regions where there are abnormally large electric or magnetic field magnitudes.

It is assumed that a CR with a charge of $q = eZ$ and a velocity $\vec{v}$ encounters an electromagnetic field described by $\vec{E}$ and $\vec{B}$. If the Lorentz force is considered, then the maximum change in energy of a particle must be given by 2.9 which is known as the Hillas parameter (Hillas, 1984).

$$\frac{dE}{dt}_{max} = \xi Zec^2 B \tag{2.9}$$

The factor $\xi = v/c$ ensures that the particle cannot be accelerated up to the speed of light. The full derivation of this can be found in appendix A.

This analysis of CR acceleration is very general. It provides an approximation of how a CR may be accelerated but is unspecific as to environments where this might occur. CR acceleration is described in more detail by Fermi's theory of diffusive shock acceleration.

Fermi's Theory of Acceleration

One theory of CR acceleration is that CRs are scattered off ISM clouds (Fermi, 1954). Such clouds have a velocity of approximately 15 km/s. Magnetic fields within the clouds are tied to the particles in the cloud and provide a mechanism for the incoming CRs to scatter. The density within the cloud is low and the cross section of scattering is small, meaning that collisions between the cloud and CRs can be considered to be collisionless. In the laboratory frame, the cloud is travelling with a velocity of v_c. The CR enters the cloud with an energy and momentum of E_1 and p_1 at an angle θ_1 above the cloud's velocity direction. While it is inside the cloud, some scattering events occur and it exits

the cloud with an energy and momentum of E_2 and p_2 at an angle of θ_2 above the cloud's velocity direction.

In the frame of the cloud, the CR enters with an energy and momentum of E'_1 and p'_1 at an angle θ'_1 above the cloud's axis. It exits the cloud with an energy and momentum of E'_2 and p'_2 at an angle of θ'_2 above the clouds axis. The next Figure shows the two reference frames.

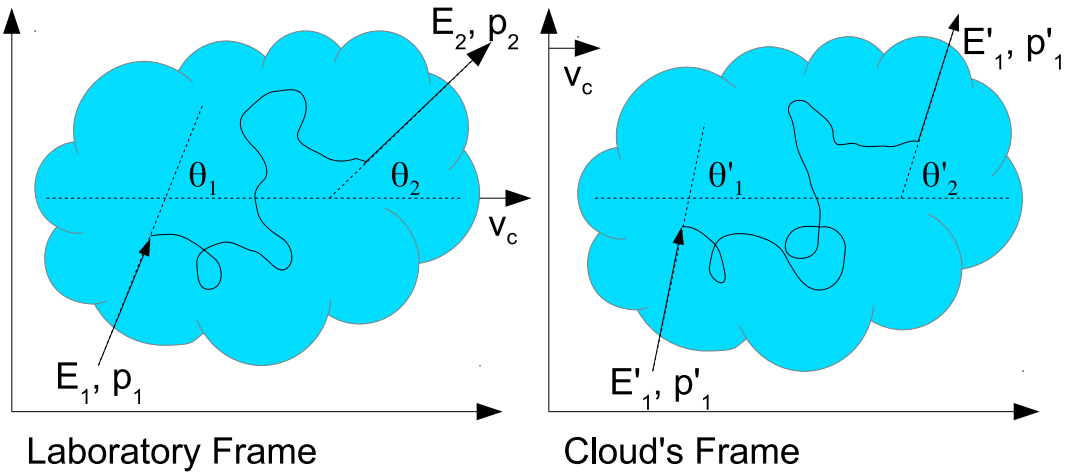

Figure 2.4: The left panel shows the acceleration of a particle from the laboratory or observers frame. The right panel shown the interaction from the stationary frame of the cloud. The particle's properties as described in the text are labelled.

Since the scattering of the CR off the cloud is collisionless, the energy of the particle does not change in the frame of the cloud ($E'_1 = E'_2$). Hence, elastic scattering occurs between the CR and the cloud. Additionally, the direction of the CR is altered in each scattering process within the cloud. Therefore the CR's exit angle is independent of the entry angle. In order to determine the dependence of the CR's final energy and momentum in the laboratory frame, it is necessary to perform two Lorentz transformations (Einstein, 1905). The first transformation takes the initial laboratory conditions of the CR and transforms them to the initial conditions in the cloud's frame. Then the collisionless assumption can be used to find the final conditions in the cloud's frame. The second transform then converts the information back to the laboratory frame. The full derivation of the average fractional change in energy per collision, $\langle \Delta E/E \rangle$ is shown in appendix A. The result is

shown in Equation 2.10 assuming that $\beta_c << 1$ is the Lorentz factor of the CRs.

$$\left\langle \frac{\Delta E}{E} \right\rangle = \frac{4}{3}\beta_c^2 \tag{2.10}$$

Thus, although the average fractional change in energy is positive, the value $\beta_c = \frac{V_c}{c} << 1$. Hence the average gain in energy is very small. This suggests that Fermi's original theory is unlikely to be a significant method by which CRs are accelerated, implying that a modification of the method is needed.

Diffusive Shock Acceleration

Diffusive shock acceleration was suggested as a modification to Fermi's theory and occurs as a shock passes through the local ISM (Bell, 1978). Shocks are formed due to a variety of processes in space. However, the most common would result from a supernova explosion. These explosions, which often result from the death of massive stars, expel matter away at a speed (V_P) higher than the speed of sound (c_s) in the surrounding ISM. This results in a shock wave which propagates out with a velocity V_S while the ISM and the magnetic fields tied to it, pile up in front of the matter ejected from the supernova. The velocity of the shock is dependent on V_P and the ratio of specific heat between the shocked and unshocked gas. Since the supernova progenitor would have released a significant amount of radiation in the explosion, the surrounding medium would be ionised. This means that the ratio of specific heats would be monatomic ($\gamma = \frac{5}{3}$).

Strong ideal shocks in a monatomic ISM gas are expected to have a compression ratio, R, approximately equal to four (Draine and McKee, 1993). The compression ratio is defined as the ratio between the density of the shocked gas to the density of the unshocked gas. The derivation of the diffusive shock acceleration theory considers a particle crossing a shock front. On each side, the particle encounters magnetic irregularities which could include features such as molecular clouds. The particle can interact with the clouds and may cross the shock front many times. Each interaction results in an increase in the

energy of the particle. The full derivation of the diffusive shock acceleration theory is presented in appendix A. The main result is the average fractional change in energy per collision and is presented in Equation 2.11 if it is assumed that the velocity of the shocked medium is much less than the speed of light, $\beta_P << 1$.

$$\left\langle \frac{\Delta E}{E} \right\rangle \approx \frac{4}{3}\beta_P = \frac{4}{3}\frac{V_P}{c} = \frac{4}{3}\left(\frac{R-1}{R}\right)\frac{V_S}{c} = \frac{V_S}{c}, \qquad R = 4 \tag{2.11}$$

Therefore, diffusive shock acceleration is more effective at accelerating CRs than Fermi's original theory, due to a large number of CRs colliding with the clouds in head-on collisions. This results in an average gain in energy per collision proportional to β_P rather than β_P^2.

2.6 Energy Spectrum of Accelerated CRs

In the method of diffusive shock acceleration, particles receive an increase in energy each time they cross the shock front. However, there is a finite probability that the particle will escape from the system each time a crossing occurs. The longer the particle stays in the system, the more energy it gains. CRs which escape, can propagate out into the galaxy and eventually can be detected. The spectrum of a source of CRs from a shock depends on the rate at which particles are able to escape.

Returning to the diffusive shock acceleration theory, it is possible to visualise the system in the shock's frame. The unshocked ISM will move towards the shock with a speed of V_S while the shocked ISM travels in the same direction as the unshocked material, away from the shock at a velocity of $\frac{V_S}{R}$. So there is a flow of CRs in the downstream direction. The probability of a CR escaping (p) in the downstream direction is the ratio of the rate per area which particles escape downstream (R_{loss}) to the rate per area which particle cross to the downstream side of the shock (R_{cross}).

$$R_{loss} = n_{CR}\frac{V_S}{R} \tag{2.12}$$

$$R_{cross} = \frac{1}{4\pi}\int_{-1}^{0} R_{u\to d}(\theta_1)2\pi \; d\cos\theta_1 = \frac{1}{4}n_{CR}v \tag{2.13}$$

$$\Rightarrow p = \frac{R_{loss}}{R_{cross}} = \frac{4V_S}{Rv} \tag{2.14}$$

The probability of returning to the shock once (q) is given by Equation 2.15.

$$q = 1 - p = 1 - \frac{4V_S}{Rv} \tag{2.15}$$

Therefore, the probability of a particle returning and crossing the shock after a number k crossings is:

$$q_k = (1-p)^k \tag{2.16}$$

Hence, for an original population of N_o CRs with an initial energy of E_o, the number and energy of particles after k shock crossings will be:

$$N(\geqslant k) = N_o(1-p)^k \tag{2.17}$$

$$E(k) = E_o\left(1 + \frac{\Delta E}{E}\right)^k \tag{2.18}$$

Thus, the spectrum of CRs generated by diffusive shock acceleration is described by a power law. This has important consequences on the production of gamma-rays since this determines the form of the gamma-ray spectrum.

2.7 Summary

The acceleration and propagation of CRs and high energy electrons through the Galaxy can be traced through observations of X-rays and gamma-rays. Since all but the very highest CRs are bent by magnetic fields, the emission of gamma-rays can indicate regions with a significant population of CRs which are losing energy due to effects such as CR-ISM interactions. High energy electrons can be traced through the Inverse Compton, synchrotron and Bremsstrahlung processes. However, CR-ISM, Inverse Compton and

Bremsstrahlung interactions also are capable of producing VHE gamma-ray emission. The presence of X-ray emission can suggest the presence of high energy electrons losing energy to synchrotron emission. However, determining the origin of gamma-rays, either from CRs or electrons can be impossible to determine based only on gamma-ray or X-ray observations. Thus it is crucial to complement such studies with investigation into the ISM.

Chapter 3

Tracing the Interstellar Medium using Radio Astronomy Techniques

The radio band of the electromagnetic spectrum encompasses the region of wavelengths from sub-millimetre wavelengths up to extremely large wavelengths. Since the 1930s when Karl Jansky first discovered radio emission from the center of the Milky Way galaxy, the field of radio astronomy has expanded rapidly. Detection of radio emission has led to many discoveries of both stable and energetic features ranging from molecular clouds to the centres of galaxies. This is important to gamma-ray astronomy since the formation of gamma-rays from CR-ISM interactions relies on the presence of molecular clouds. This chapter discusses how one can trace the presence of atomic and molecular clouds in space via radio radiation and the information that can be extracted by the detection of such signals.

3.1 Energy Levels of Atoms and Molecules

Atoms and molecules can be described by quantum wave functions meaning that the energy states that they exist in are quantised. It is the presence of discrete energy levels that results in the detection of radio spectral lines. Particles will absorb radiation with wavelengths similar to their energy levels, placing them in a higher energy state, also

known as an excited state. Higher energy states are not stable and after a period of time, the particle will release energy to return to the ground state.

Energy levels are the result of structural changes in the particle. For example, atoms can undergo changes in the alignment of the spins or the energy levels of the nucleons and electrons. Molecules can also have similar properties but can also have vibrational and rotational modes leading to energy transitions. The transitions of nucleon energy states typically require MeV energies while electron transitions typically occur in the visible or ultraviolet (UV) parts of the electromagnetic spectrum which is equivalent to a few eV. Vibrational transitions occur when the positions of the nuclei in the molecule change with respect to the ground state position and result in spectral lines that are generally in the infrared domain. However, a few vibrational transitions are observed by radio telescopes. Rotational transitions occur with changes in the rotation of the molecule. These transitions are generally detectable by radio telescopes. The main rotational modes observed are from linear or symmetric molecules. A molecule which is observed through rotational transitions is known as a rotor.

3.1.1 Atomic Spin-Flip Energy Levels

The most common low energy process by which ISM atoms (in particular, hydrogen), can release radio emission is through fine structure or hyperfine structure splitting that occurs due to the change in the spin alignment of a nucleon and an electron. If the electron has a total spin of $\vec{S}$, orbital momentum of $\vec{L}$ and a total angular momentums of $\vec{J} = \vec{L} + \vec{S}$ then the total number of spin states that it can inhabit is given by $2S + 1$. Given that the proton has a spin of $\vec{I}$, then the total momentum angular momentum of the system is given by $\vec{F} = \vec{I} + \vec{J}$. All of these quantities are quantised and $\vec{F}$ takes on integer values with the degeneracy given by $g_n = 2F + 1$. The lowest state corresponding to $F = 0$ with a degeneracy of $g_0 = 1$ occurs when the spins of the proton and electron are anti-parallel. When $F = 1$ and the degeneracy is $g_1 = 3$ the spins of the electron and proton are aligned. The frequency of the photon that is absorbed or emitted by the transition

between these two states is $\nu = 1.420405751786 \times 10^9$ Hz. The Einstein coefficient given by this frequency is $A_{10} = 2.86888 \times 10^{-15}$ s^{-1} which implies that the spontaneous half life of the transition is $t_{1/2} = 3.49 \times 10^{14}$s. This mean that the transition between the states are classified as forbidden and are not likely to occur often due to spontaneous emission. However, the alignment of the spins between the proton and the electron in the interstellar medium generally change on an order of a few hundred years due to collisions. Thus, a majority of the emission that is observed is due to stimulated emission.

3.1.2 Linear Rotors

Linear rotors include molecules such as carbon monoxide and carbon monosulfide. For a molecule that comprises of i atoms with a total angular momentum of $J = J_x + J_y + J_z = 2J_\perp$, the rotational energy of the molecule is given by:

$$E_{rot} = \frac{J_\perp^2}{2I_\perp} \tag{3.1}$$

where the principal axis is in the x direction. The moment of inertia for the constituent atoms with mass m_i and distance from the axis r_i is given by:

$$I = \sum m_i r_i \tag{3.2}$$

In order to specify this in terms of something that is possible to measure, the energy can be expressed in terms of angular frequency since $J_i = I_i \omega_i$:

$$E_{rot} = \frac{1}{2}\left(I_x\omega_x + I_y\omega_y + I_z\omega_z\right) \tag{3.3}$$

However, the square of the angular momentum can also be expressed in terms of its quantum formulation $J^2 \rightarrow J(J+1)\hbar^2$. This allows the rotational energy to be written in yet another form:

$$E_{rot} = \frac{J(J+1)\hbar^2}{2I} \tag{3.4}$$

A linear rotor has the molecular axis aligned along the line connecting the atoms. The moment of inertia around this axis is negligible while the moment of inertia for the other two axes are equal:

$$I_x = 0;\ I_y = I_z \tag{3.5}$$

$$E_{rot} = \frac{J_\perp}{2I_\perp} \tag{3.6}$$

where $J_\perp$ and $I_\perp$ are the angular momentum and moment of inertia perpendicular to the axis of rotation respectively. If a linear molecule is to absorb or emit a photon of energy ΔE_{rot} with a frequency of $\nu = \Delta E_{rot}/2\pi\hbar$, then the frequency of that transition can be found in terms of the quantum number of the system. The transitions in angular momentum are restricted to $\Delta J \pm 1$ since photons have a spin of 1. If the lower energy state has an angular momentum quantum number of J_L and the upper state has J_U, then the frequency can be found to be:

$$\nu = \frac{\hbar}{2\pi I}(J_L + 1) \tag{3.7}$$

Therefore, a linear rotor has precise frequencies associated with its rotation about the principal axis. Thus detection of the molecule is possible and many transitions are detectable by radio telescopes.

3.1.3 Symmetric Rotor

Molecules which are symmetric rotors are symmetric about one axis while the other two axes are equivalent. An example of such a molecule is ammonia. The moment of inertia for a symmetric rotor follows the following system:

$$I_x = I_y \neq I_z \tag{3.8}$$

Thus, the moment of inertia of the system can be split into components which are perpendicular or parallel to the axis of rotation. That is, $I_\perp = I_x = I_y$ and $I_\parallel = I_z$. The

angular momentum can also be rearranged such that:

$$J_x^2 + J_y^2 = J^2 - J_z^2 \tag{3.9}$$

Thus the rotational energy of the symmetric rotor can be expressed as:

$$E_{rot} = \frac{J_x^2 + J_y^2}{2I_\perp} + \frac{J_z^2}{2I_\parallel} \tag{3.10}$$

$$\Rightarrow E_{rot} = \frac{J^2}{2I_\perp} - \frac{J_z^2}{2I_\perp} + \frac{J_z^2}{2I_\parallel} \tag{3.11}$$

$$\Rightarrow E_{rot} = \frac{J^2}{2I_\perp} + J_z^2\left(\frac{1}{2I_\parallel} - \frac{1}{2I_\perp}\right) \tag{3.12}$$

The quantum numbers for symmetric rotors are given by J and K where K^2 is the eigenvalue for J_z^2 and J^2 is the eigenvalue for $J_x^2 + J_y^2 + J_z^2$. The range of values which the quantum number can take are:

$$J = 0, 1, 2, \ldots \ ; \ K = 0, \pm 1, \pm 2, \ldots \pm J \tag{3.13}$$

Additionally, note that:

$$J^2 \rightarrow J(J+1)\hbar^2 \ ; \ J_z^2 \rightarrow K^2\hbar^2 \tag{3.14}$$

Thus the rotational energy of a symmetric rotor can be expressed in terms of the quantum numbers of the system:

$$E_{rot} = \frac{\hbar^2}{2I_\perp}J(J+1) + \hbar^2 K^2\left(\frac{1}{2I_\parallel} - \frac{1}{2I_\perp}\right) \tag{3.15}$$

In addition to the two quantum numbers already presented, J, the angular momentum and K, the projection of the angular momentum onto the principal axis, there is also the magnetic quantum number M. This can take values in the range of $\pm J$ which means that the degeneracy of a given symmetric rotor energy level is $2J + 1$. Thus, when observing a population of symmetric molecules, the spectral line could be comprised of many different

transitions which have similar energies. Occasionally, there are some symmetric molecules which have some hyperfine structure due to magnetic splitting. This leads to multiple spectral lines being observed within a small frequency range provided the telescope has sufficient frequency resolution and the signal is strong enough.

3.2 Excitation and Critical Density

The process of particles being excited to upper energy levels and then transitioning back to the ground state can be understood through the processes which cause a transition. The particle will be stimulated into either upper or lower levels by ambient emission. For two energy states, E_1 and E_2, the probability of these interactions are B_{12} and B_{21} respectively. The particle can also spontaneously transition down to E_1 with a probability of A_{21} due to the instability of the upper state. Collisions between the particles themselves also result in transitions. The probability of a particle transitioning to higher or lower states is given by the parameters C_{12} and C_{21} respectively. All of these five parameters are known as Einstein coefficients. If the density of particles in the lower state is n_1 and n_2 in the upper state then for a stationary system, the number of particles transitioning to the upper state must be equal to the number transitioning to the lower state. Thus:

$$n_1 \left(B_{12}\bar{U} + C_{12}\right) = n_2 \left(A_{21} + C_{21} + B_{21}\bar{U}\right) \tag{3.16}$$

where $\bar{U}$ is given by the Plank black-body spectrum:

$$\bar{U} = \frac{8\pi h\nu_o^3}{c^3} \frac{1}{\exp\left(\frac{h\nu_o}{kT}\right) - 1} \tag{3.17}$$

where ν_0 is the frequency of the transition and T is the temperature. The spontaneous and stimulated processes are due to radiative effects. Hence the temperature is that of a back-body, T_B. However, collisional processes depend on the kinetic temperature of the gas, T_K. Using this information, an expression for the excitation temperature can be

derived which is shown in Equation 3.18:

$$T_{ex} = T_K \frac{T_B A_{21} + T_o C_{21}}{T_K A_{21} + T_o C_{21}} \tag{3.18}$$

This equation can be evaluated for the two cases discussed previously. When the transitions are driven by radiation processes and there are negligible collisional effects ($A_{21} \gg C_{21}$) then the excitation temperature will tend towards the radiation temperature, i.e. $T_{ex} \rightarrow T_B$. However, when collisional processes dominate ($C_{21} \gg A_{21}$), then the excitation temperature will tend towards the kinetic temperature of the gas ($T_{ex} \rightarrow T_K$). In the case where the probability of decay by spontaneous emission is approximately equal to the probability of a decay occurring due to collisions between particles the critical density (n^*) is defined where:

$$A_{21} \approx C_{21} \approx n^* \langle \sigma v \rangle \tag{3.19}$$

where σ is the cross section of the interaction and v is the velocity of the particles. Thus, the black-body spectrum can only be used to estimate the temperature of the gas when the density is less than the critical density.

3.3 Local Thermodynamic Equilibrium

The simplest model of a population of particles assumes that the system is in local thermodynamic equilibrium (LTE). In this model, it is assumed that the population of particles is in thermodynamic equilibrium. Clearly this is a situation which is not often met in many astrophysical situations. An additional assumption requires that the population distributions of the energy levels follows a Boltzmann distribution. Despite the limitations, assuming that LTE conditions apply means that the observed spectral line can be used to approximate the mass of a gas feature.

For a system with states l and u and a kinetic temperature of T_K, the ratio of the number

densities, n_u and n_l, of the two states is given by:

$$\frac{n_u}{n_l} = \frac{g_u}{g_l} \exp\left(-\frac{h\nu_{u\to l}}{kT_K}\right) \tag{3.20}$$

where g_u and g_l are the statistical weights of the two states and $\nu_{u\to l}$ is the frequency of the transition.

Therefore, if two energy transitions of a molecule are observed then it is possible to determine the temperature of the gas.

3.4 Radiative Transfer

In order to be able to derive some physical properties of gas clouds from their spectral lines, it is necessary to understand the processes of how light is emitted and absorbed as it travels to the observation point on Earth. This next section explains the concept of thermal radiation and uses this to derive the equation of radiative transfer.

3.4.1 Thermal Radiation

Thermal radiation is emitted by a population of particles which is dependent on the kinetic temperature of the system. The radiation emitted by the particles can be approximated by a black body spectrum which is described by Plank's law:

$$B_\nu(\nu, T) = \frac{2h\nu^3}{c^2} \frac{1}{\exp\left(\frac{h\nu}{kT}\right) - 1} \tag{3.21}$$

where T is the temperature of the system, ν is the frequency and k is Boltzmann's constant. Additional properties of the system can be calculated by either integrating or differentiating Plank's law. If Equation 3.21 is integrated over all solid angles and possible frequencies, then the Stefan-Boltzmann law can be derived which describes the flux, F

from a black body at its surface:

$$F = \sigma T^4 \tag{3.22}$$

where σ is the Stefan-Boltzmann constant given by:

$$\sigma = \frac{2k^2\pi^5}{15c^2h^3} = 5.670373 \times 10^{-8}\ \mathrm{Wm^{-2}K^{-4}} \tag{3.23}$$

If the derivative of Plank's law is found, then the wavelength at which the most radiation is emitted can be found. This property is called Wien's displacement law.

$$\lambda_{max} = \frac{b}{T} \tag{3.24}$$

where T is the temperature of the system in Kelvin and $b = 2.8977721 \times 10^{-3}$ m K is known as Wien's displacement constant.

3.4.2 Equation of Radiative Transfer

The equation of radiative transfer describes the absorption of background photons as they encounter particles as well as the emission of more photons as the exited particles fall back to the ground state. A full derivation is presented in appendix A. The result is that for a specific intensity I_ν which travels a length ds the change in intensity per unit length dI_ν/ds is the equation of radiative transfer is given by Equation 3.25:

$$\frac{dI_\nu}{ds} = -\kappa_\nu I_\nu + j_\nu \tag{3.25}$$

where κ_ν is the absorption coefficient and j_ν is the emission coefficient of the radiation released by the particles. Thus, the intensity is reduced by the amount that the particles absorb and increased by the amount that they emit as they transition to the lower state.

3.5 Optical Depth

The optical depth is a measure of how much radiation is absorbed over a certain distance s. It is defined as:

$$\tau_\nu(s) = \int_0^s \kappa_\nu \, ds \tag{3.26}$$

where κ_ν is the absorption coefficient. If the cross-sectional area of the absorbing particles is equal to the total target area, the optical depth is equal to 1. When the optical depth is less than 1, the gas is defined as being optically thin. On the other hand, if the optical depth is much greater than 1 then the gas is optically thick.

Using the definition of optical depth, the equation of radiative transfer can be expressed in term of the optical depth instead of the depth and absorption coefficient.

$$\frac{dI_\nu}{d\tau_\nu} = -I_\nu(\tau_\nu) + S_\nu(\tau_\nu) \tag{3.27}$$

where $S_\nu = \dfrac{j_\nu}{\kappa_\nu}$ is the source function. Using the theory which describes the solution of first order linear differential equations, a solution to the equation of radiative transfer can be found:

$$I_\nu = I_\nu(0)e^{-\tau_\nu} + e^{-\tau_\nu} \int_0^{\tau_\nu} e^{\tau'_\nu} S_\nu(\tau'_\nu) \, d\tau'_\nu \tag{3.28}$$

where $I_\nu(0)$ is the initial intensity of the radiation. When the source function is constant, the integral can be performed. Therefore, provided the optical depth and the source function are known in addition to the intensity measured at Earth it is possible to determine the initial intensity.

3.6 Brightness Temperature

The equation of radiative transfer can be expressed in terms of the brightness temperature. Since many of the gaseous objects of interest in space emit at radio frequencies ($h\nu <<$

kT), Plank's law can be simplified into the Rayleigh-Jeans Law:

$$B_\nu(T_S) \approx \frac{2k\nu^2 T_S}{c^2} \tag{3.29}$$

where T_S is the radiation temperature of the source and ν is the frequency of the transition. The above relation can be used if the source is assumed to be a black body which emits in the radio spectrum. In order to relate the source temperature to the brightness temperature measured by the telescope, the following equation has to be defined where E_u and E_l are the energy levels of the upper and lower states respectively.

$$J_\nu(T) = \left[\exp\left(\frac{E_u - E_L}{kT}\right) - 1\right]^{-1} \tag{3.30}$$

The brightness temperature is then defined in the following way:

$$T_b = \frac{c^2}{2k\nu^2} B_\nu(T_S) = \frac{h\nu}{k} J_\nu(T_S) \tag{3.31}$$

If it is assumed that the source function is constant, then the solution to the radiative transfer equation can be evaluated in terms of the temperatures of the system where T_S is the temperature of the source, T_b is the brightness temperature and T_{bg} is the background radiation temperature:

$$T_b = \frac{h\nu}{k} J_\nu(T_{bg}) e^{-\tau_\nu} + \frac{h\nu}{k} J_\nu(T_S)(1 - e^{-\tau_\nu}) \tag{3.32}$$

In radio astronomy observations, the brightness temperature that is often measured is the excess above the background temperature. Thus the above equation becomes

$$T_b = \frac{h\nu}{k} \left[J_\nu(T_S) - J_\nu(T_{bg})\right] (1 - e^{-\tau_\nu}) \tag{3.33}$$

For cases where the gas is optically thin ($\tau_\nu \gg 1$), the excess brightness temperature becomes

$$T_b = \frac{h\nu}{k}\left[J_\nu(T_S) - J_\nu(T_{bg})\right]\tau_\nu \tag{3.34}$$

For cases where that gas is optically thick ($\tau_\nu >> 1$), the excess brightness temperature becomes

$$T_b = \frac{h\nu}{k}\left[J_\nu(T_S) - J_\nu(T_{bg})\right] \tag{3.35}$$

If the background temperature is negligible in comparison to the source temperature (and hence $T_S \approx T_{ex}$), then the brightness temperature is given by

$$T_b = \frac{h\nu}{k} J_\nu(T_{ex})(1 - e^{-\tau_\nu}) \tag{3.36}$$

3.7 Column Density

The column density of a gas cloud is defined as the number of particles in the cloud per unit area. That is, if the cloud subtends a certain amount of area on the sky, then the column density is the area number density. In astronomy, column density is usually expressed in units of cm^{-2}. The following section derives the column density which requires more than one transition of a particular particle to be observed. The method of calculating the column density when only one transition can be observed is also discussed.

Since the absorption coefficient can be defined in terms of the Einstein coefficients, so to can the optical depth. This is shown in the following equation where ν is the frequency of the transition, A_{ul} is the probability of the particle transitioning spontaneously from the upper state to the lower state, n_u and n_l are the densities of the upper and lower states respectively, g_u and g_l are the statistical weights of the upper and lower states respectively and $\varphi(\nu)$ is the Gaussian function which describes the emission:

$$\tau_\nu = \frac{c^2}{8\pi\nu^2} A_{ul}\left(n_l \frac{g_u}{g_l} - n_u\right)\varphi(\nu)ds \tag{3.37}$$

Since the Boltzmann equation can be expressed as:

$$\frac{n_l g_u}{n_u g_l} = \exp\left(\frac{h\nu_{ul}}{kT_{ul}}\right) \tag{3.38}$$

where T_{ul} is the temperature of the system, it can be substituted into the equation for optical depth:

$$\tau_\nu = \frac{c^2}{8\pi\nu^2} A_{ul} n_u \left[\exp\left(\frac{h\nu_{ul}}{kT_{ul}}\right) - 1\right] \varphi(\nu) ds \tag{3.39}$$

This equation can the be integrated along the line of sight:

$$\tau_\nu = \frac{c^2}{8\pi\nu^2} A_{ul} \int n_u \; ds \left[\exp\left(\frac{h\nu_{ul}}{kT_{ul}}\right) - 1\right] \varphi(\nu) \tag{3.40}$$

The column density of molecules in the upper state is then defined as the areal number density:

$$N_u = \int n_u \; ds \tag{3.41}$$

Hence the optical depth is dependent on the column density of particles in the upper state:

$$\tau_\nu = \frac{c^2}{8\pi\nu^2} A_{ul} N_u \left[\exp\left(\frac{h\nu_{ul}}{kT_{ul}}\right) - 1\right] \varphi(\nu) \tag{3.42}$$

This equation can be substituted into the equation for the brightness temperature when the background temperature is negligible:

$$T_b = \frac{h\nu}{k} J_\nu(T_{ex}) \left(\frac{1 - e^{-\tau_\nu}}{\tau_\nu}\right) \left(\frac{c^2}{8\pi\nu^2} A_{ul} N_u \left[\exp\left(\frac{h\nu_{ul}}{kT_{ul}}\right) - 1\right] \varphi(\nu)\right) \tag{3.43}$$

$$T_b = \frac{hc^2}{8k\pi\nu} A_{ul} N_u \left(\frac{1 - e^{-\tau_\nu}}{\tau_\nu}\right) \varphi(\nu) \tag{3.44}$$

This can be integrated over the width of the line and solved to find the column density of the particles in the upper state:

$$\int_{-\infty}^{\infty} T_b \; d\nu = \frac{\nu}{c} \int_{-\infty}^{\infty} T_b \; dv \tag{3.45}$$

where v is the Doppler velocity:

$$\int_{-\infty}^{\infty} T_b \, d\nu = \frac{hc^3}{8k\pi\nu^2} A_{ul} N_u \left(\frac{1 - e^{-\tau_\nu}}{\tau_\nu} \right) \int_{-\infty}^{\infty} \varphi(\nu) \, d\nu \tag{3.46}$$

$$\Rightarrow N_u = \frac{8k\pi\nu^2}{A_{ul}c^3} \int_{-\infty}^{\infty} T_b \, dv \left(\frac{1 - e^{-\tau_\nu}}{\tau_\nu} \right) \tag{3.47}$$

If the gas is assumed to be optically thin, then the upper state column density can be simplified to:

$$N_u = \frac{8k\pi\nu^2}{A_{ul}c^3} \int_{-\infty}^{\infty} T_b \, dv \tag{3.48}$$

In general, the total column density of the gas, N, is of more interest than the column density of the upper state. For a system of particles with energy levels that are populated according to a Boltzmann distribution with a temperature of T_{ex}, then the following equations apply:

$$N = \frac{N_u}{g_u} \exp\left(\frac{E_u}{kT} \right) Q(T_{ex}) \tag{3.49}$$

where $Q(T_{ex})$ is the partition function given by:

$$Q(T_{ex}) = \sum_i g_i \exp\left(\frac{E_i}{kT_{ex}} \right) \tag{3.50}$$

While this provides a rigorous method with which to calculate the column density, in many cases only one transition of the particle is observed. When this occurs, the column density can be calculated through the use of an X-factor. The column density is then given by:

$$N = X \int_{-\infty}^{\infty} T_b \, dv \tag{3.51}$$

The use of X-factors can introduce large uncertainties into the column density calculation since they are generally calculated only along the galactic plane and from the assumption that the gas is optically thin. An example is X_{CO} which is the X-factor used to determine the column density of molecular hydrogen gas from the integrated intensity of a carbon monoxide spectral line.

It is possible to calculate the column density for both atomic hydrogen, HI, and molecular, H_2. The total column density of hydrogen is then the sum of N_{HI} and N_{H_2}, allowing for an extra proton in the molecular component. Thus the total proton column density is given by:

$$N_p = N_{HI} + 2N_{H_2} \tag{3.52}$$

This can be used to either calculate the column density of protons in a specific area or to produce column density maps of integrated kinematic velocity ranges.

3.7.1 Mass and Density

Column density provides a distance independent measure of the amount of gas in a particular feature. However, it is also useful to know the mass and density. In order to calculate both of these quantities, the distance to the feature needs to be known. Unfortunately, distance measures are not very accurate and hence numbers calculated using this are also very uncertain.

In order to calculate the mass of a gas feature, the area of the cloud needs to be known. Assume a cloud is located at a distance d and is contained within an ellipse with semi-major and semi-minor axes a and b respectively. Observationally, the axes of the ellipse will usually be found initially in degrees. These can be converted into lengths using trigonometric relations and the assumed distance to the region. Then, the area of an ellipse can be found using

$$A = \pi ab \tag{3.53}$$

By multiplying the column density by the area the total number of particles can be found. This is then converted into mass by multiplying by the mass of the individual particle. An additional factor may also be included to account for gas that is not traced by the observed gas. For example, it could be assumed that the gas contains 10% helium. The

total mass of the gas feature is then usually represented in units of solar mass:

$$M = \frac{NAm_f m_{part}}{M_\odot} \tag{3.54}$$

where m_f is the factor which incorporates other untraced gases, m_{part} is the mass of the particle, N is the column density, A is the area and $M_\odot$ is the mass of the Sun.

Once the mass of the gas feature is obtained, the density can be calculated if the volume of the feature is assumed. There is no simple way to obtain the depth of the region. The width of the spectral line cannot be used since there may be turbulence within the feature which causes broadening. Thus, the region which contains the gas is assumed to be an elliptical prism where the depth is assumed to be the same length as the semi-minor axis:

$$V = \pi a b^2 \tag{3.55}$$

Thus, the mass density of the gas is simply the ratio of the calculated mass and the volume:

$$\rho = \frac{M}{V} \tag{3.56}$$

3.8 Gas Tracers

There are many different chemical species of gas in the galaxy, many of which can be detected by radio telescopes. In the next section, some of the more abundant gases are discussed and some of the particulars involving calculating parameters of the gas tracers used in this thesis are mentioned.

3.8.1 Neutral Hydrogen

Hydrogen, the most abundant atom in the Universe consists of only a proton and an electron. Since the density of most gas in the Galaxy is approximately 1 cm^{-3}, hydrogen can exist in its atomic form, HI. Additionally, due to the average photon field in the

Universe having a low temperature of 2.7 K, hydrogen atoms are unlikely to be ionised unless the gas is located in regions of high photon temperature such as the surrounds of massive stars. Highly ionised hydrogen, HII, is thus not a good tracer of large molecular cloud feature especially when the abundance is much lower than HI.

Since the excitation of HI lines requires temperatures greater than 1000 K the main form of emission from HI comes from the interactions between the spin states of the electron and the proton. Since the radiation emitted from this transition has a wavelength of approximately 21 cm, it is often named the 21 cm transition. This interaction emits at a frequency of $\nu = 1.42 \times 10^9$ Hz with an Einstein coefficient of $A_{21} = 2.85 \times 10^{-15}$ s^{-1} (Furlanetto et al., 2006). Thus the half-life of the state for spontaneous emission is $t_{1/2} = 3.5 \times 10^{14}$ s $\approx 1.1 \times 10^7$ years.

This classifies the transition as forbidden and would imply that the radiation is very faint. However, collisions that occur between the hydrogen atoms mean that the spin of the electron can change within the time frame of 400 years. Thus, transitions for the 21 cm transition are dominated by collisional effects. Since other transitions through this effect cannot be observed the column density of HI has to be calculated through the use of an X-factor (Dickey and Lockman, 1990).

$$X_{HI} = 1.823 \times 10^{18} \text{ cm}^2 \text{ K}^{-1} \text{ km}^{-1} \text{ s} \tag{3.57}$$

In the analysis of the gamma-ray sources HESS J1616-508 and HESS J1614-518, HI observations were taken from the publicly available Southern Galactic Plane Survey (SGPS). That survey was completed using a combination of the Australia Telescope Compact Array (ATNF) and the Parks telescope. Refer to section 4.9 for more description of the telescopes used. SGPS data has a beam full width half maximum (FWHM) of 130″ and provides full coverage over both gamma-ray sources. The survey provides both continuum subtracted data cubes and the continuum image. The region covering the two HESS sources contains a number of continuum sources. Whilst modelling by the SGPS team has been done to remove artefacts from the data cube, they are still present in the data.

Additionally, since atomic hydrogen is the most abundant particle in the galaxy, there is a significant amount of emission at any point in the data cube. These two combined effects combined makes characterising the gas surrounding the HESS sources difficult.

3.8.2 Molecular Hydrogen

In some regions the density is sufficient for atomic hydrogen to form molecular hydrogen, H_2. When considering high energy interactions, regions with denser molecular gas are more likely to be a viable target for high energy CRs to produce gamma-rays. Thus, tracing molecular hydrogen is of specific interest. However, molecular clouds only exist at temperatures of the order of 10 K. This is insufficient to raise H_2 to even the first excited state due to the symmetric charge distribution in the molecule. Hence, it is usually impossible to use H_2 to find dense regions of cold gas.

3.8.3 Carbon Monoxide

Carbon monoxide (CO) is the second most abundant molecule in the ISM with a fractional abundance of 10^{-4} (Szűcs et al., 2014). Since the abundance of CO is significantly lower than that of HI, the molecule will also tend to trace regions of higher density and hence, H_2. Unlike H_2, CO has an asymmetric charge distribution which leads to rotational transitions which can be excited at the low temperatures found in molecular clouds. The transition between the J=1 and J=0 states is easily observed using either the Mopra or Nanten telescopes (again, refer to section 4.9 for a description of the telescopes). However, the transition from J=2 to J=1 requires good atmospheric conditions due to absorption by water vapour. The Nanten2 telescope is currently observing the J_{2-1} emission. However, no observations in the study region have yet been made available. The J_{1-0} transition has been observed by both the Nanten galactic survey and the Mopra CO survey (Braiding et al., 2015; Burton et al., 2013) at resolutions of $4'$ (Mizuno and Fukui, 2004) and $33''$ respectively.

Since CO emission is available at high resolution in the region, it is possible to calculate

the mass of molecular gas in any feature. The lack of higher transitions requires the use of the X-factor for CO, X_{CO} which converts the integrated intensity from a CO feature into the column density of molecular hydrogen (Strong et al., 2004):

$$X_{CO} = 1.5 \times 10^{20} \mathrm{cm}^2 \mathrm{K}^{-1} \mathrm{km}^{-1} \mathrm{s} \tag{3.58}$$

The mass of the gas in the region is then calculated by assuming that the atoms of the gas are arranged such that there is 10% helium and molecular hydrogen. Other constituents of the gas are considered to be negligible. This is a reasonable assumption since the abundances of all other molecules are very low. Atomic hydrogen also is less abundant when molecular hydrogen is present. This introduces a factor of 2.4 to account for all of the nuclei, resulting in the mass being described by:

$$\Rightarrow M = 2.4 A N_{H_2} \frac{m_p}{M_\odot} \tag{3.59}$$

where m_p is the mass of a proton. Other isotopes of carbon monoxide are also present in molecular clouds. The most abundant isotope, ^{12}CO, has been described above. However, observations of ^{13}CO, C^{17}O and C^{18}O have been completed by the Mopra telescope. These less abundant isotopologues trace gas in the denser cores of the molecular clouds. The X-factor for ^{13}CO is given by (Simon et al., 2001):

$$X_{^{13}CO} = 4.92 \times 10^{20},\ \mathrm{cm}^2 \mathrm{K}^{-1} \mathrm{km}^{-1} \mathrm{s} \tag{3.60}$$

This can then be used to calculate the mass by using the equation above. This provides a rough comparison of the mass contained within a molecular cloud and its core.

3.8.4 Carbon Monosulfide

Carbon monosulfide (CS) is another linear molecule similar to CO. However, due to the larger charge asymmetry, the molecule can be excited at much lower temperatures. Thus

the wavelength of the light emitted by CS is best observed using 7 mm receivers on the telescopes. The abundance of CS is given by (Frerking et al., 1980):

$$A_{CS} = 1.0 \times 10^{-9} \tag{3.61}$$

This is very low in comparison to gases such as CO. Thus, CS is primarily used to trace the dense cores of molecular clouds.

A CS survey has been completed using ATCA and is called MALT-45 (Jordan et al., 2015). The survey covers the region spanning $\pm 0.5^{o}$ above and below the galactic plane and from $g_b = 335.0^{o}$ to $g_b = 330.0^{o}$. Thus HESS J1616-508 is completely covered by the survey region but only the northern section of HESS J1614-518 has data. In order to have complete coverage of the HESS source, a smaller region was observed across the southern part of HESS J1614-518 using the Mopra radio telescope. This observation was completed at lower resolution and sensitivity than the ATCA data due to time constraints.

The mass contained within a molecular core containing CS can also be calculated and occasionally optical depth calculations can be made. However, due to the low abundance of CS, it can be assumed that in most cases the gas is optically thin and thus the column density can be approximated.

The optical depth can be calculated by solving the equation:

$$R_{CS} = \frac{1 - \exp(-\tau_{CS} X_{CS})}{1 - \exp(-\tau_{CS})} \tag{3.62}$$

where R_{CS} is the ratio between the integrated intensity of the CS and $C^{34}S$ lines and:

$$X_{CS} = \frac{1}{22.5} \tag{3.63}$$

is the terrestrial ratio of CS to $C^{34}S$. Thus, the column density of first state of CS can be calculated:

$$N_{CS1} = \frac{8\pi k \nu^2 \bar{W_{CS}}}{hc^3 A_{10}} \frac{\tau_{CS}}{1 - \exp(-\tau_{CS})} \tag{3.64}$$

where A_{10} is the Einstein coefficient for spontaneous emission from CS and $\bar{W_{CS}}$ is the average integrated intensity of the CS line. Then, the column density of the CS gas was calculated using the equation:

$$N_{CS} = N_{CS1}\left[\frac{g_1}{Q}\exp\left(-\frac{T_1}{T_g}\right)\right]^1 \tag{3.65}$$

where g_1 is the statistical weight of the first excited state, T_g is the temperature of the gas and Q is the partition function. The values for the partition function were approximated using the numbers shown in the next table. The column density of molecular hydrogen

T_g	Q
$[0, 9, 375]$	0.9200
$(9.375, 18.75]$	1.2119
$(18.75, 37.5]$	1.5084
≥ 37.5	1.8072

could then be calculated using

$$N_{H_2} = \frac{N_{CS}}{A_{CS}} \tag{3.66}$$

where A_{CS} is the abundance of galactic CS. The mass of molecular gas can then be calculated using the equation described in the section on CO.

3.8.5 Silicon Monoxide

Another linear rotor is silicon monoxide (SiO). Similarly to CS, it is detected by telescopes observing near 7 mm wavelengths. However, SiO is a rarer molecule than CS and is not generally found in the relatively inert cores of molecular clouds. Instead, SiO can be formed in clouds which have been disturbed by the presence of shocks. Thus, this molecule can be used to detect the influence of SNRs and hence possible regions of intense star formation. Observations of SiO were made by both of the surveys described in the section on CS. No analysis of the physical properties of the gas was completed using SiO spectral lines, thus discussion of such a calculation is beyond the scope of this study.

3.8.6 Ammonia

Ammonia is a symmetric top molecule where the main emission lines are observed in telescopes operating at 12 mm wavelengths. The 12 mm sky in the region of HESS J1616-508 and the northern section of HESS J1614-518 has been previously studied and little ammonia was found coincident with the sources. The southern section of HESS J1614-518 was observed in this study using the Mopra radio telescope. The first transition of ammonia is distinct due to the 4 satellite lines surrounding the main emission line.

Ammonia has a pyramid structure which has the nitrogen atom at a peak and the three hydrogen atoms forming the base. Classically, the nitrogen nucleus is prevented from crossing the base to form an inverted molecule. However, the quantum properties of the particles introduces a finite probability of such an event occurring, thus vibrational behaviour occurs. This can be affected by the rotation of the molecule. If the molecule is rotating about the principal axis the base of the pyramid spreads out, lowering the potential that the nitrogen atom encounters when crossing the base. However, if rotation is perpendicular to the axis, then the base of the pyramid becomes smaller, thus increasing the potential. These behaviours either increase or decrease the frequency of inversions respectively.

The nitrogen nucleus has splitting of the main spectral line due to the charge distribution not being spherical. This means that the particle has a quadrupole moment which interacts with the electrons in the molecule and hence splitting occurs. This produces a distinctive spectrum with two satellite peaks on either side of the main peak. If the gas is optically thin, then the ratio of the intensities of the peaks can be calculated from theory. The benefit of the five peak spectrum is that combinations of the peaks can be used to calculate the optical depth instead of requiring a higher transition to be detected. The frequencies of the peaks are shown in the next table.

While the study of ammonia gas provides important information about the molecular gas, in particular the temperature and optical depth in gas that is cold enough such that CS molecules have frozen out onto dust grains, this study focuses on just the detection of

Number	Relative Line Frequency (kHz)
1	1539
2	593
3	-5
4	-605
5	-1547

Table 3.1: The frequencies of the 5 NH_3 (1–1) spectral lines shown relative to the frequency $\nu_o = 23694495.5$ kHz (Rydbeck et al., 1977).

ammonia. A detailed discussion of the specifics of the mass and temperature calculations are not provided.

3.8.7 Recombination Lines

Recombination lines are the result of an excited electron transitioning back through the energy levels to the lowest possible state. They can be observed towards regions containing partially ionised gas. The ions capture electrons in their outer shells. The main source of recombination lines come from hydrogen and helium although other atoms and molecules could also contribute. The terminology for radio recombination lines refers to the lower shell number and the number of energy levels the electron jumped (Δn). For $\Delta n = 1,\ 2,\ 3, \ldots$, the symbols used to indicate this are $\alpha,\ \beta,\ \gamma, \ldots$. Thus the emission from an electron transitioning from $n = 70$ to $n = 69$ would be known as $H_{69\alpha}$ emission.

Similarly to HII, radio recombination lines are useful in identifying gas features which contain ionised gas. In particular, they are used in studying nebulae. However, they can also identify areas of strong stellar winds such as those in OB associations and around WR stars. Observations of recombination lines have been made using the 12 mm receiver on the Mopra radio telescope. The observations were conducted towards the southern half of HESS J1614-518.

	g_b Extent	g_l Extend	FWHM	$\Delta\nu$	T_{RMS}
M 3mm Map	Full	Full	$30''$	87.6 m/s	1.4 K
M 7mm Map	$331.5^o \pm 0.35^o$	$-0.675^o \pm 0.175^o$	$72''$	10.8 km/s	0.02 K
M 12mm Map	$331.5^o \pm 0.5^o$	$-0.75^o \pm 0.25^o$	$135''$	10.7 km/s	0.06 K
M 7mm Point	–	–	$72''$	206 m/s	0.02 K
M 12mm Point	–	–	$135''$	426 m/s	0.05 K
N 3mm Map	Full	Full	$2.6'$	1 m/s	0.4 K
ATCA 21cm	Full	Full	$130''$	193 km/s	1.6 K
ATCA 7mm	Full	$0^o \pm 0.5^o$	$57''$	191 km/s	0.036 K
MOST 834 GHz	Full	Full	$55''$	-	0.06 K
Spitzer 8 micron	Full	Full	$0.3''$	-	100 MJy/sr
HESS	Full	Full	$10'$	-	-

Table 3.2: The parameters of the observations used. M stands for Mopra and N stands from Nanten. Data sets where the galactic longitude and latitude were labelled 'Full' indicate that both HESS J1616-508 and HESS J1614-518 were covered by the data. This does not apply to deep pointings since they are a pencil beam. $\Delta\nu$ is the channel spacing in the data cubes where applicable and T_{RMS} was calculated using the `MIRIAD` task `imstat`.

3.9 Telescopes Employed in this Thesis

The observations used in this thesis were taken from the Mopra radio telescope, the Nanten telescope, the Australian Telescope Compact Array (ATCA), the Mononglo Observatory Synthesis Telescope (MOST), the Spitzer Space Telescope, the Fermi Space Telescope and HESS. The properties of each telescope and the observation modes used are shown in Table 3.2. The observations are described in more detail in the following sections.

Some data sets required additional processing before they could be used. The SGPS data had to be converted from Jansky per beam to Kelvin and corrected for oversampling. The Mopra CO data had to be corrected for the beam efficiency. This is explained in more detail later in this chapter.

The radio data from Mopra, Nanten and ATCA were in the form of a data cube. Data cubes have the sky plane coordinates along two axes while the other can be presented in units of frequency or the Doppler shifted velocity which can be obtained using the galactic rotation curve (Brand and Blitz, 1993). Thus both the morphological and spectral characteristics of gas can be investigated.

3.9.1 Mopra Radio Telescope

The Mopra radio telescope, located in the Warrumbungle Mountains near Coonabarabran, NSW has been used to observe spectral lines with wavelengths of approximately 3 mm, 7 mm and 12 mm.

The main CO data used in this study was taken from the Mopra CO survey using the 3 mm receiver. The southern section of HESS J1614-518 was also mapped by the telescope's 7 mm and 12 mm receiver. The telescope is capable of observing multiple spectral lines in a single observation using an instrument called MOPS. The observed spectral lines for 3 mm, 7 mm and 12 mm are shown in the next three tables. There are two methods

Spectral Line	Frequency (Hz)
^{12}CO	110.201353
^{13}CO	109.782173
C^{17}O	112.358985
C^{18}O	115.271202

Table 3.3: The main molecular lines used in 3mm radio data analysis and their corresponding rest frequency.

Spectral Line	Frequency (Hz)	Spectral Line	Frequency (Hz)
SiO 1–0 v1	43122.079	HC_5N 17–16	45264.750
SiO 1–0 v2	43820.582	HC_3N 5–4 F5-5	45488.839
^{29}SiO 1–0	42879.922	^{13}CS 1–0	46247.580
SiO 1–0 v3	42519.373	HC_5N 16–15	47927.275
^{30}SiO 1–0	42373.365	C^{34}S 1–0	48206.946
CH_3OH–I	44069.476	OCS 4–3	48651.604
SiO 1–0	43423.864	CS 1–0	48990.957
HC_7N 40–39	45119.064		

Table 3.4: The main molecular lines used in 7mm radio data analysis and their corresponding rest frequency.

by which observations can be taken. The telescope can be used to take deep position switched observations towards just one section of the sky where the telescope alternates between observing the source and a region of sky empty of emission. These are known as deep pointings. They do not reveal the morphology of the gas due to the limited spatial coverage. However, they have a high sensitivity which makes such observations useful for

Spectral Line	Frequency (Hz)	Spectral Line	Frequency (Hz)
NH_3 8–6	20719.221	NH_3 2–2	23722.6336
NH_3 9–7	20735.452	NH_3 3–3	23870.1269
NH_3 7–5	20804.830	CH_3OH I 1	24928.7150
C_6H	20792.872	CH_3OH I 2	24933.4680
NH_3 11–9	21070.739	CH_3OH I 3	24942.3820
NH_3 4–1	21134.311	CH_3OH I 4	24595.0790
CH_3OH II	19967.396	CH_3OH I 5	25018.1230
$H_{69\alpha}$	19591.110	CH_3OH I 6	25124.8720
$H_{65\alpha}$	23404.280	NH_3 6–6	25056.0250
CH_3OH	23444.778	HC_5N 10–9	26626.533
CH_3OH II	23121.024	$H_{62\alpha}$	26939.170
NH_3 2–1	23089.819	CH_3OH I 7	26847.205
C_2S	22344.030	HC_3N 3–2	27294.078
H_2O	22235.253	NH_3 9–9	27477.943
NH_3 1–1	23694.4709	CH_3OH I 8	27472.501

Table 3.5: The main molecular lines used in 12mm radio data analysis and their corresponding rest frequency.

confirming if regions contain some emission.

Another form of observation is on-the-fly mapping which is where the telescope performs less sensitive observations over a wide spatial area. This type of observation allows the morphology of the gas to be analysed which has been done for the bulk of this study's gas analysis. Such observations can be found to not provide any information if the emission is lower than the sensitivity of the telescope in this mode. In this case, the observation can only be used to place an upper limit on the possible detectable emission.

Mopra CO Survey

The Mopra CO survey is still in progress with 10 square degrees of sky along the galactic plane recently released to the public (Braiding et al., 2015). It uses the MOPS instrument on the telescope to observe multiple wavelengths in a single observation. The survey provides information about CO gas as well as three other isotopologues, ^{13}CO, $C^{18}O$ and $C^{17}O$ although the last isotope is not observed outside of the densest regions in the galactic center. The survey aims to cover the fourth quadrant of the galactic plane and extends 0.5 degrees above and below the plane.

The data is presented in cubes 1° square in size and is observed using the on-the-fly method. The cubes are observed in 10 longitudinal and 10 latitudinal strips which are then combined, thus providing a sensitivity of 1.4 K within approximately 20 hours of observation time. This provided total coverage for HESS J1616-508. In order to cover HESS J1614-518, the survey was extended down to $g_b = -1^o$ for 330° to 333°. The additional half-cubes were only observed in longitudinal strips. Hence the noise level is higher in comparison to the main cubes.

The data provided by the Mopra CO survey was already corrected for oversampling and in units of Kelvin. Additional corrections had to be made when calculating the column density to convert the intensity recorded by the telescope into the intensity that the telescope would have observed if the detector had a 100% efficiency. This beam efficiency of the telescope is a measure of the percentage of light received by the telescope that was subsequently detected. If the region of interest is smaller than the beam of the telescope it must be assumed that the emission fills the beam. Then the efficiency is $\eta_{MB} = 0.42$. For regions of emission that are larger than the beam of the telescope, the beam efficiency is $\eta_{XB} = 0.55$ (Urquhart et al., 2010). The corrected intensity is then given by

$$T_A = \frac{T_A^*}{\eta} \tag{3.67}$$

where T_A^* is the measured intensity and η is the appropriate beam efficiency for the situation.

Mopra 7 mm and 12 mm Maps

The MALT-45 7 mm survey and the HOPS 12 mm survey both did not cover the HESS TeV source HESS J1614-518 due to its displacement form the galactic plane. To complete the data set, this study mapped the southern part of HESS J1614-518 in both 7 mm and 12 mm. The spatial extent of these maps are presented in Table 3.2. The 7 mm mapping included observations of the CS (1–0) transition. Thus, the Mopra 7 mm maps could be combined with the MALT-45 survey.

3.9.2 Mopra 7 mm and 12 mm Deep Pointings

In addition to mapping the regions left uncovered by previous surveys, some deep pointings were directed towards the stellar cluster Pismis 22 to search for tracers of dense molecular gas. In total, 5 position switched pointings were made towards and surrounding the cluster, each an hour of duration with 30 minutes on source and 30 minutes towards the reference. The T_{RMS} of the pointings are listed in table 3.2. The deep pointings made directly towards the cluster were taken at both 7 mm and 12 mm wavelengths. These pointings were given the position label P. Four other pointings were taken using the 12 mm receiver and are labelled PU, PD, PL and PR for the positions above, below, left and right of the cluster respectively. The locations are shown in Figure 3.1 while table 3.6 presents the locations in galactic coordinates.

Wavelength	g_l	g_b
7 mm	331.468	-0.597
12mm	331.468	-0.597
12mm	331.468	-0.497
12mm	331.468	-0.697
12mm	331.368	-0.597
12mm	331.568	-0.597

Table 3.6: The locations of the deep pointings towards Pismis 22.

The sensitivity of the deep pointings is higher than that of the mapping described in the previous section. Initially, there was only one deep pointing towards the cluster planned in each wavelength. However, after analysing the data, there was a possible detection of the NH_3 $(1,1)$ transition in the 12 mm observations. To verify this and to possibly determine the extend of the ammonia emission, a further four pointings were taken. The RMS of the pointing was again calculated using the `MIRIAD` task `imstat`.

3.9.3 Nanten Telescope

The Nanten telescope was located at the Las Campanas Observatory in Chile at the time that the CO observations used in this study were made. The survey completed by the

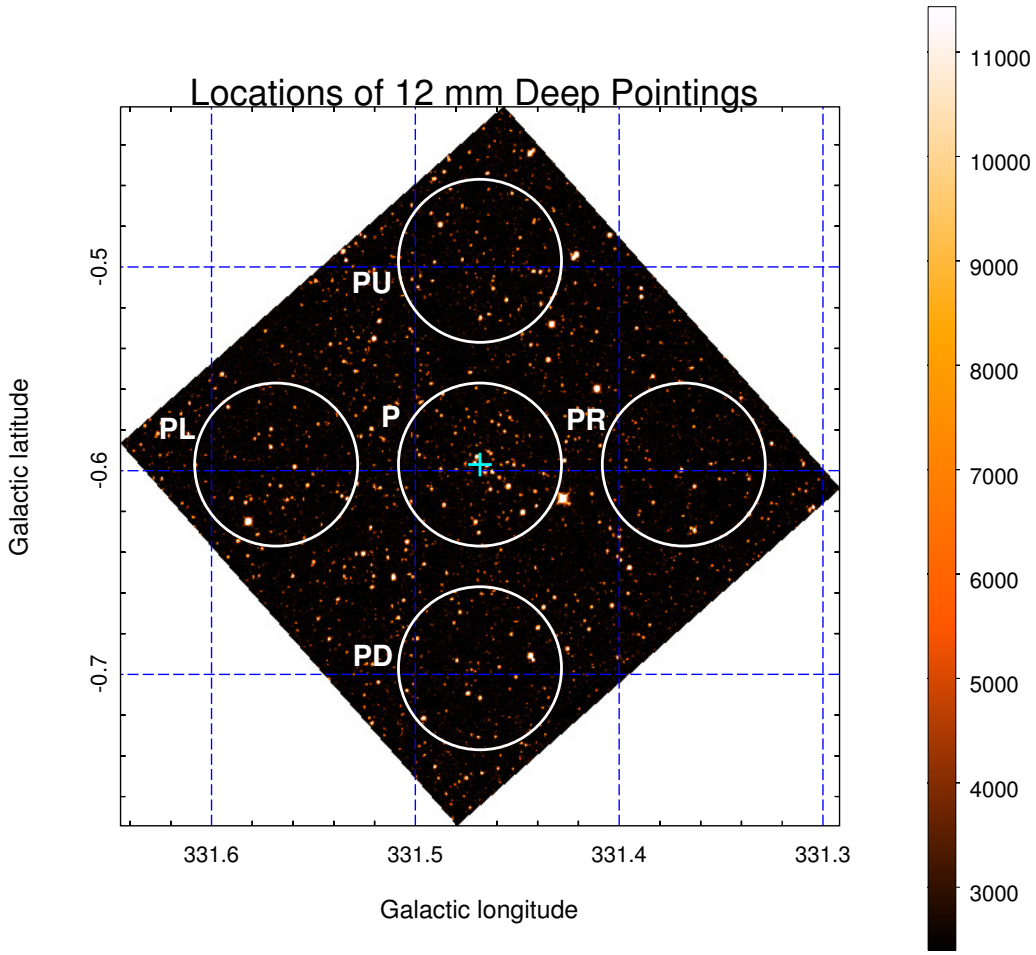

Figure 3.1: The locations of the deep pointings are shown as white circles overlaid on the optical Digital Sky Survey (DSS) map. The cyan cross marks the location of the open cluster Pismis 22.

Nanten telescope has been done at a lower resolution and sensitivity than the Mopra survey and hence is mainly useful for examining large scale structures. The telescope was later upgraded and moved to Chile where it operated at lower altitudes before it was later moved to the Atacama Plateau where it was renamed Nanten2. The data from the telescope was from the Nanten CO survey and was used to quickly identify large CO features and to verify calculations made using the Mopra CO survey. The survey was completed with a velocity channel spacing of 1 m/s and a beam size of 2.6′. The survey is sensitive to emission with a temperature of above approximately 0.4 K. The data set was surveyed at one pointing per beam which resulted in a sampling less than Nyquist. Thus, the oversampling factor is 1 and the data did not have to be corrected.

3.9.4 Australia Telescope Compact Array (ATCA) and the Parkes Telescope

ATCA is a radio interferometer located in Narribri, NSW. It consists of six 22 m dishes with a similar configuration to the Mopra telescope. Indeed, the Mopra telescope is often used in combination with ATCA to perform long baseline interferometry.

Southern Galactic Plan Survey

The Southern Galactic Plane Survey (SGPS) has mapped the HI emission in the galactic plane spanning the region of $|b| \leq 1.5^o$ and $253^o \leq l \leq 358^o$ using the Australian Telescope Compact Array (ATCA) and the Parkes telescope (McClure-Griffiths et al., 2005)[1]. The data is available as only the Parkes contribution, the combined data with continuum emission and the combined data cubes with the continuum subtracted.

The data used in this survey has primarily been the combined cubes with the continuum emission subtracted. This data had a final FWHM of $130''$, a pixel size of $40''$ and a velocity channel separation of $\Delta v = 0.82$ km/s. The RMS level for the data level is 1.6 K. The cubes, which were downloaded from the survey page managed by the CSIRO had units of Jy/beam. Thus, the following conversion factor had to be applied to the data to convert it to Kelvin:

$$\frac{\lambda^2}{2k\Omega}\,\frac{\mathrm{K}}{\mathrm{Jy/beam}} \tag{3.68}$$

where λ is the wavelength of the emission, k is the Boltzmann constant and Ω is the beam of the telescope.

When analysing the HI gas from the SGPS survey, care must be taken when dealing with artefacts. These result from two primary radio continuum sources. Firstly, the calibration of the gain of the Parkes multibeam which is due to variations between the gains of different beams. Secondly, artefacts arise from the coverage of the u-v plane, which is the

[1] Avaliable from: http://www.atnf.csiro.au/research/HI/sgps/queryForm.html

inverse Fourier transform of the sky plane, observed by ATCA since it would be unreasonable to completely fill in the plane due to time constraints. The artefact from the gain calibration can lead to some striping which is minimised along the galactic plane. The *u-v* coverage has a large impact on the data which results in continuum sources appearing as absorption features in the continuum subtracted data. Additionally, this results in radial and azimuthal features interfering with the data around the continuum features.

MALT-45 Survey

The MALT-45 survey was completed at 7mm wavelengths using only ATCA (Jordan et al., 2015). Whilst the system is technically an interferometer, the survey utilised all five of the telescopes individually, operating them each as single dish radio telescopes, to map the region at a high spatial resolution and sensitivity. The beam FWHM for the telescope used in this mode is the same as the beam of the Mopra telescope. The sensitivity of the survey was high since each survey point was essentially a deep pointing. The final area spans 5° of galactic longitude centred on 332° and $\pm 0.5^o$ above and below the galactic plane. Thus the survey provides complete coverage for HESS J1616-508 whilst it covers the northern half of HESS J1614-518.

3.10 Summary

This chapter details a broad overview of the relevant analysis techniques used in radio astronomy, focusing on the specific techniques employed for each gas that was observed. The production of gamma-rays through CR interactions relies on the presence of dense gas, thus the knowledge of the density of the gas in the regions towards HESS J1616-508 and HESS J1614-518 is crucial for modelling these interactions. The calculation of the gas density has been described using the assumption that the system is in a local thermodynamic equilibrium. The gases which can be used to make these calculations

include HI which was observed in the SGPS survey, CO isotopologues observed in the Mopra and Nanten CO Surveys and CS isotopologues observed in the MALT-45 survey and in additional Mopra mapping. The gas tracers NH_3 and SiO were also discussed briefly, although they were not the focus of this study.

Chapter 4

Interstellar Gas towards HESS J1616-508 and HESS J1614-518

The two TeV gamma-ray sources have been covered by many different galactic plane surveys including the Southern Galactic Plane Survey, The Mopra CO Survey, the Nanten CO Survey, the MOST 843 MHz survey, the Spitzer Space Telescope and the 7mm wavelength survey MALT-45, to name a few. The source HESS J1614-518 was not completely covered by MALT-45 or by another 12mm survey, HOPS. Thus additional observations were made using the Mopra radio telescope to provide full coverage. The MALT-45 survey was observed at a higher sensitivity than the observations taken in this study. This chapter aims to characterise the interstellar gas in the region of the HESS sources. Potential high energy sources are first discussed, followed by analysis of other clumps of gas in the region.

4.1 Observations

4.1.1 HESS

The HESS telescope discovered HESS J1614-518 and HESS J1616-508 in the initial galactic plane survey, HGPS. The data used in this study is publicly available from the HESS collaboration website.

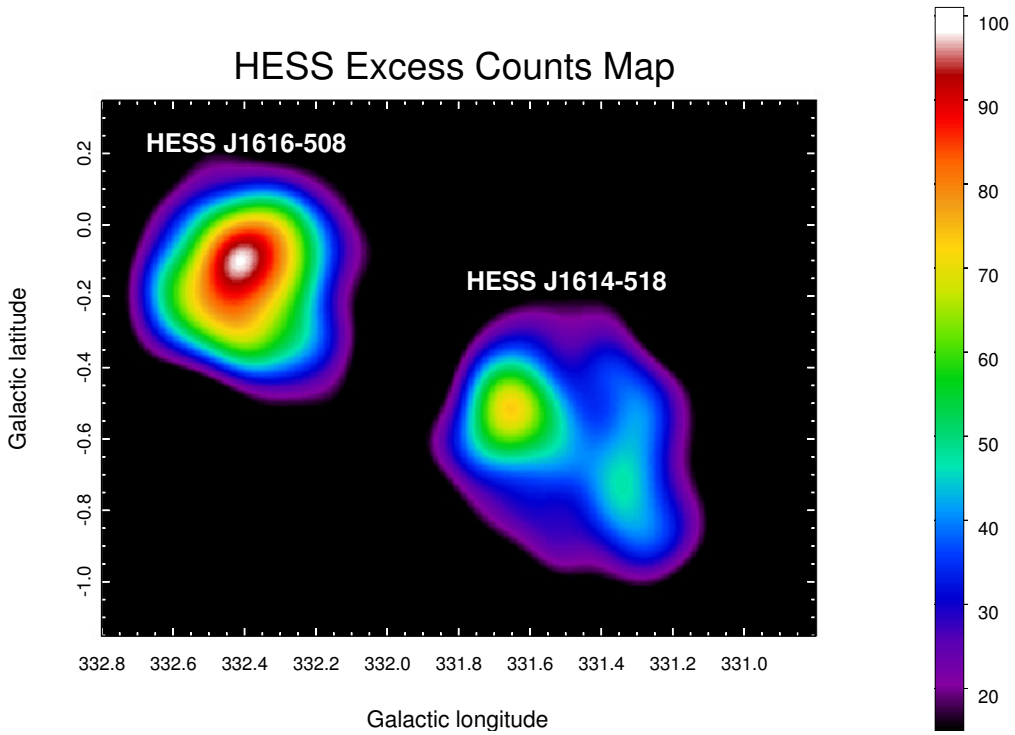

Figure 4.1: VHE gamma-ray excess counts towards HESS J616-508 and HESS J1614-518.

The observations made of HESS J1614-518 and HESS J1616-508 were done during the year of 2004. The sources were each observed for a time period of 9.8 and 10.2 hours respectively. The flux and spectral index found in the analysis presented by HESS (The HESS Collaboration, 2006) are shown in table 4.1.

Note that the flux of the Crab Nebula is approximately 3×10^{-10} cm^{-2}s^{-1} for energies greater than 200 GeV. The flux of the sources in Crab units is then 19% and 14% for HESS J1616-508 and HESS J1614-518 respectively. The HESS telescope had a sensitivity of 2% of the Crab flux for the observation time listed.

The observations of the gamma-ray sources have been used for spatial comparison with

	F < 200 TeV	Γ
HESS J1614-518	57.8 ± 7.7	2.46 ± 0.2
HESS J1616-508	43.3 ± 2.0	2.35 ± 0.06

Table 4.1: Spectral parameters of the HESS sources. (The HESS Collaboration, 2006) where the integrated flux, F less than 200 TeV is in units of erg cm^{-2} s^{-1}. The sources energy spectrum was modelled by a power law which was proportional to $E^{-\Gamma}$ where Γ is the spectral index.

the atomic and molecular gas analysed in this study using the contours of the excess counts map. HESS J1614-518 has published contours unlike HESS J1616-508. Thus, the contours for HESS J1616-508 have been made using the levels for HESS J1614-518 with additional levels due to the higher number of excess counts. The background excess count of the HESS excess counts was found to be $\sigma \approx 5$. Thus, the outer contour was set to be 6σ to ensure that the excess counts within the contour levels could be attributed towards the gamma-ray sources. The HESS excess counts map of the data towards HESS J1616-508 and HESS J1614-518 with the contours are shown in Figure 4.1.

4.1.2 Identified Potential Accelerators

There are a number of potential particle accelerators which have been identified within 1 degree of the HESS TeV gamma-ray sources HESS J1614-518 and HESS J1616-508. These included SNRs, PWNe, a stellar cluster, WR stars and two Fermi-LAT sources. The locations, age, distance and radii of the SNR, WR stars and the cluster are listed in table 4.2. The location, age, distance and spin-down power of the pulsars are listed in table 4.3. The spectral properties and locations of the two Fermi-LAT sources are listed in table 4.4. The locations of the described accelerators are shown in Figure 4.2.

4.1.3 Mopra CO Survey

The Mopra CO survey is used to trace the dark H_2 gas. After the data cubes were corrected for the beam efficiency, it was then possible to use the data to calculate properties of the gas clouds. This section identifies gas clouds from broad 10 km/s integrated maps and

Source	l (deg)	b (deg)	d (kpc)	Age (kyr)	Radius (deg)
Kes 32	332.407	0.120	5.5	3	0.13
RCW 103	332.428	-0.363	6.7	2	0.08
G332.0+0.2	332.046	0.210	7.4	10	0.10
Pismis 22	331.468^o	-0.597^o	1 kpc	40 Myr	-
WR 73-1	331.815	-0.339	10.9	<500	-
WR 74	331.877	-0.635	2.55	<500	-

Table 4.2: The location, distance, age and radius of the three SNRs, two Wolf-Rayet (WR) stars and Pismis 22. The locations and diameters of the SNRs were taken from Green et al. (1999), the distances were from Pavlovic et al. (2014) and the ages were from Vink (2004) for Kes 32, Kaspi et al. (1998) for RCW 103 and a suggested maximum age from Pavlovic et al. (2014) was used for G332.0+0.2. Pismis 22 information was taken from Piatti et al. (2000). The WR stars locations and distances were taken from van der Hucht (2001).

Source	l (deg)	b (deg)	d (kpc)	Age (kyr)	$\dot{E}$ (erg s^{-1})
PSR J1617-5055	332.5	-0.28	6.5	8.1	1.6×10^{37}
PSR J1614-5048	332.32	0.170	7.2	7.4	1.6×10^{36}
PSR J1613-5211	331.2	-0.778	6.1	377	7.9×10^{33}

Table 4.3: The location, distance, age and spin-down power of the puslars (Manchester et al., 2005).

Source	l (deg)	b (deg)	F	Γ
3FGL J1615.3-5146e	331.659	-0.659	$9.3 \pm 0.6 \times 10^{-9}$	1.86 ± 0.04
3FGL J1616.2-5054e	332.365	-0.131	$13.9 \pm 0.7 \times 10^{-9}$	2.14 ± 0.03

Table 4.4: The spectral properties of the Fermi-LAT GeV gamma-ray sources and their locations. (Acero et al., 2015) The integrated flux, F, from 1 GeV to 100 GeV is in units of photons cm^{-2} s^{-1}. The spectral index of the power law that the GeV flux was fitted to is given by Γ

explains the process of calculating the column density, mass and density of the cloud from its spectral line.

Integrated maps of ^{12}CO are shown in Figure 4.3 and 4.4 with the contours of the HESS TeV gamma-ray contours. The data was integrated over 10 km/s intervals. The galactic plane in the ^{12}CO data can be seen as a dense, horizontal band of gas between -80 km/s to -100 km/s. Upon examination of the data it is evident that there is not much overlap of the gas and HESS J1614-518 on the scales presented. CO regions of interest (RoI) were selected from these interval ranges and are represented as black ellipses. Similar figures

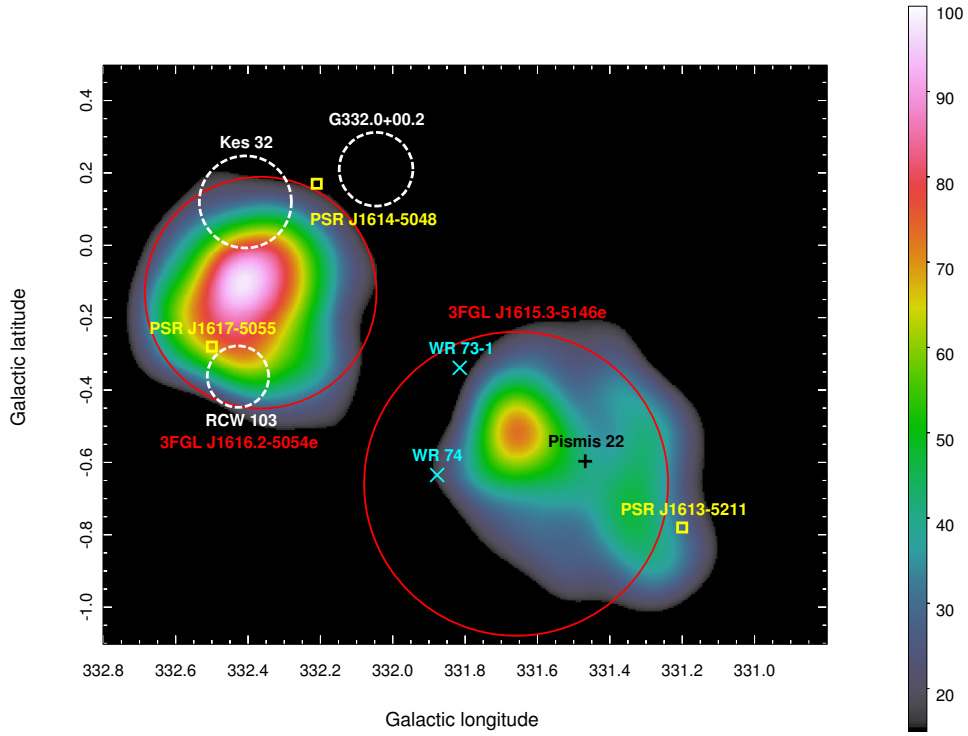

Figure 4.2: The HESS excess counts above background map with the locations of the potential accelerators marked. The SNRs are shown as white dashed circles, the pulsars are yellow squares, the WR stars are cyan crosses, the cluster Pismis 22 is marked by a black plus and the Fermi-LAT sources are red circles.

for ^{13}CO and C^{18}O are located in appendix B.

Once the data was corrected, it was then possible to calculate the column density using the conversion factor X_{CO}. This can be done on a pixel by pixel basis or over a wide region. The former case require the data to be corrected by η_{MB} while the latter needs the data to be corrected by η_{XB}. When dealing with RoI, the observed brightness temperature was integrated over the cloud's velocity range before the correction was applied and then the column density of molecular hydrogen was calculated using Equation 3.58.

Regions of interest, presented in Figures 4.3 and 4.4, were chosen for their proximity to potential high energy accelerators or with the HESS TeV gamma-ray contours. Their locations are shown in tables 4.5 and 4.6. After they had been located, the ISM spectra of the regions were taken from the main data cube. The spectral components were then fitted using a sum of Gaussian functions using the `MINUIT` module in `root` which is software developed by CERN which was found to be more efficient than the `Python SciPy` curve

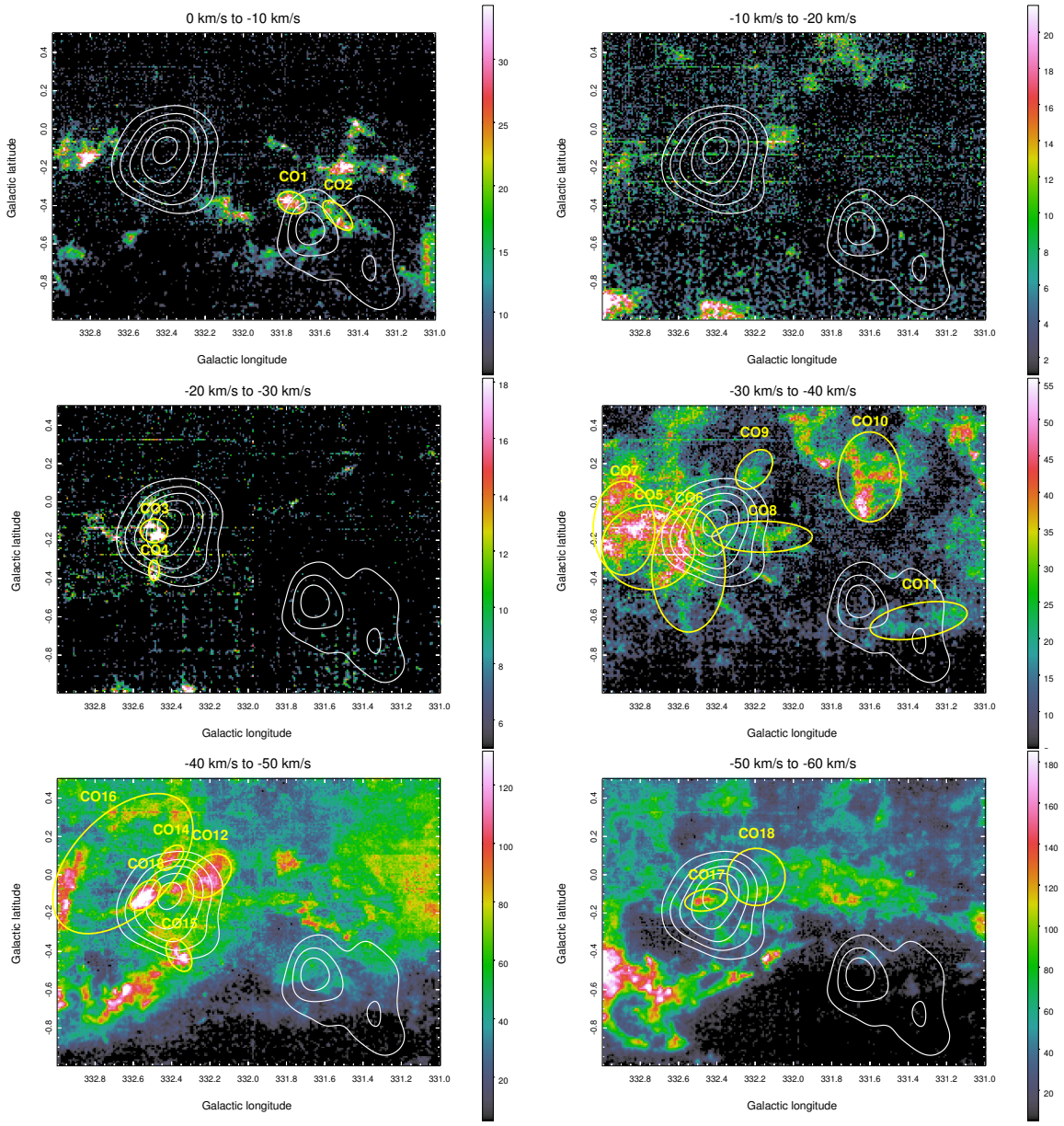

Figure 4.3: Integrated maps of ^{12}CO from 0km/s to -60km/s in 10km/s intervals. The excess HESS TeV gamma-ray contours are shown in white. RoI are marked as yellow ellipses. The coordinates are in units of degrees and the colour scale is in Kelvin.

fitting toolbox. An example of the fit generated for RoI CO1 is shown in Figure 4.5. The spectral line of CO1 was found to be fitted with a Gaussian function described by

$$p_0 \exp\left[\frac{(v-p_1)^2}{2p_2^2}\right] \tag{4.1}$$

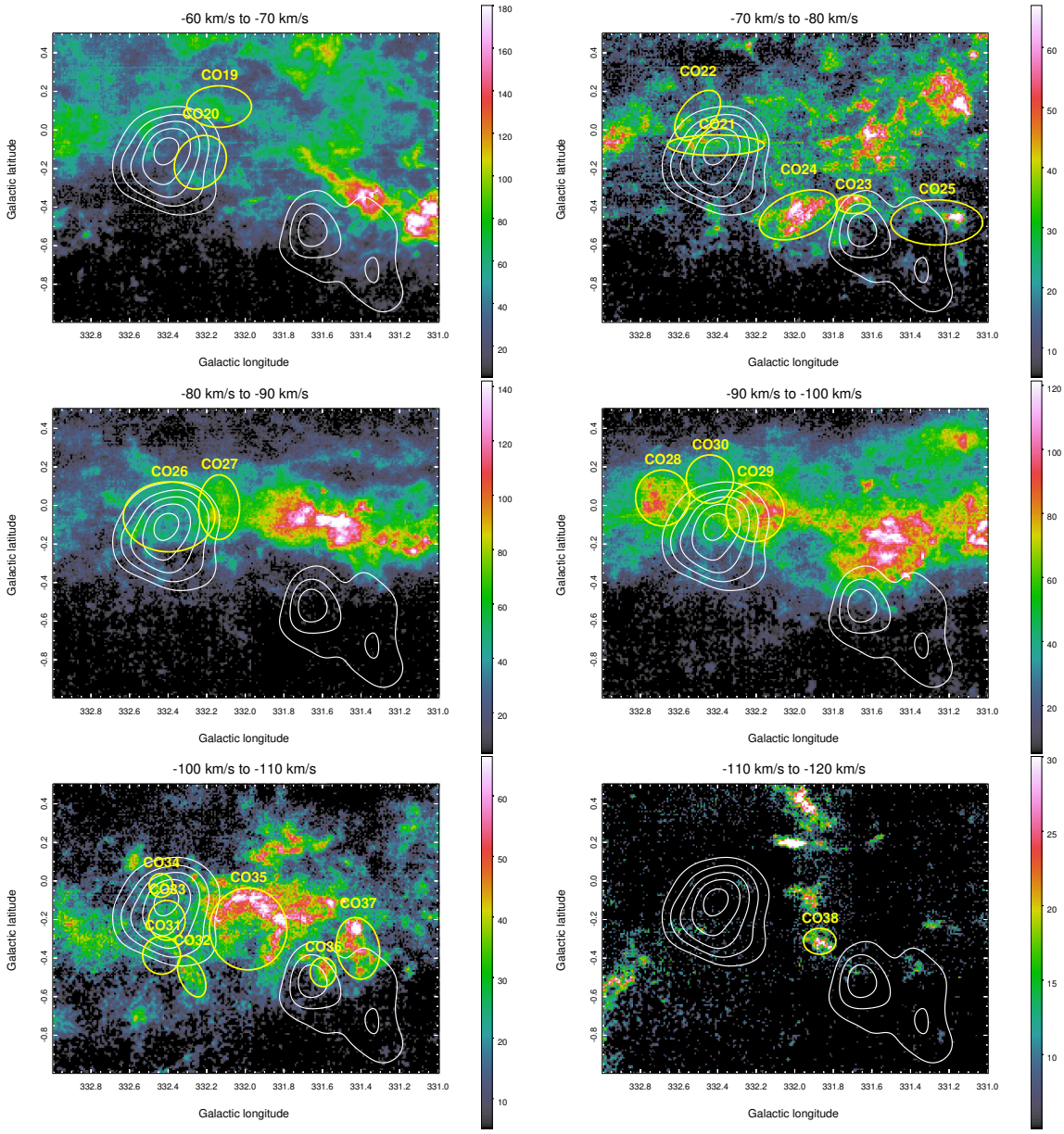

Figure 4.4: Integrated maps of ^{12}CO from -60km/s to -120km/s in 10km/s intervals. The excess HESS TeV gamma-ray contours are shown in white. RoI are marked as yellow ellipses. The coordinates are in units of degrees and the colour scale is in Kelvin.

where p_0 is the height of the Gaussian, p_1 is the mean and p_2 is one standard deviation. The RoI, CO1, had the parameters $p_0 = 354$ k, $p_1 = -5$ km/s and $p_2 = 2$km/s. The data cube was then integrated over the velocity range defined by the full width half maximum (FWHM) of the Gaussian function fitted to the spectral component. The size and location of the region was then modified if necessary to ensure that a majority of the gas in the clump was included. The fitting process was then repeated.

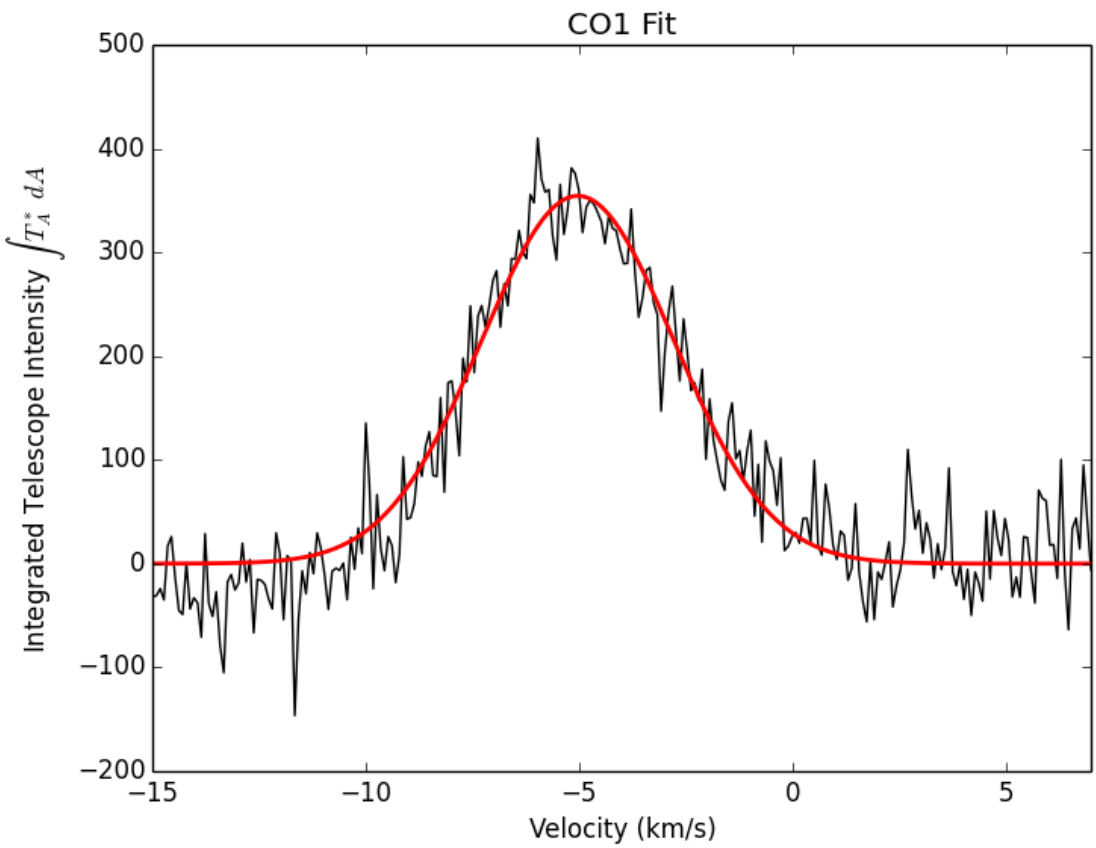

Figure 4.5: An example of the Gaussian function found for ^{12}CO using `root` to the peaks of the RoI CO1.

The intensity of the emission within the regions was then calculated by numerically integrating over the Gaussian which was the best fit for the peak of interest. This was converted into a column density, mass and density using the Equation 3.58, 3.59 and 3.56.

The errors on the integrated emission are due to statistical fluctuations in the data and the offset of the continuum level from zero. For each region, this was calculated by fitting a DC offset to each dataset averaged over the number of pixels. The fitting routine was implemented using the curve fitting tool in Python's SciPy module. The tool uses the Levenberg-Marquardt algorithm (LMA) which is a method of solving non-linear least squares problems. Thus, the level of the continuum and the error in determining it were found. The error on the flux measured by the telescope is then given by the sum of the statistical error and the error of determining the continuum level. The errors from calcu-

RoI	l	b	a	b	θ	v	1σ v	$T^*_{A_{max}}$	d_n	d_f
CO1	331.746	-0.384	0.43	0.31	158	-5.0	2.3	354.4	0.3	14.7
CO2	331.507	-0.451	0.77	0.35	135	-6.4	2.1	379.7	0.4	14.5
CO3	332.492	-0.151	2.73	2.36	0	-29.4	3.3	57.2	2.2	12.9
CO4	332.492	-0.358	1.07	2.09	0	-30.0	2.5	196.5	2.2	12.8
CO5	332.758	-0.238	12.13	11.01	0	-39.9	3.9	7137.6	2.9	12.3
CO6	332.548	-0.357	9.97	16.71	0	-41.9	2.3	9563.1	3.0	12.1
CO7	332.885	-0.137	8.02	12.23	0	-39.8	3.6	5158.8	2.9	12.3
CO8	332.164	-0.182	12.27	3.79	0	-37.2	3.1	878.4	2.7	12.4
CO9	332.205	0.170	4.03	6.05	140	-41.9	2.4	3479.4	3.0	12.1
CO10	331.603	0.131	7.00	9.97	0	-33.6	2.1	3031.2	2.4	12.5
CO11	331.346	-0.620	13.61	4.81	10	-43.8	4.1	7076.7	3.0	11.9
CO12	332.203	-0.006	6.94	4.87	45	-42.7	3.0	3667.4	3.0	12.0
CO13	332.537	-0.106	5.62	3.32	45	-48.3	1.7	1688.5	3.3	11.8
CO14	332.403	0.089	4.63	2.60	45	-47.4	1.2	826.7	3.3	11.8
CO15	332.362	-0.419	5.40	3.30	120	-48.5	1.8	1148.5	3.3	11.7
CO16	332.655	0.058	25.77	14.87	45	-47.6	-1.3	6143.3	3.3	11.8
CO17	332.457	-0.132	6.60	3.30	10	-49.4	2.0	2850.8	3.4	11.7
CO18	332.194	-0.012	8.96	8.85	10	-49.8	1.6	3120.5	3.4	11.6
CO19	332.136	0.121	12.57	8.07	0	-67.1	3.5	2093.2	4.3	10.7

Table 4.5: The locations of the CO RoI from CO1 to CO19 are in columns 2 and 3 in galactic longitude and latitude with units of degrees. The semi-major, semi-minor and angle from the galactic plane are listed in columns 4, 5 and 6 respectively with units of degrees. The peak velocity and the 1σ width of the Gaussian fit are listed in columns 7 and 8 in units of km/s. The peak intensity measured by the telescope is then presented in column 9 in units of Kelvin. The near and far distances in units of kpc are listed in the last two columns.

lating other parameters such as the optical depth, column density, mass and density can then be propagated through.

The locations and parameters of the CO (1–0) RoI ellipses are presented in table 4.5 and 4.6 along with the fitting parameters and the near and far distances.

4.1.4 Nanten CO Survey

The CO emission observed by the Nanten telescope is presented here for comparison with the Mopra CO Survey. The integrated maps of Nanten CO emission are shown in Figures 4.6 and 4.7 with the HESS TeV gamma-ray contours.

The Nanten data set was not Nyquist sampled. Instead, the survey was completed such

RoI	l	b	a	b	θ	v	1σ v	$T^*_{A_{max}}$	d_n	d_f
CO20	332.233	-0.167	9.49	11.29	320	-68.5	2.8	2214.4	4.4	10.7
CO21	332.409	-0.079	19.28	4.07	0	-69.2	2.8	2081.7	4.4	10.7
CO22	332.503	0.076	6.58	11.49	320	-67.5	4.1	1871.4	4.3	10.8
CO23	331.698	-0.386	7.10	3.77	0	-72.5	1.3	572.5	4.6	10.4
CO24	331.981	-0.440	16.57	9.01	20	-71.3	4.8	2394.7	4.5	10.5
CO25	331.264	-0.479	17.70	8.72	0	-66.8	3.0	7219.5	4.3	10.6
CO26	332.395	-0.059	21.67	16.57	0	-86.2	4.4	4263.1	5.2	9.8
CO27	332.136	-0.009	9.45	14.92	0	-83.6	4.4	1971.5	5.1	9.9
CO28	332.685	0.039	14.07	14.64	0	-96.9	1.3	1069.2	5.8	9.3
CO29	332.205	-0.034	14.99	15.27	0	-95.1	4.9	3320.9	5.7	9.3
CO30	332.440	0.136	12.27	12.55	0	-95.7	-1.7	350.3	5.7	9.3
CO31	332.434	-0.385	10.37	10.37	0	-101.9	4.2	497.7	6.1	9.0
CO32	332.278	-0.494	6.66	12.41	25	-103.7	2.7	712.1	6.2	8.8
CO33	332.406	-0.204	10.06	10.95	0	-101.8	4.4	613.0	6.1	9.0
CO34	332.437	-0.023	6.54	6.55	0	-102.3	1.9	354.1	6.1	9.0
CO35	331.985	-0.249	21.21	22.38	0	-100.8	6.3	4077.0	6.0	9.0
CO36	331.597	-0.472	7.01	7.88	0	-99.4	3.8	736.6	6.0	9.0
CO37	331.416	-0.349	12.17	17.76	10	-103.8	3.6	1339.7	6.3	8.6
CO38	331.871	-0.313	10.33	8.26	0	-111.9	2.0	227.4	7.1	7.9

Table 4.6: The locations of the CO RoI from CO20 to CO38 are in columns 2 and 3 in galactic longitude and latitude with units of degrees. The semi-major, semi-minor and angle from the galactic plane are listed in columns 4, 5 and 6 respectively with units of degrees. The peak velocity and the 1σ width of the Gaussian fit are listed in columns 7 and 8 in units of km/s. The peak intensity measured by the telescope is then presented in column 9 in units of Kelvin. The near and far distances in units of kpc are listed in the last two columns.

RoI	$\bar{T_A^*}$	err $\bar{T_A^*}$	N_{H_2}	err N_{H_2}	M	err M	ρ	err ρ
CO1	19.3	3.7	2.9×10^{21}	5.5×10^{20}	23.4	0.4	7258.0	138.8
CO2	18.0	2.4	2.7×10^{21}	3.6×10^{20}	43.3	0.6	6051.5	81.5
CO3	4.3	3.7	6.5×10^{20}	5.6×10^{20}	253.0	21.8	214.6	18.5
CO4	34.0	3.2	5.1×10^{21}	4.9×10^{20}	690.9	6.6	3690.1	35.1
CO5	52.0	11.7	7.8×10^{21}	1.7×10^{21}	62868.5	141.1	550.4	1.2
CO6	36.3	7.8	5.4×10^{21}	1.2×10^{21}	54752.7	118.1	424.5	0.9
CO7	52.2	11.0	7.8×10^{21}	1.7×10^{21}	46359.4	97.9	758.9	1.6
CO8	12.8	3.6	1.9×10^{21}	5.5×10^{20}	5381.4	153.2	393.8	11.2
CO9	92.4	7.7	1.4×10^{22}	1.1×10^{21}	20420.6	16.9	2673.4	2.2
CO10	16.2	3.1	2.4×10^{21}	4.6×10^{20}	10263.5	195.1	270.0	5.1
CO11	124.3	5.0	1.9×10^{22}	7.4×10^{20}	73711.5	294.6	3014.9	12.0
CO12	91.0	11.1	1.4×10^{22}	1.7×10^{21}	27814.0	34.0	2180.9	2.7
CO13	52.6	13.5	7.9×10^{21}	2.0×10^{21}	8891.1	22.9	1845.5	4.8
CO14	27.1	6.5	4.1×10^{21}	9.8×10^{20}	2946.4	70.9	1216.5	29.3
CO15	39.8	9.1	6.0×10^{21}	1.4×10^{21}	6428.6	14.7	1403.8	3.2
CO16	7.1	4.1	1.1×10^{21}	6.1×10^{20}	24498.3	1413.9	55.3	3.2
CO17	90.0	13.9	1.4×10^{22}	2.1×10^{21}	17757.6	27.4	3183.8	4.9
CO18	22.8	8.2	3.4×10^{21}	1.2×10^{21}	16341.5	58.9	300.1	1.1
CO19	41.0	9.2	6.1×10^{21}	1.4×10^{21}	37677.5	84.9	592.5	1.3

Table 4.7: The gas parameters calculated for RoI CO1 to CO19. The average telescope beam temperature, $\bar{T_A^*}$, in Kelvin, the column density N_{H_2}, in cm^{-2}, the mass, M, in solar masses and the density, ρ, in H_2 per cm^{-3} are presented with their statistical errors.

RoI	$\bar{T_A^*}$	err $\bar{T_A^*}$	N_{H_2}	err N_{H_2}	M	err M	ρ	err ρ
CO20	33.3	7.0	5.0×10^{21}	1.1×10^{21}	32335.3	68.3	409.6	0.9
CO21	43.6	7.0	6.5×10^{21}	1.1×10^{21}	31022.6	49.9	1250.4	2.0
CO22	57.3	10.9	8.6×10^{21}	1.6×10^{21}	39259.9	74.6	1015.7	1.9
CO23	17.0	5.1	2.5×10^{21}	7.7×10^{20}	4112.3	124.2	524.9	15.9
CO24	47.4	10.1	7.1×10^{21}	1.5×10^{21}	64199.6	136.8	614.2	1.3
CO25	77.4	17.1	1.2×10^{22}	2.6×10^{21}	108291.9	238.9	1035.2	2.3
CO26	43.5	10.5	6.5×10^{21}	1.6×10^{21}	141620.0	340.9	306.5	0.7
CO27	49.3	12.7	7.4×10^{21}	1.9×10^{21}	63000.9	161.9	608.4	1.6
CO28	6.7	4.8	1.0×10^{21}	7.2×10^{20}	12549.7	894.2	55.7	4.0
CO29	70.6	16.4	1.1×10^{22}	2.5×10^{21}	146495.9	341.0	549.8	1.3
CO30	3.8	4.0	5.7×10^{20}	6.0×10^{20}	5275.7	562.4	36.0	3.8
CO31	22.0	4.9	3.3×10^{21}	7.4×10^{20}	21469.9	479.5	247.8	5.5
CO32	27.5	4.2	4.1×10^{21}	6.2×10^{20}	20586.5	311.4	481.6	7.3
CO33	28.1	6.3	4.2×10^{21}	9.4×10^{20}	28065.3	627.2	325.8	7.3
CO34	17.8	4.1	2.7×10^{21}	6.2×10^{20}	6904.2	159.2	317.0	7.3
CO35	60.3	13.7	9.0×10^{21}	2.0×10^{21}	259323.5	587.9	331.6	0.8
CO36	55.8	9.8	8.4×10^{21}	1.5×10^{21}	27925.2	49.1	929.1	1.6
CO37	27.3	6.6	4.1×10^{21}	10.0×10^{20}	53550.5	1301.6	262.1	6.4
CO38	8.2	2.5	1.2×10^{21}	3.8×10^{20}	6347.8	195.7	115.8	3.6

Table 4.8: The gas parameters calculated for RoI CO20 to CO38. The average telescope beam temperature, $\bar{T_A^*}$, in Kelvin, the column density N_{H_2}, in cm^{-2}, the mass, M, in solar masses and the density, ρ, in H_2 per cm^{-3} are presented with their statistical errors.

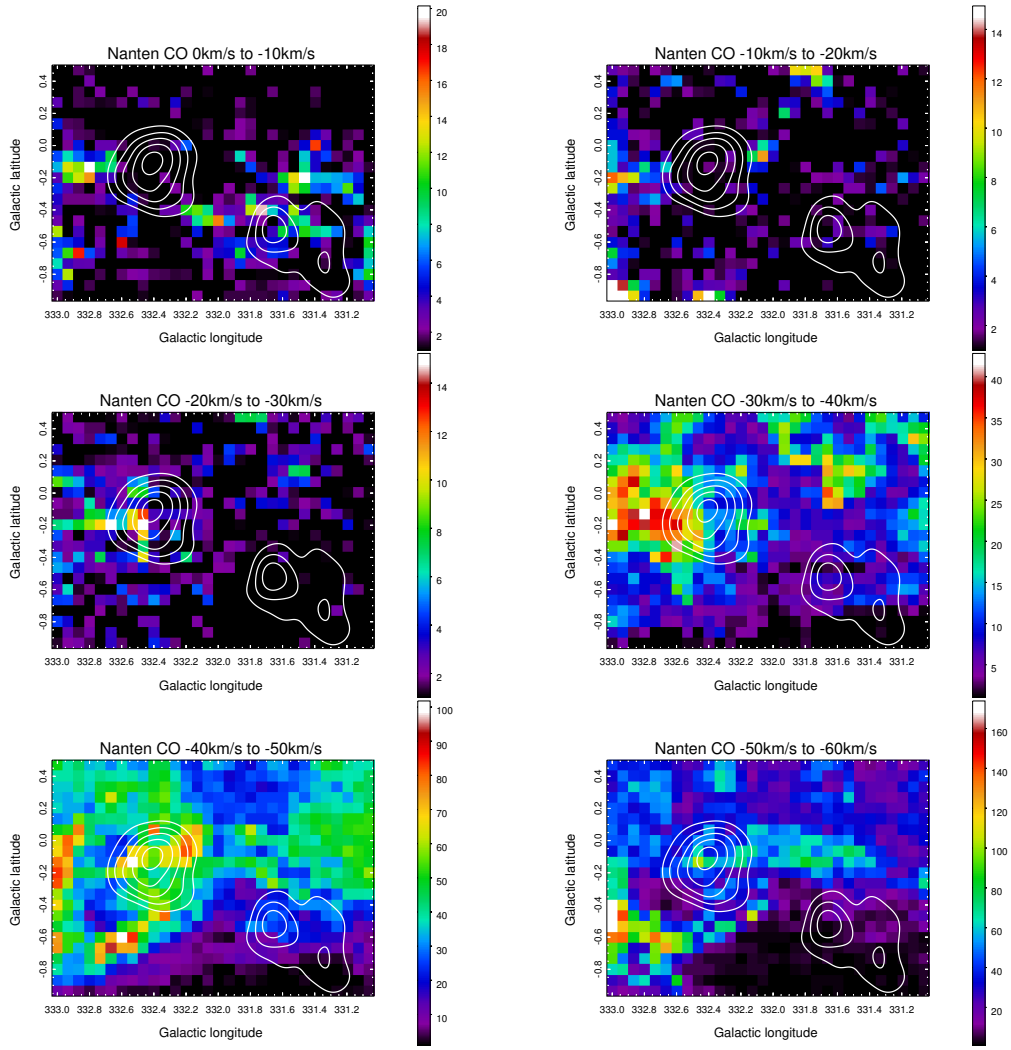

Figure 4.6: Integrated 10km/s maps from 0 km/s to -60 km/s of CO data from the Nanten telescope where the HESS TeV gamma-ray excess counts contours are shown in white. The axes are in units of degrees while the colour scale is in Kelvin.

that the oversampling factor was 1. Additionally, corrections for the beam efficiency of the telescope were already applied to the data supplied by the Nanten team. Thus, no corrections had to be performed on the data in order to compute the column density. Comparing the integrated maps of the CO (1–0) emission from the Nanten telescope and the Mopra telescope, it can be seen that the spatial resolution from Nanten does not reveal morphologically interesting features as well as the Mopra CO (1–0) Survey. Thus the main use of Nanten data has been to verify the calculations of column density, mass and density as explained in the section on the Mopra CO survey.

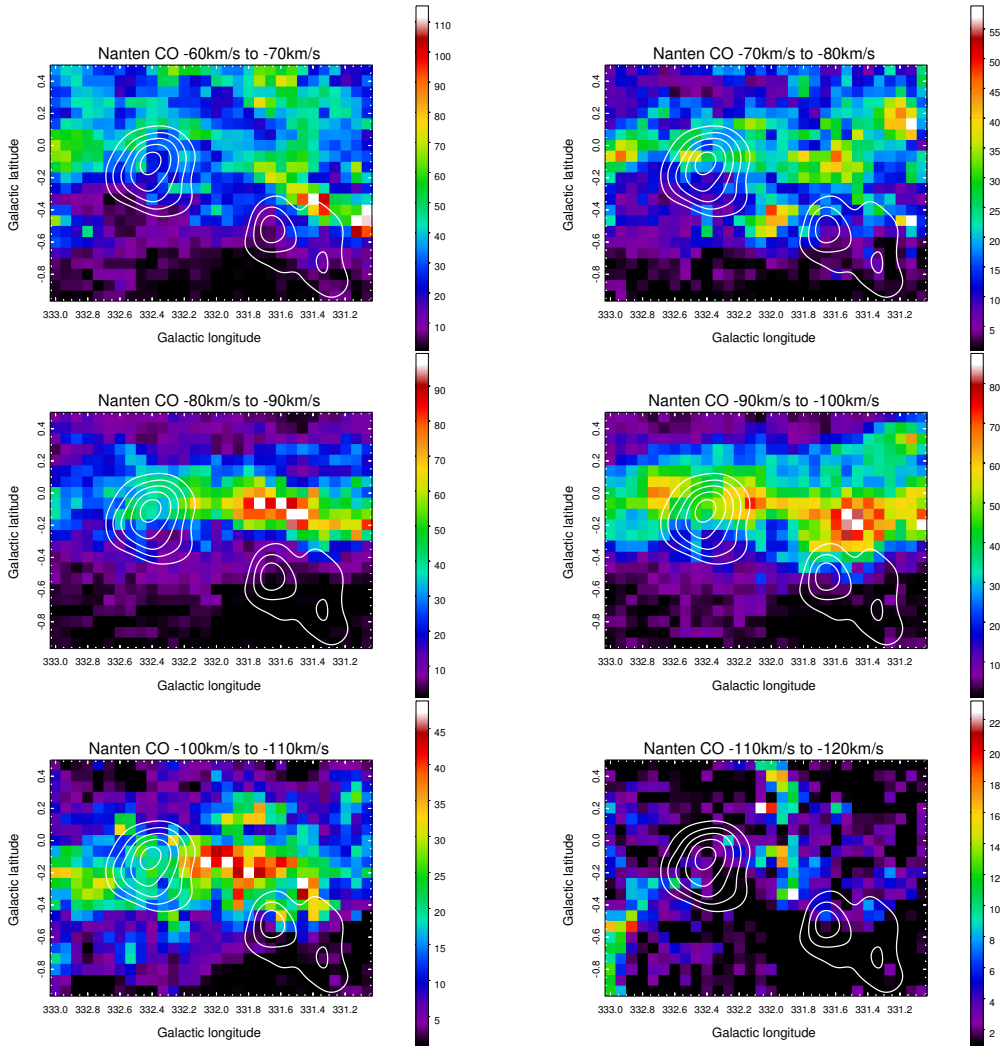

Figure 4.7: Integrated 10km/s maps from -60 km/s to -120 km/s of CO data from the Nanten telescope where the HESS TeV gamma-ray excess counts contours are shown in white. The axes are in units of degrees while the colour scale is in Kelvin.

4.1.5 MALT-45 and the Mopra Telescope 7 mm Emission

The MALT-45 survey of CS, $C^{34}S$ and SiO molecules is complementary to additional Mopra 7 mm mapping observed for this thesis (Jordan et al., 2015) although it has a higher sensitivity (see Table 3.2). For CS, the two data sets were combined using `Montage` such that they had the same sensitivity. The data were then cropped in galactic longitude to only cover the region spanning 331° to 333° which contains the HESS sources. Integrated maps of CS in 10 km/s intervals for velocities spanning 0 km/s to -120 km/s are shown in Figures 4.8 and 4.9. Integrated 10 km/s maps of other 7 mm molecules are presented in Appendix B including $C^{34}S$ and SiO.

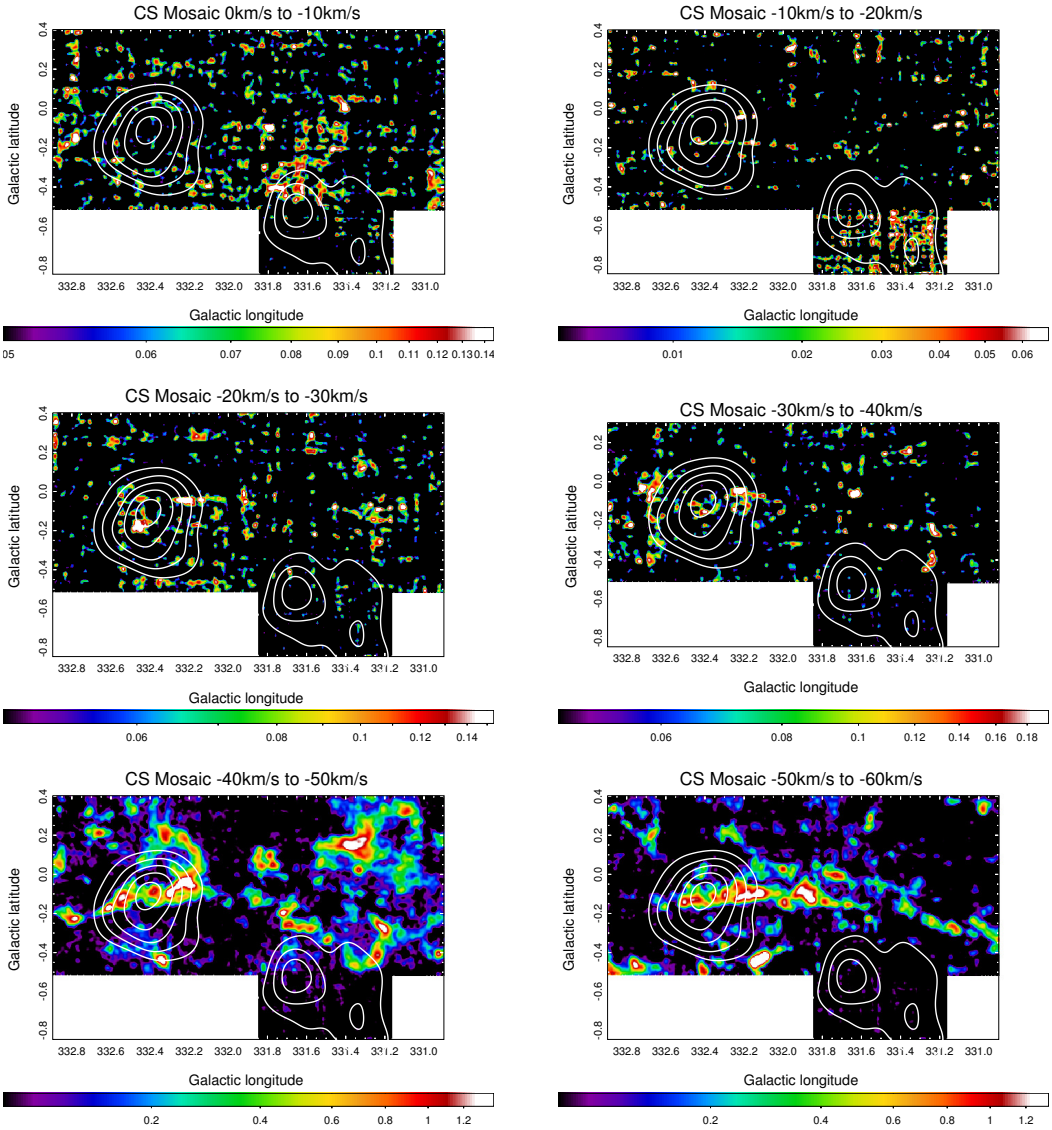

Figure 4.8: Mosaic of CS data from MALT-45 and the Mopra telescope over 10 km/s integrated ranges from 0 km/s to -60 km/s. The axes are in units of degrees while the colour scale is in Kelvin.

There is significant CS emission near HESS J1616-508 particularly in the -40 km/s to -60 km/s velocity range. In the -40 km/s to -50 km/s integrated Figure, there is a ring of CS emission in the upper half of the HESS J1616-508 TeV contours. Since the density required to produce CS emission is high, there must be a very energetic process occurring in order to blow out a CS bubble. Such a process could also be responsible for the acceleration of CR particles and hence the production of gamma-rays. There is no indication of CS emission near HESS J1614-518 with very little overlap. This is expected

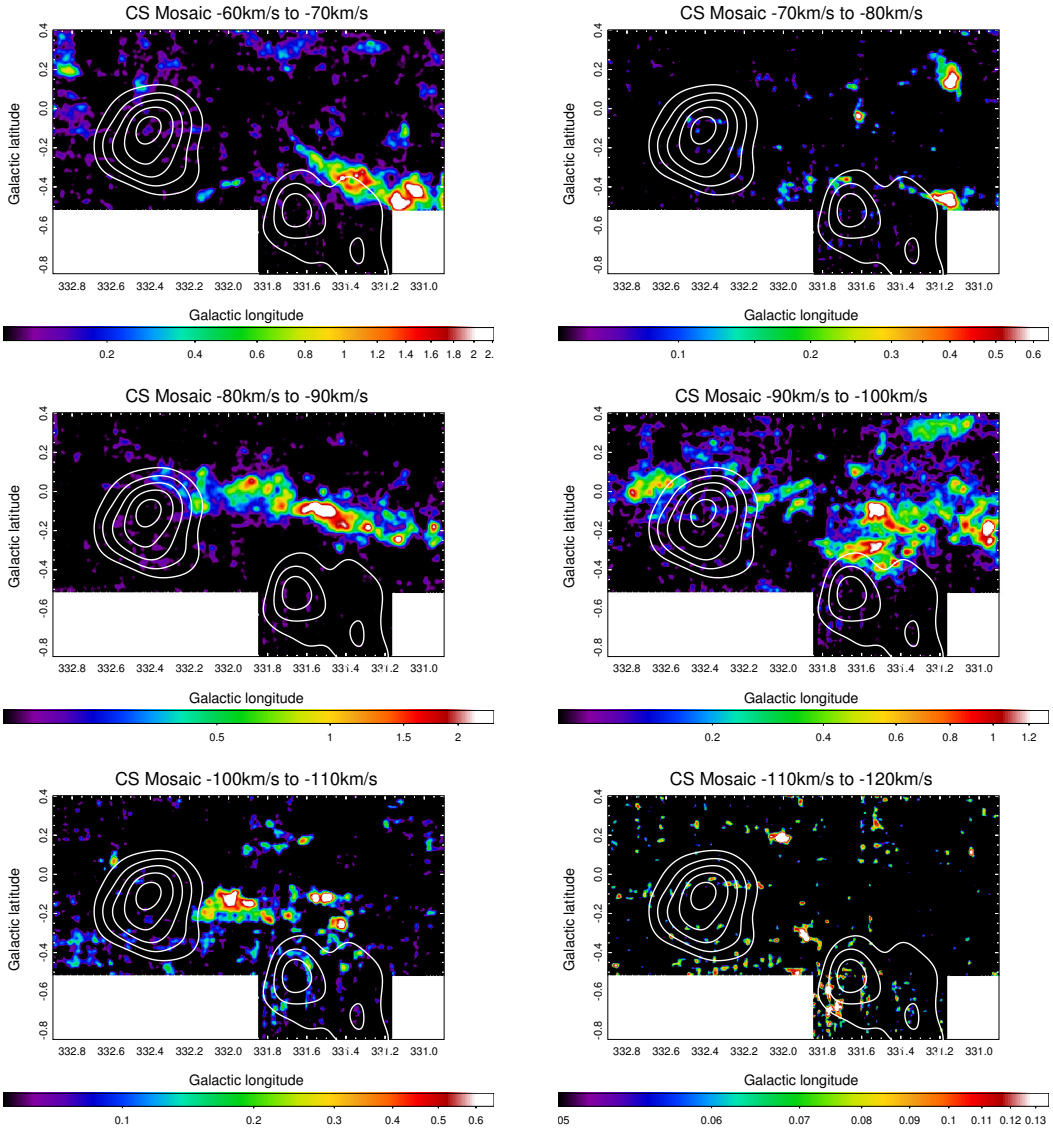

Figure 4.9: Mosaic of CS data from MALT-45 and the Mopra telescope over 10 km/s integrated ranges from 0 km/s to -60 km/s. The axes are in units of degrees while the colour scale is in Kelvin.

to a degree considering the displacement of the HESS TeV gamma-ray source from the galactic plane.

The CS data has been used in this project to identify dense molecular cores. However, it is also possible to calculate the column density, mass, density and optical depth given the presence of CS and $C^{34}S$ following the process described in Chapter 3. Future work on the ISM surrounding the HESS TeV gamma-ray sources includes extending the study of CS beyond morphological considerations into spectral analysis. If the density of the molecular

cores is known, then that information can be used to improve diffusion calculations which in this study assume that the density through a molecular cloud is constant. However, molecular clouds have a gradient density which can provide more information about the gamma-ray morphology expected from the collision of CRs with low energy ISM particles.

4.1.6 Southern Galactic Plane Survey

The continuum data from SGPS is useful in determining regions where interference from radio continuum sources may have occurred. Thus the continuum data from SGPS is shown in Figure 4.10. Several continuum regions can be seen to overlap with HESS J1616-508 while HESS J1614-518 is not associated with any.

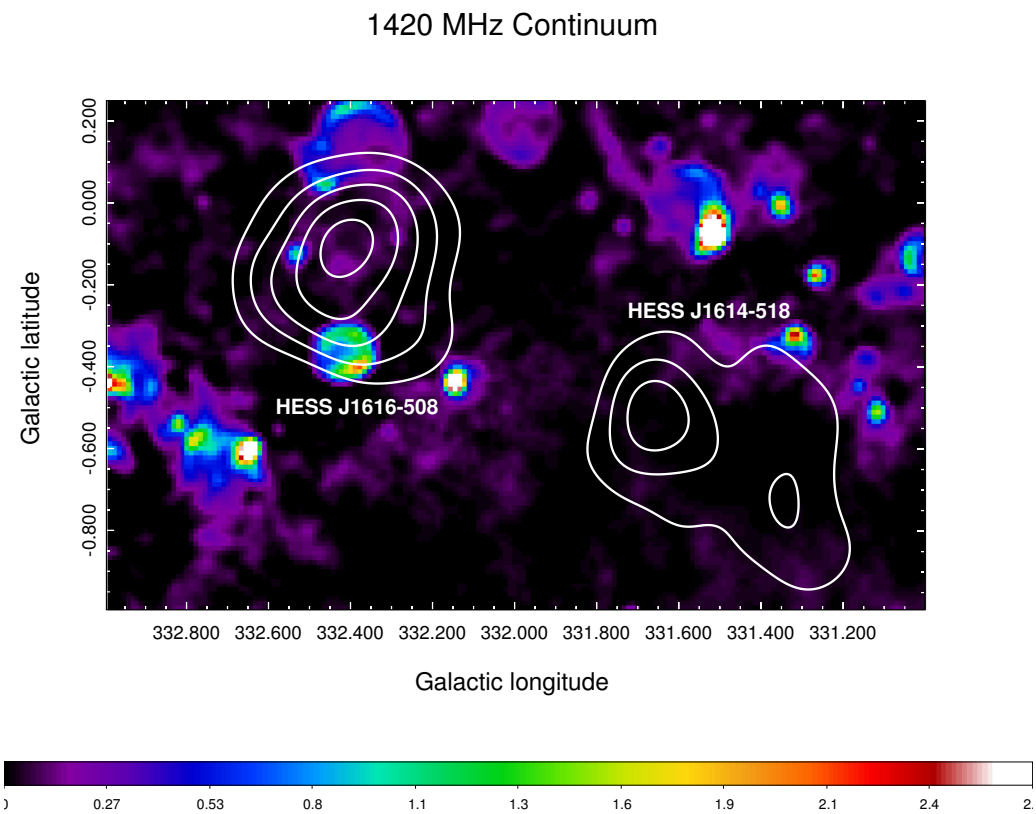

Figure 4.10: The continuum map from the SGPS survey at 1420 MHz with the excess HESS TeV gamma-ray contours in white (Haverkorn et al., 2006). The axes are in units of degrees while the colour scale is in Jy/beam.

The continuum subtracted data integrated from 0 km/s to -120 km/s in 10 km/s inter-

vals are shown in Figure 4.11 and Figure 4.12 (McClure-Griffiths et al., 2005). There is significant emission throughout the survey region. In particular, the velocity range from −20 km/s to -40 km/s and -90 m/s to -100 km/s show that there is significant HI emission which overlaps most of the HESS TeV gamma-ray emission from HESS J1616-508. Continuum source contamination can be seen in many of the integrated ranges with lines of emission radiating outwards. The figures also show that HESS J1616-508 is normally covered by HI emission except in the last integrated image frame. HESS J1614-518 is partially covered with some ranges such as the -20 km/s to -30 km/s and -50 km/s to -60 km/s velocity ranges, indicating minimal HI emission.

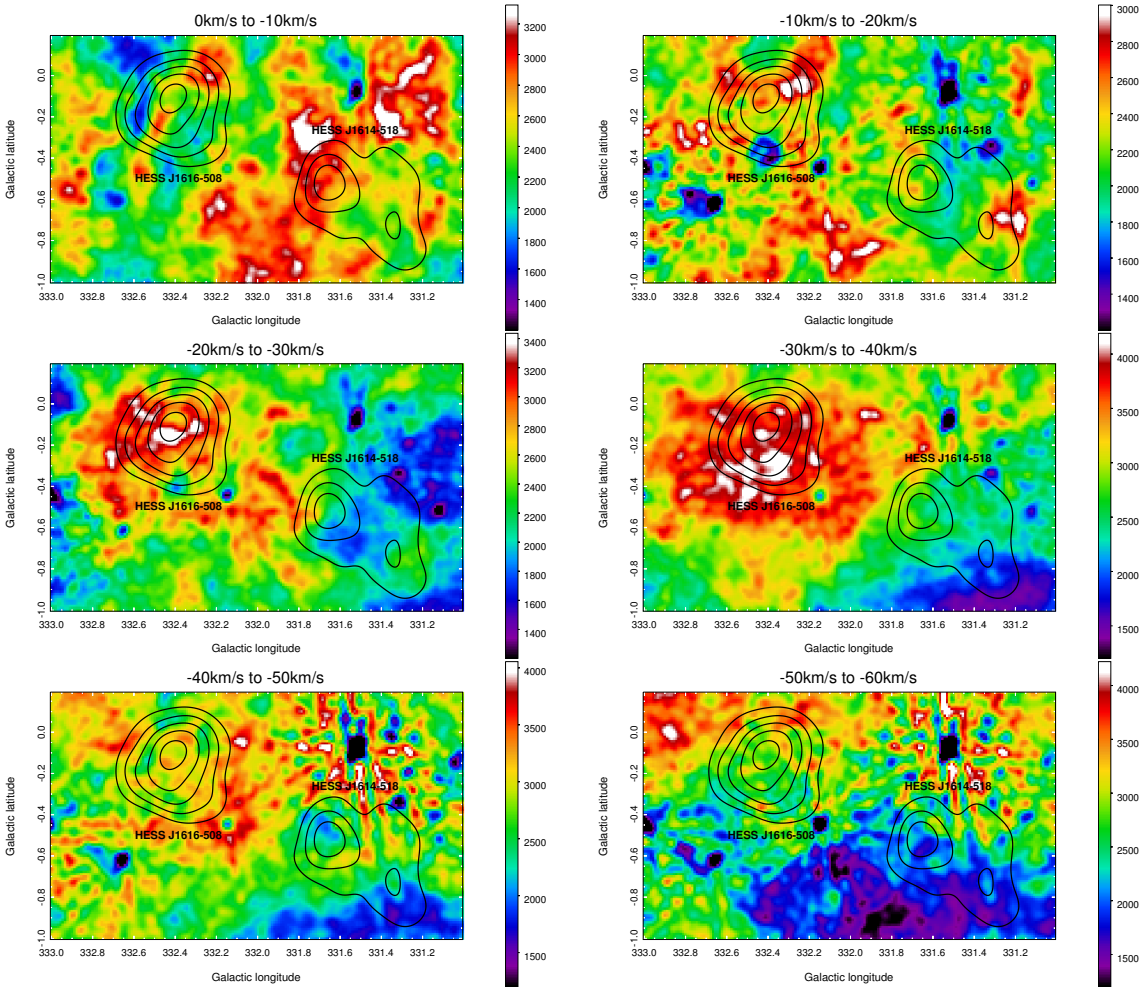

Figure 4.11: Integrated maps of HI from 0km/s to -60km/s in 10km/s intervals. The excess HESS contours are shown in black. The axes are in units of degrees while the colour scale is in Kelvin.

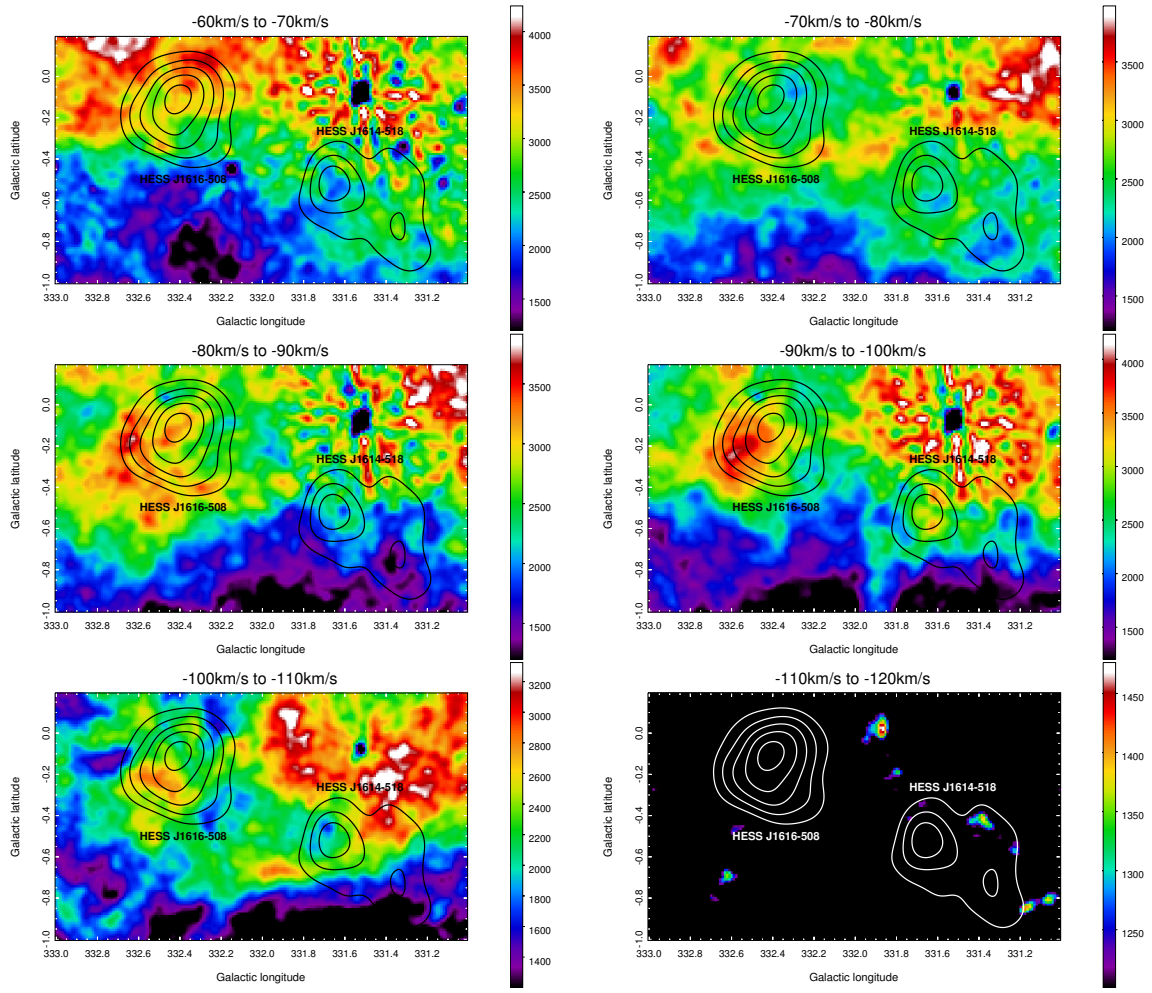

Figure 4.12: Integrated maps of HI from -60km/s to -120km/s in 10km/s intervals. The excess HESS contours are shown in black. The axes are in units of degrees while the colour scale is in Kelvin.

4.1.7 Molonglo 843 MHz Galactic Plane Survey

The Molonglo Galactic Plane Survey (MGPS) was carried out by the Molonglo Observatory Synthesis Telescope (MOST) at 843 MHz (Green et al., 1999). The data spanning the HESS sources is shown in Figure 4.13 on a linear scale with the VHE contours.

MGPS is useful in identifying features in the interstellar medium such as supernova remnants or regions of ionised hydrogen. From the Figure, a number of shell-like features are visible. Some of these trace the shocks of three known SNRs.

Note that similar caution has to be applied to MGPS data as was used when examining infrared data with regards to spatial coincidence. This is particularly important since

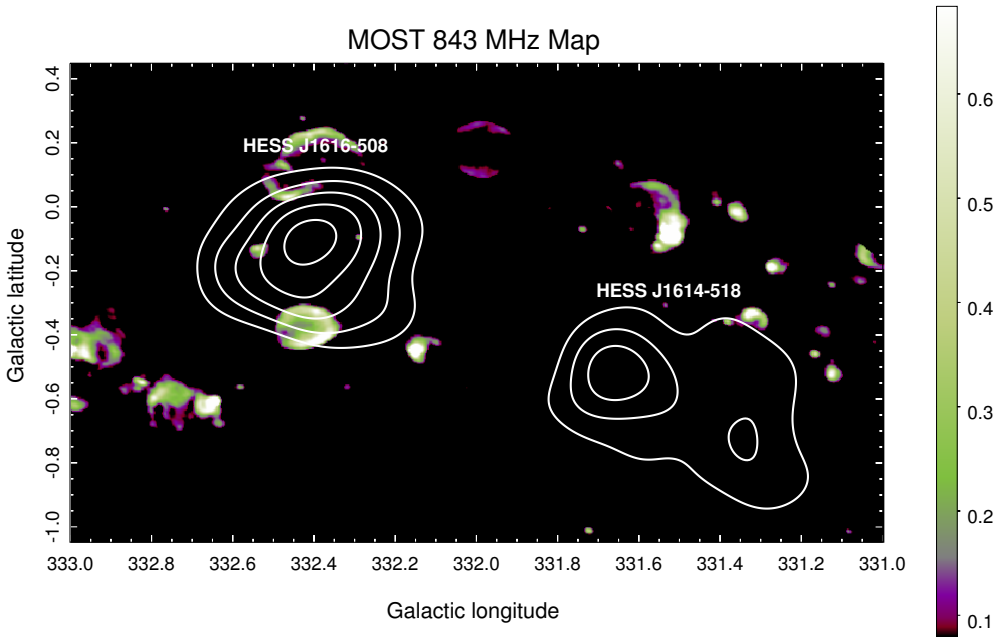

Figure 4.13: MGPS 843 MHz map of the region spanning HESS J1616-508 and HESS J1614-518 with excess HESS TeV gamma-ray contours. The colour scale is in units of Jy/beam.

MOST is sensitive enough to detect background galaxies which are evidenced as small unresolved features as well a radio galaxies (Green et al., 1999).

MGPS can be used in comparison with the 8 μm data from the Spitzer space telescope to identify regions dominated by non-thermal processes. This is due to the Spitzer data tracing mainly thermal emission. Regions of strong 843 MHz emission which are lacking in infrared emission would suggest dominant non-thermal processes are occurring. This can then be confirmed by examining X-ray data. Regions where this might occur are in the shocks of SNRs.

4.1.8 Infrared Emission from the Spitzer Space Telescope

The HESS sources, HESS J1616-508 and HESS J1614-508 have been observed by the Spitzer space telescope at a wavelength of 8 μm (Churchwell et al., 2009). Figure 4.14 presents the infrared data on a logarithmic scale to highlight features of lower emission. It is also shown with the HESS contours and HII regions.

The 8 μm emission traces excited polycyclic aromatic hydrocarbons (PAHs) which are one

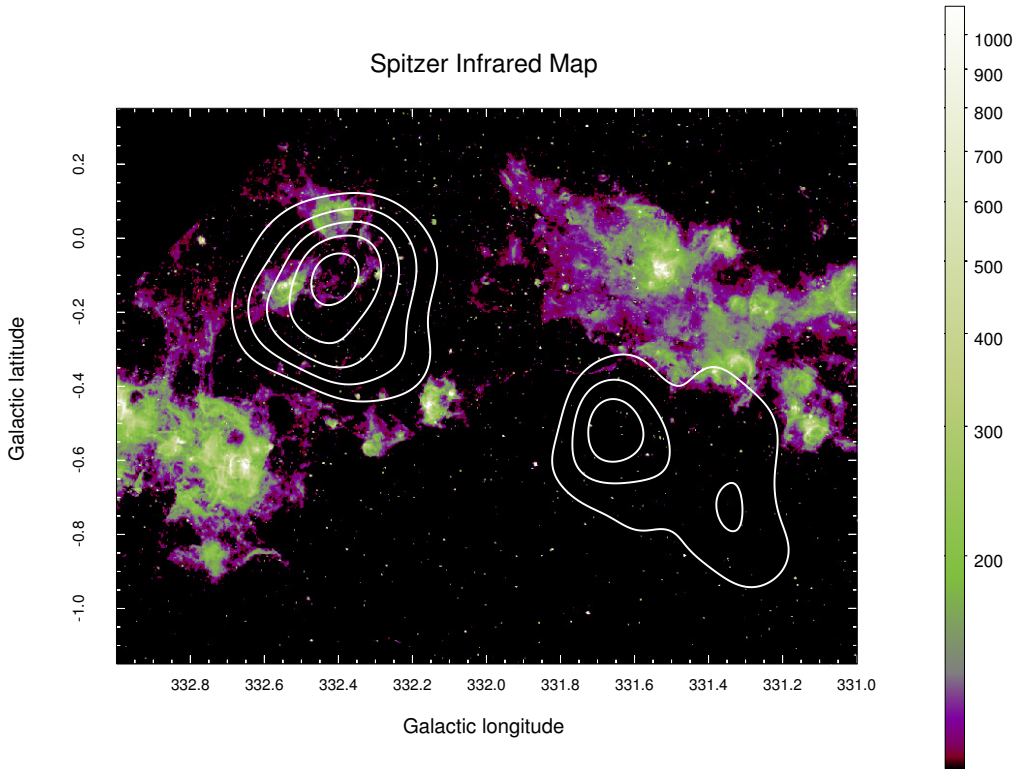

Figure 4.14: Infrared 8 μm emission towards HESS J1616-508 and HESS J1614-518 with excess HESS contours. The logarithmic colour scale is in units of MJy/sr while the axes are in units of degrees.

of the chemicals involved with the formation of life. The extensive emission here indicates that there are many star forming regions present. Thus, extensive infrared emission at 8 μm indicated regions of intense star formation and possible high energy processes which could result in the acceleration of CRs although some caution should be applied when examining the Spitzer data in comparison to the data cubes since the infrared emission contains emission from all velocities through the galaxy.

4.1.9 Mopra Ammonia Mapping Observations

Similarly, the 12 mm data was observed using the Mopra mapping technique. The mapping was designed to complement HOPS 12mm mapping of the galactic plane, although the data from this survey is not presented in this work. The 10 km/s interval integrated maps for all 12 mm molecules are presented in appendix B. No gas was detected in any 12 mm molecule within the 0 km/s to -120 km/s Mopra maps.

4.2 Summary

A variety of gases including isotopologues of CO, CS, NH_3 and HI, have now been observed towards HESS J1616-508 and HESS J1614-518, in addition to the gamma-rays observed by the HESS and Fermi-LAT telescopes. The main gas of interest in the following chapters is ^{12}CO since this gas is commonly used to trace dark H_2. The Mopra CO survey was primarily used since the resolution is significantly better than the Nanten CO observations. 38 CO RoI in the area towards HESS J1616-508 and HESS J1614-518 were identified and their mass and density were calculated. The CO gas morphology in the CO RoI can now be compared to other observed gases including HI, ^{13}CO and CS in addition to the radio 843 MHz and infrared 8 μm emission.

Chapter 5

Relation of ISM to Potential Cosmic Ray Accelerators

The CO (1–0) data now provides sufficient information that a study of the ISM towards specific potential particle accelerators becomes possible. These objects, which include pulsars, SNRs, WR stars and a stellar cluster, could potentially accelerate CR protons or electrons. The study of the ISM could indicate the type of particle the sources are accelerating if they are related to the HESS TeV gamma-rays sources HESS J1616-508 and HESS J1614-518. In this chapter, we select the CO RoI which are in the kinematic velocity range of the potential CR accelerators and discuss in detail the morphology of the gas.

5.1 HESS J1616-508

PSR J1617-5055

The pulsar PSR J1617-5055 is considered to be the most likely candidate for the gamma-ray emission from HESS J1616-508. The pulsar is estimated to be $\approx$ 6.5 kpc away (Kargaltsev et al., 2009). The velocity that the distance corresponds to is -107 km/s. The ^{12}CO, ^{13}CO, HI and CS data was integrated over a 10 km/s range surrounding the

velocity distance of the pulsar from −102 km/s to −112 km/s. These maps are shown in Figure 5.1 with the 8 μm emission. A column density map of the protons in the region was also made using the Mopra ^{12}CO and HI data. This is presented in Figure 5.2. The pulsar is also within the same velocity range of RCW 103, discussed in the next section, which has been suggested as being associated with PSR J1617-5055 due to their spatial and distance correlations (Kaspi et al., 1998).

It can be seen that there is no infrared or 843 GHz radiation as well as little ^{13}CO. The HI emission does show denser clouds on each side of the pulsar, towards and away from the center of the HESS TeV emission. There is also ^{12}CO emission surrounding the pulsar. From the column density map shown in Figure 5.2 it can be seen that the mass of H_2 from ^{12}CO emission dominates the mass of HI. The column density, mass and density of the CO (1–0) RoI are shown in table 5.1.

SNR RCW 103

The SNR RCW 103 has been suggested as being associated with PSR J1617-5055 and is sufficiently close to the HESS source to be considered as an accelerating source of CRs. It is located at a distance of 6.7 kpc (Pavlovic et al., 2014), although a spatially coincident void in the −10 km/s to −20 km/s map of HI, shown in Figure 5.3 could indicate a closer distance of approximately 1 kpc. This analysis will use the currently published distance for the RCW 103. However, the relation of the HI gas to the SNR and the implications on the distance needs to be investigated in the future.

Previous studies of the SNR in X-rays have found that the SNR is very strong emitter in that wavelength. The shell is clearly visible and spherically homogeneous. There also seems to be a source of X-rays emitted from the center of the SNR which has been speculated to be a central pulsar object (De Luca et al., 2008). Thus suggesting that the association with PSR J1617-5055 is not possible. The SNR's distance from the gamma-ray source has suggested that it is too far away to be associated. However, while it is unlikely that the SNR is a counterpart to the gamma-ray emission, the ISM surrounding

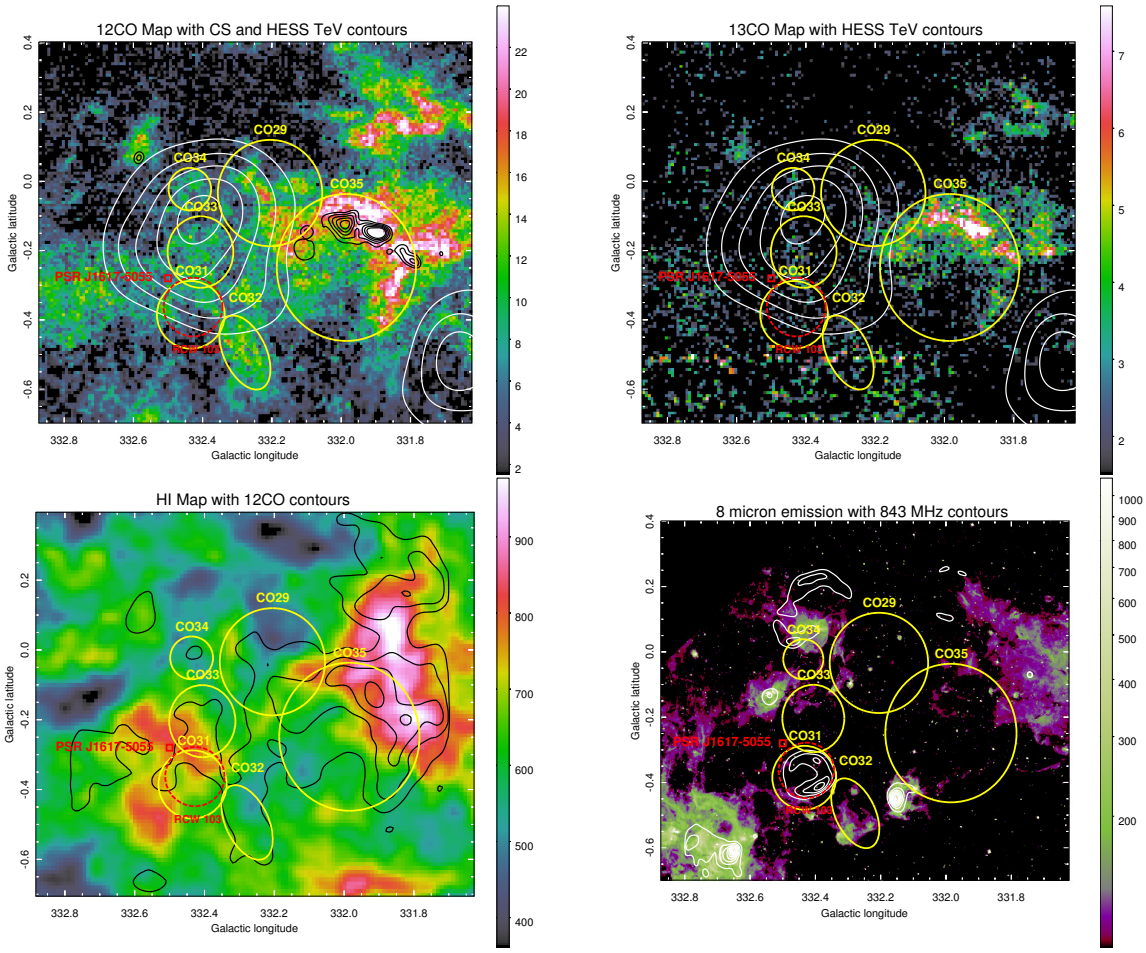

Figure 5.1: The area surrounding the pulsar PSR J1617-5055 and RCW 103 roughly centred on HESS J1616-508. The top left panel shows the ^{12}CO map with the RoI CO (1–0) regions marked in yellow. The potential accelerators are shown in red. HESS TeV contours are shown in white and CS (1–0) contours are in black. The top right panel shows the ^{13}CO emission presented the same as the ^{12}CO emission omitting the CS (1–0) contours. The bottom left panel shows the HI emission with the ^{12} CO contours in black along with the RoI CO (1–0) in yellow and the potential accelerators in red. The bottom right image shows the 8 μm Spitzer map with the 843 MHz emission as white contours. Again, RoI are shown in yellow and potential accelerators are marked in red. The CO and HI data was integrated between -102 km/s and -112 km/s. The axes are all in units of degrees while the colour scale for the 12CO, 13CO and HI emission in in Kelvin. The colour scale for the infrared emission is in MJy/sr.

it is still considered in order to build a complete understanding of the potential targets for CR interactions.

The emission from ^{12}CO, ^{13}CO, HI and CS, presented in Figure 5.1, was integrated between -102 km/s and -112 km/s which spans the 5 km/s each side of the published kinematic velocity of the SNR. A column density map of the protons in the region was

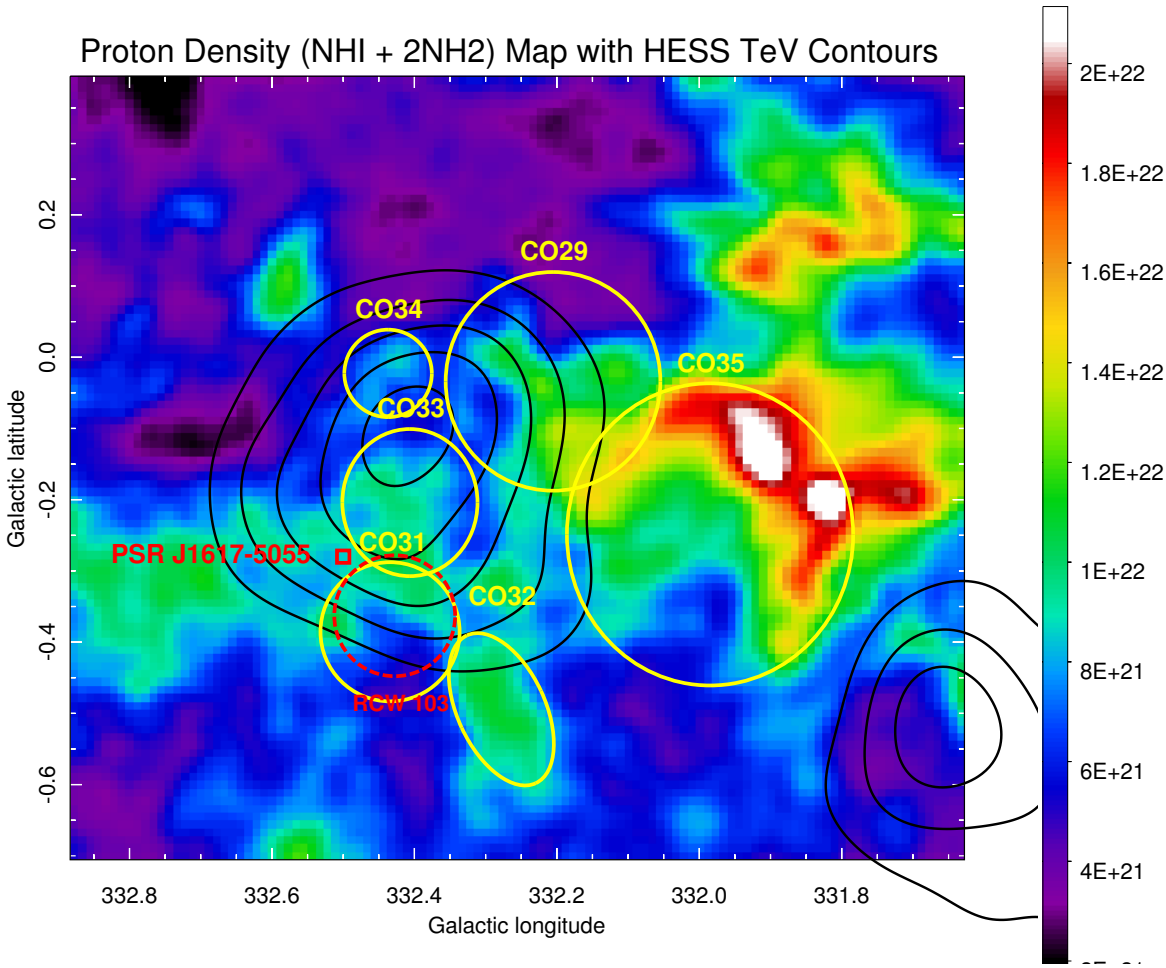

Figure 5.2: The column density map of hydrogen gas towards PSR J1617-5055, RCW 103 and HESS J1616-508. The CO (1–0) RoI are marked as yellow ellipses while the HESS TeV contours are black. PSR J1617-5055 and RCW 103 are labelled in red. The map was made from the sum of the HI column density and twice the H_2 column density calculated from CO (1–0).

also made using the Mopra ^{12}CO and HI data. This is presented in Figure 5.2.

The ISM suggests the possibility of a shell in this velocity range which is seen in HI, CO and the column density map with a hollow of lower emission towards the center of the SNR. There is also gas between the SNR and the center of the gamma-ray emission. However, this could just be due to the emission from a spiral arm which passes through the region. There is no infrared emission which lines up with the supernova shell which is very visible in the 843 GHz continuum. RCW remains an interesting feature due to the significant amount of gas in the region despite the lack of association with PSR J1617-5055. The column density, mass and density of the regions are presented in table 5.1.

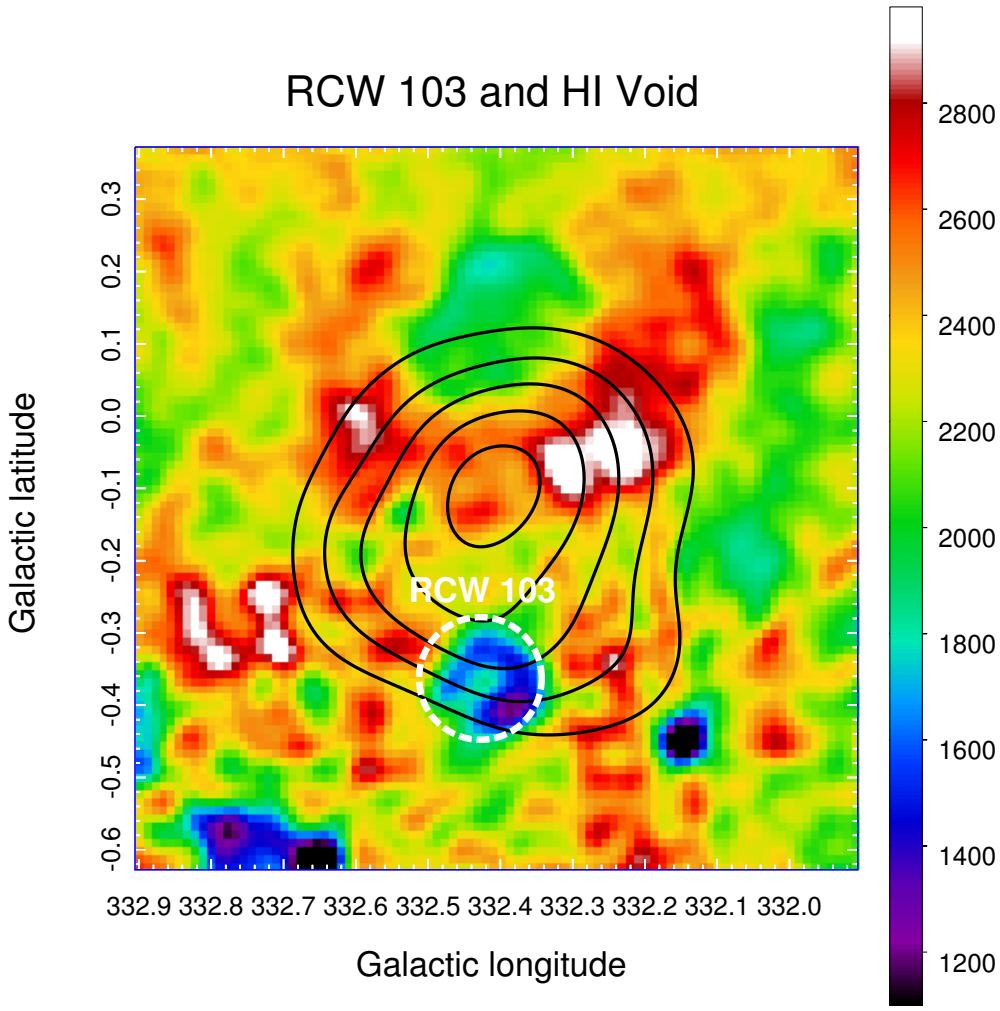

Figure 5.3: HESS J1616-508 contours in black and the position of RCW 103 in white are shown on the HI data from the velocity interval between −10 km/s and −20 km/s. There is a void in the HI coincident with the location of the SNR. The scale is in units of Kelvin.

SNR Kes 32

The SNR Kes 32 is estimated to have a distance of 5.5 kpc (Pavlovic et al., 2014) and is located towards the northern side of HESS J1616-508. Recent literature suggests that an association between Kes 32 and the HESS source is unlikely due to the spatial separation. However, the situation is worth investigating due to the still uncertain distance of the HESS source and the SNR. Indeed the HI data integrated between the velocity range of −10 km/s and −20 km/s has a void coincident with the location of Kes 32 suggesting a distance of 1 kpc which is shown in Figure 5.4. The distance used for the SNR in this

thesis is the published value although the relation between the HI void and the SNR needs to be investigated in the future.

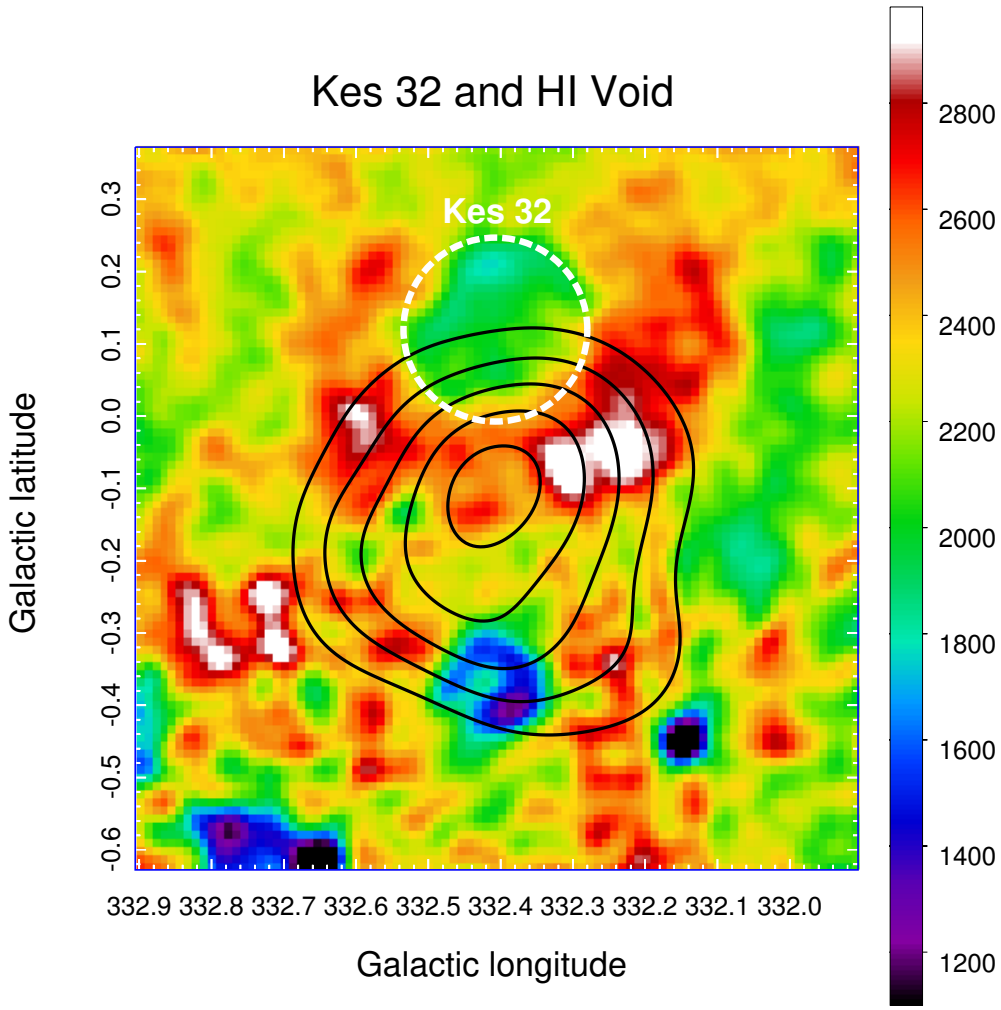

Figure 5.4: HESS J1616-508 contours in black and the position of Kes 32 in white are shown on the HI data from the velocity interval between −10 km/s and −20 km/s. There is a void in the HI coincident with the location of the SNR. The scale is in units of Kelvin.

The gas data integrated across −80 km/s to −90 km/s for the kinematic distance of 5.5 kpc, is shown in Figure 5.5. A column density map of the protons in the region was also made using the Mopra ^{12}CO and HI data. This is presented in Figure 5.6.

The two isotopologues of CO and HI emission reveal diffuse gas covering the northern half of HESS J1616-518. There is the suggestion of a HI shell around Kes 32 but that is not present in ^{12}CO. There is a denser region of gas to the right of the gamma-ray contours which contains dense cores of CS gas. The SNR shell is also visible in the 843

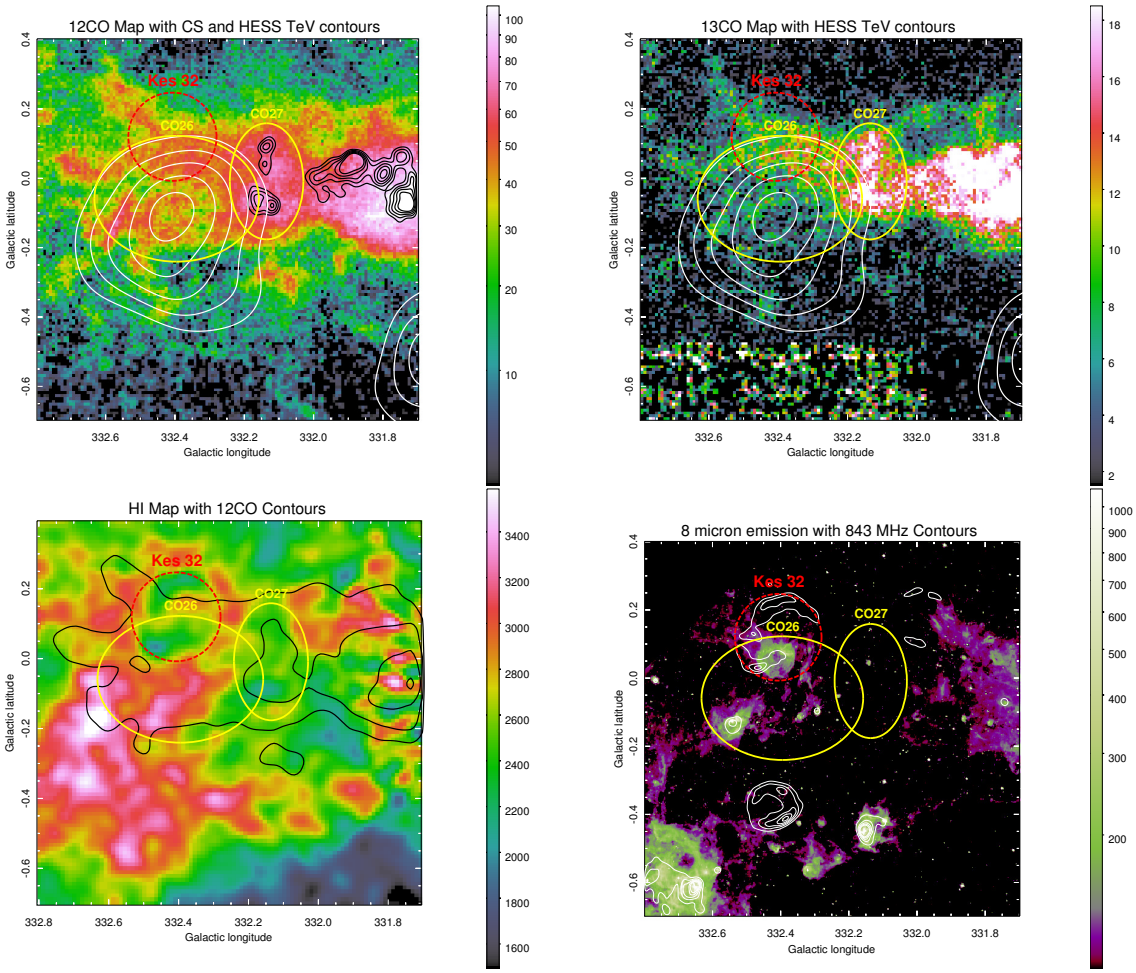

Figure 5.5: The area surrounding the SNR Kes 32 roughly centered on HESS J1616-508. The top left panel shows the ^{12}CO map with the RoI CO (1–0) regions marked in yellow. The potential accelerators are shown in red. HESS TeV contours are shown in white and CS (1–0) contours are in black. The top right panel shows the ^{13}CO emission presented the same as the ^{12}CO emission omitting the CS (1–0) contours. The bottom left panel shows the HI emission with the ^{12} CO contours in black along with the RoI CO (1–0) in yellow and the potential accelerators in red. The bottom right image shows the 8 μm Spitzer map with the 843 MHz emission as white contours. Again, RoI are shown in yellow and potential accelerators are marked in red. The CO and HI data integrated between -80 km/s and -90 km/s. The axes are all in units of degrees while the colour scale for the 12CO, 13CO and HI emission is in Kelvin. The colour scale for the infrared emission is in MJy/sr.

GHz emission and has spatially matching 8 μm emission.

Column density, mass and density for the CO RoI are presented in table 5.1. Morphologically, the distribution of the gas overlapping with the HESS contours suggests that the SNR bears further investigation. However, it remains questionable as to why the gamma-ray emission would not coincide with the denser region of gas to the right if a

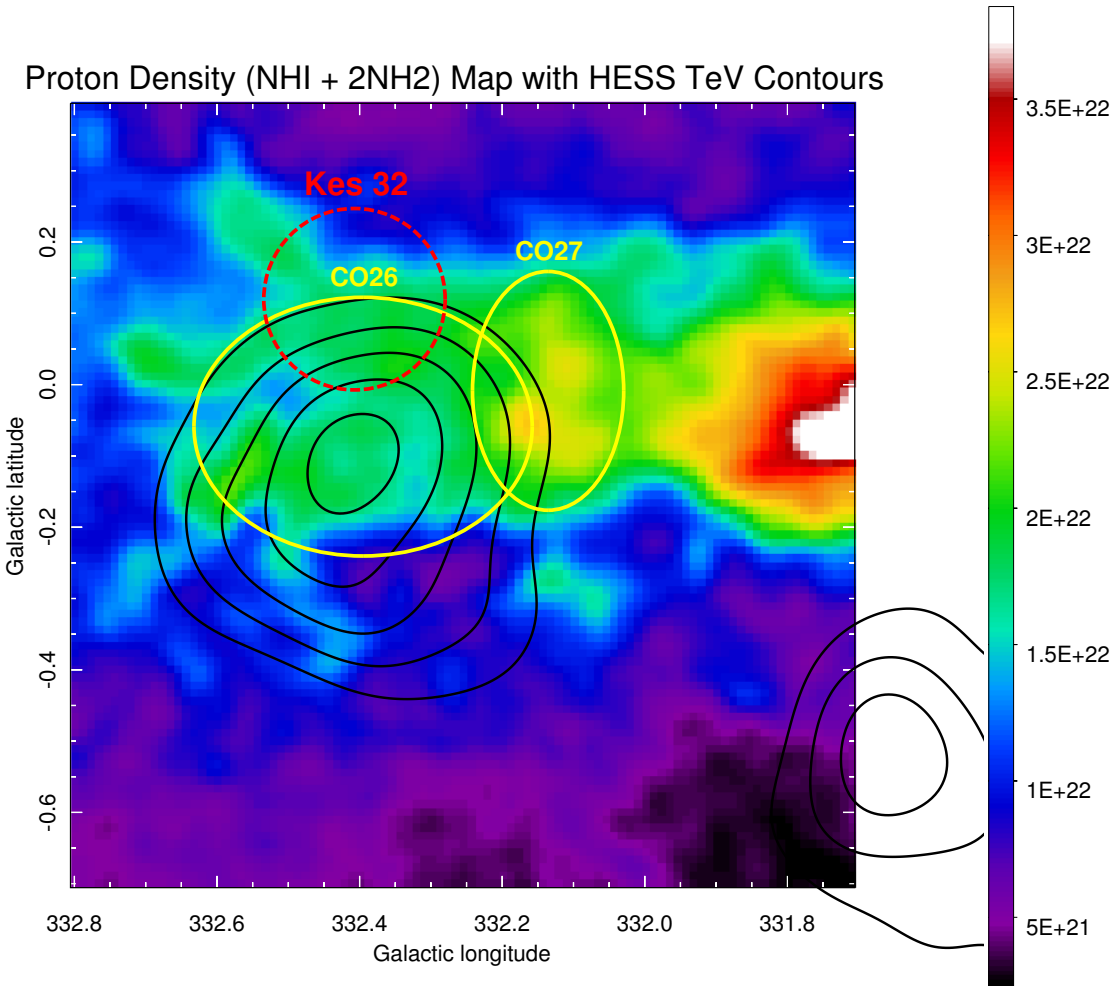

Figure 5.6: The column density map of hydrogen gas towards Kes 32 and HESS J1616-508. The CO (1–0) RoI are marked as yellow ellipses while the HESS TeV contours are black. PSR J1617-5055 and RCW 103 are labelled in red. The map was made from the sum of the HI column density and twice the H_2 column density calculated from CO (1–0).

hadronic scenario is considered with Kes 32 as the source of CRs. This will be discussed in more detail in Chapter 6.

SNR G332.0+0.2

SNR G332.0+0.2 is spatially the most distant accelerator from HESS J1616-508. Located at a distance of 7.4 kpc (Pavlovic et al., 2014), the SNR is considered to be a highly unlikely counterpart to the gamma-ray emission due to its spatial separation. However, it is included in this study for completeness. Similarly to the other SNR mentioned, there is a suggestion of a HI void that is spatially coincident with the SNR which exists at a distance of 2 kpc which is not in agreement with the published distance. This void is

located within the velocity range of −20 km/s to −30 km/s and is shown in Figure 5.7.

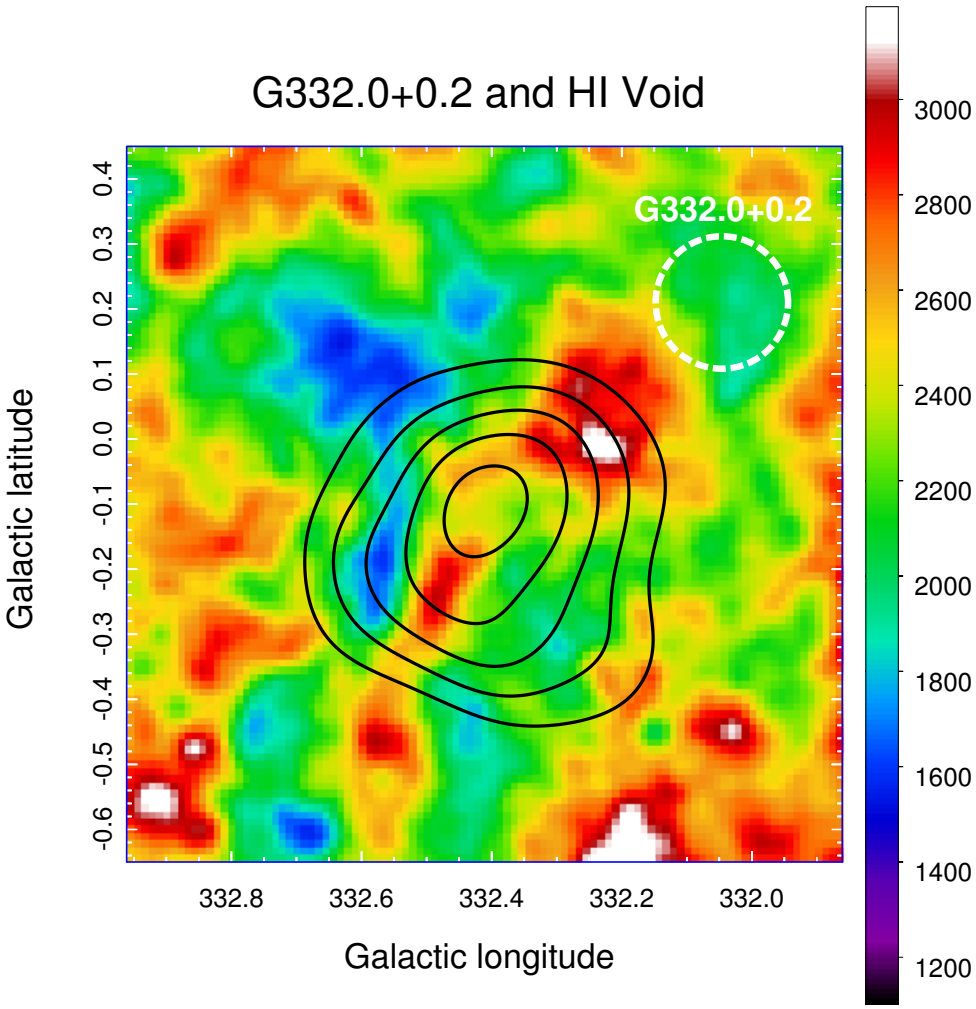

Figure 5.7: HESS J1616-508 contours in black and the position of G332.0+0.2 in white are shown on the HI data from the velocity interval between −10 km/s and −20 km/s. There is a void in the HI coincident with the location of the SNR. The scale is in units of Kelvin.

The CO, CS, HI, infrared and radio continuum data are presented in Figure 5.8. A column density map of the protons in the region was also made using the Mopra ^{12}CO and HI data. This is presented in Figure 5.9. The data is integrated across the kinematic velocity range of −100 km/s to −110 km/s which corresponds to a distance of 6.1 kpc. It can be seen that there is very little gas which could associate the SNR with the gamma-ray source. Similarly to RCW 103, the is no HI shell evident around the SNR. There is some indication of 843 GHz emission towards the SNR's location which does not have good spatial.

If the SNR is located within the specified velocity range, then from the morphology of the gas, it remains unlikely that there is any obvious association with the gamma-ray source. There are regions of very dense gas adjacent to the SNR and the HESS source such as the CO (1–0) shell marked by RoI CO35 which also contains bright CS emission. There is some gas overlapping with the gamma-ray source which lacks the dense CS emission and appears to contain less mass.

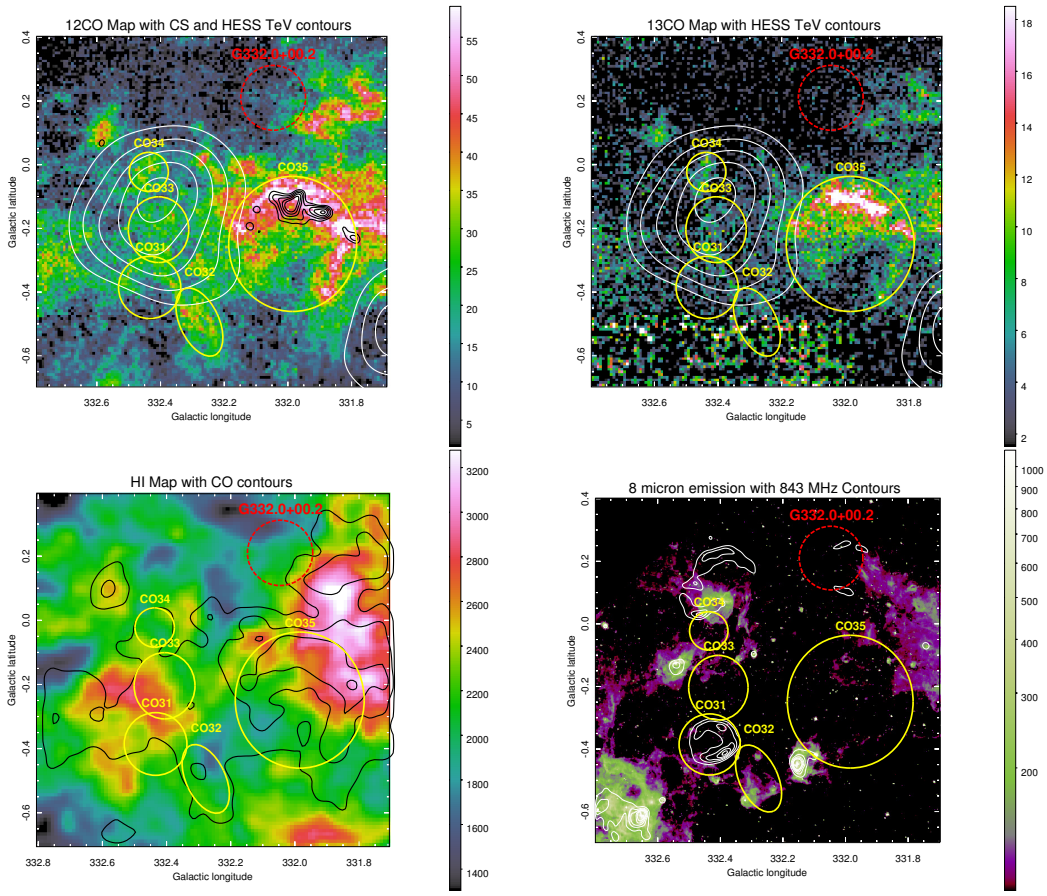

Figure 5.8: The environment of SNR G332.0+0.2 roughly centred on HESS J1616-508. The top left panel shows the ^{12}CO map with the RoI CO (1–0) regions marked in white. The potential accelerators are shown in yellow. HESS TeV contours are shown in white and CS (1–0) contours are in black. The top right panel shows the ^{13}CO emission presented the same as the ^{12}CO emission omitting the CS (1–0) contours. The bottom left panel shows the HI emission with the ^{12} CO contours in black along with the RoI CO (1–0) in white and the potential accelerators in yellow. The bottom right image shows the 8 μm Spitzer map with the 843 MHz emission as white contours. Again, RoI are shown in white and potential accelerators are marked in yellow. The CO and HI data was integrated between -100 km/s and -110 km/s.

The column density, mass and density of the regions presented in the Figure are shown

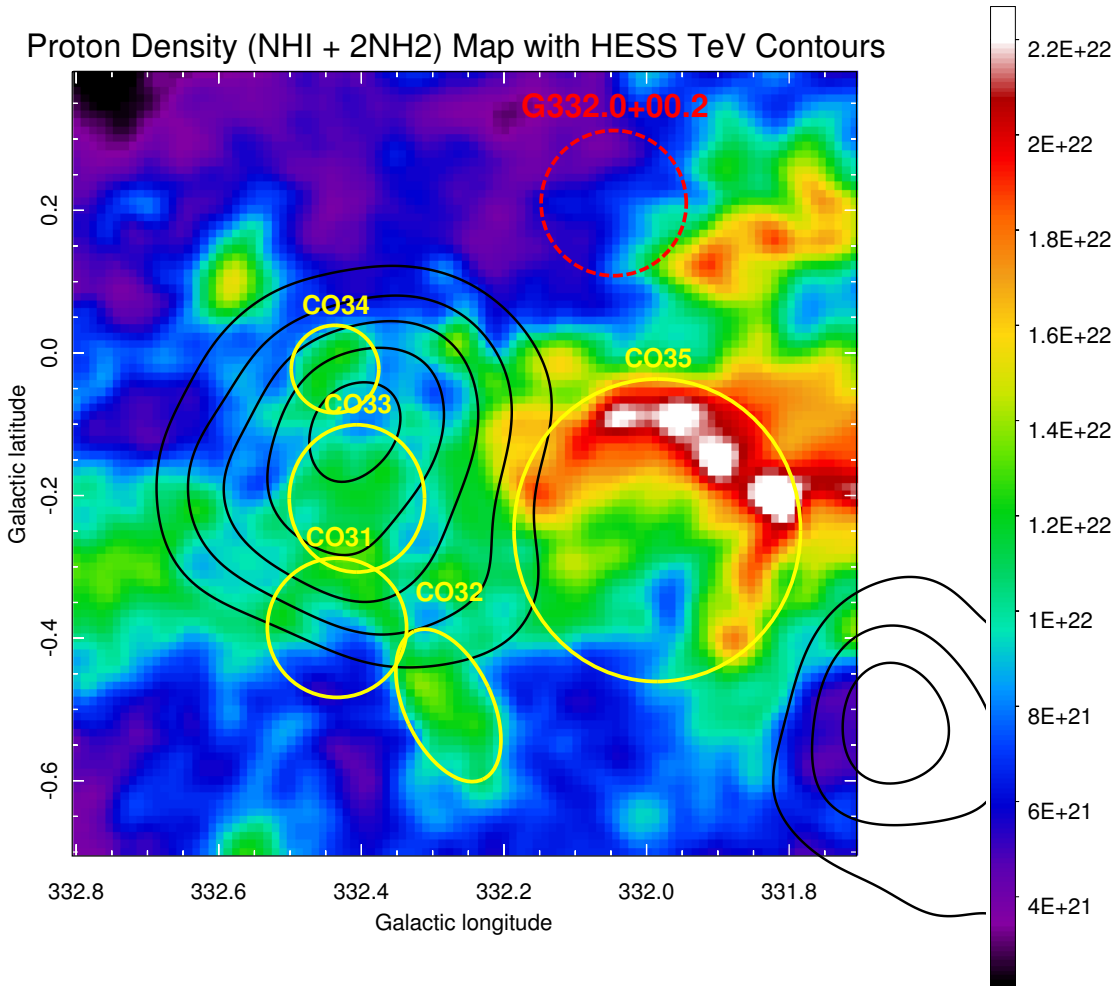

Figure 5.9: The column density map of hydrogen gas towards G332.0+0.2 and HESS J1616-508. The CO (1–0) RoI are marked as yellow ellipses while the HESS TeV contours are black. G332.0+0.2 is labelled in red. The map was made from the sum of the HI column density and twice the H_2 column density calculated from CO (1–0).

in table 5.1.

PSR J1614-5048

The pulsar PSR J1614-5048 is spatially located between the SNRs Kes 32 and G332.0+0.002. The pulsar is located at a distance of 7.2 kpc, has an age of 7.42×10^3 years and a spin down power of 1.6×10^{36} ergs s^{-1}. The distance of the pulsar results in a Doppler velocity of -113 km/s in this region of the galaxy. The pulsar has not been considered to be a counterpart for HESS J1616-508 due to its large distance from the center of the gamma-

ray emission.

Figure 5.10 presents the integrated maps of the CO, HI, CS, 8 μm infrared, and the 843 GHz in the region surrounding the pulsar and the HESS source. A column density map of the protons in the region was also made using the Mopra ^{12}CO and HI data. This is presented in Figure 5.11.

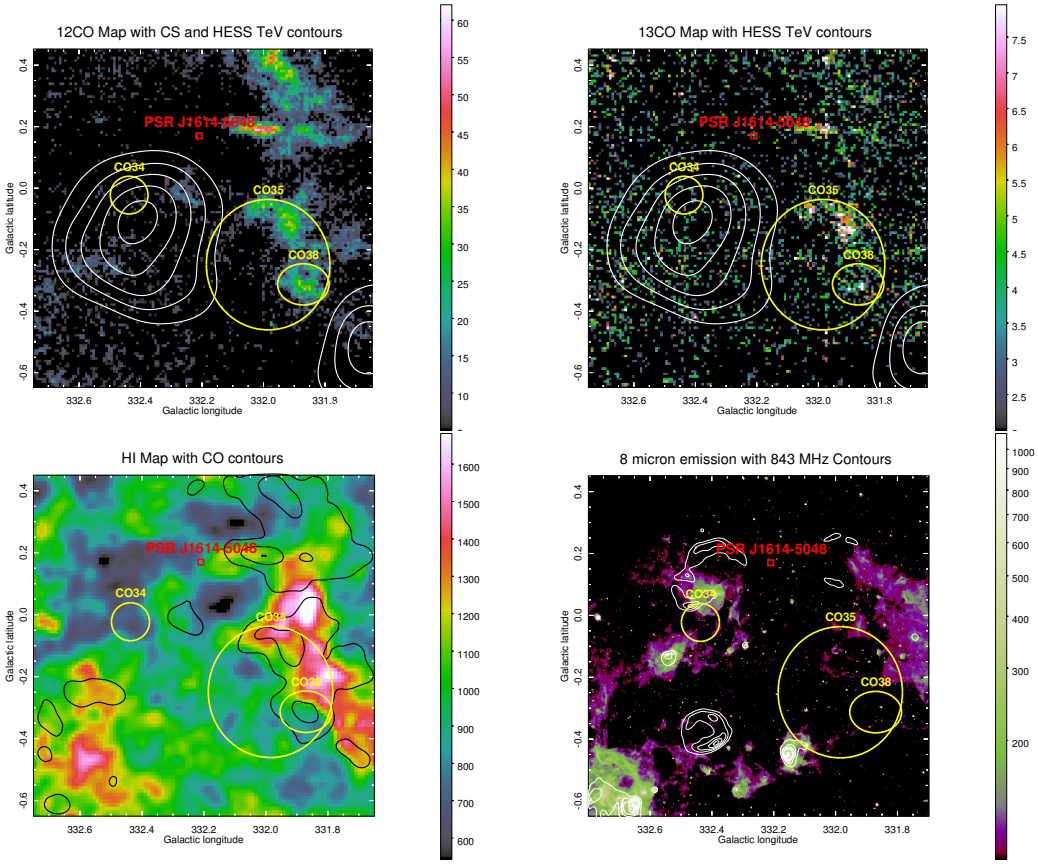

Figure 5.10: The area surrounding the pulsar PSR J1614-5048 roughly centred on HESS J1616-508. The top left panel shows the ^{12}CO map with the RoI CO (1–0) regions marked in white. The potential accelerators are shown in yellow. HESS TeV contours are shown in white and CS (1–0) contours are in black. The top right panel shows the ^{13}CO emission presented the same as the ^{12}CO emission omitting the CS (1–0) contours. The bottom left panel shows the HI emission with the ^{12} CO contours in black along with the RoI CO (1–0) in white and the potential accelerators in yellow. The bottom right image shows the 8 μm Spitzer map with the 843 MHz emission as white contours. Again, RoI are shown in white and potential accelerators are marked in yellow. The CO and HI data was integrated between -108 km/s and -118 km/s.

There is evidence for some ^{12}CO emission close to the pulsar although PWNe do not require gas to overlap the gamma-ray source. There is some diffuse HI gas within the gamma-ray contours close to the pulsar but it is not very dense since there is no ^{13}CO or

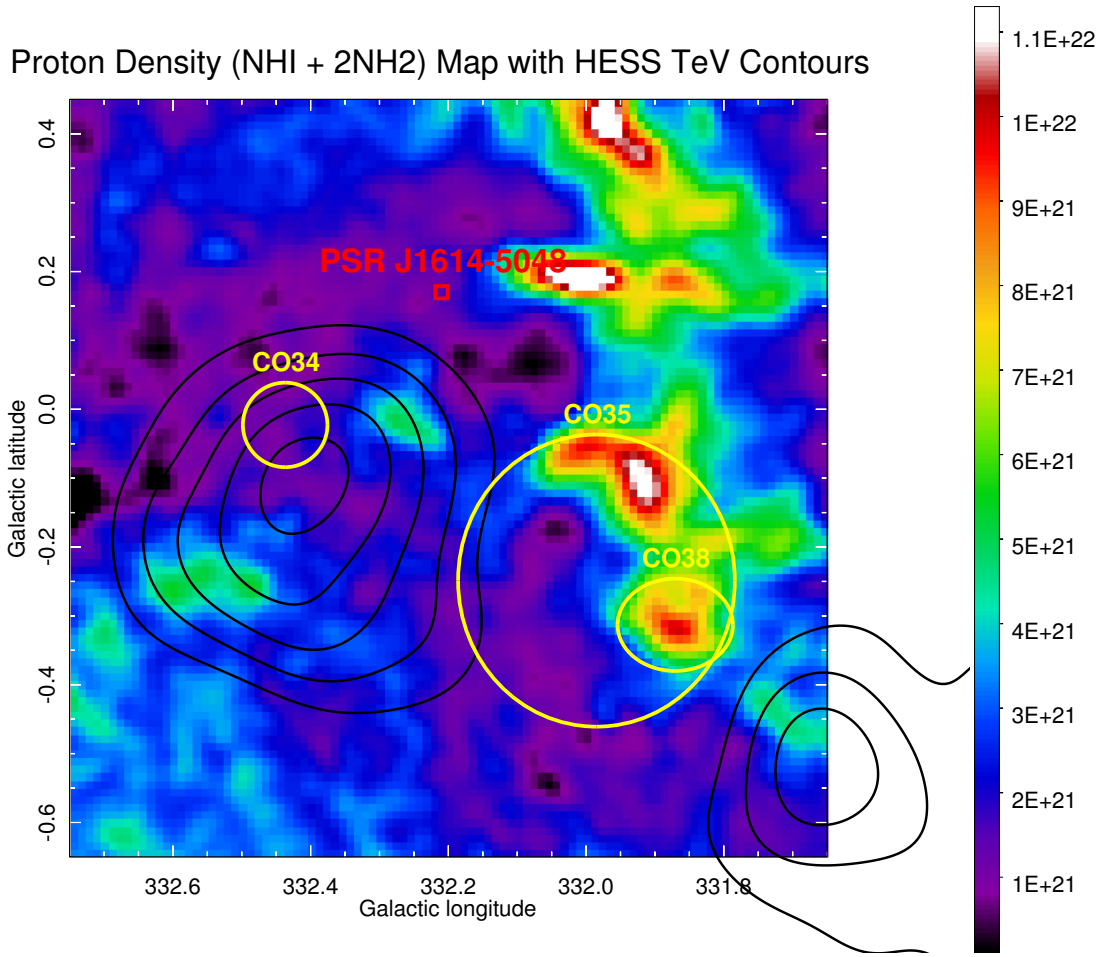

Figure 5.11: The column density map of hydrogen gas towards PSR J1614-5048 and HESS J1616-508. The CO (1–0) RoI are marked as yellow ellipses while the HESS TeV contours are black. PSR J1614-5048 is labelled in red. The map was made from the sum of the HI column density and twice the H_2 column density calculated from CO (1–0).

CS in the same region. However, this cloud poses a barrier to electrons travelling to the center of the gamma-ray emission. There is also no infrared or radio-continuum emission near the pulsar. There is some diffuse HI emission close to the pulsar. However, the proton density map is dominated by the CO emission.

Morphologically, it seems unlikely that PSR J1614-5048 could be involved in the production of gamma-rays. However, there is a possibility that particles accelerated by the pulsar could travel to the center of the gamma-ray emission where they release their energy. The column density, mass and density of the regions identified in the Figure are presented in table 5.1.

Region	Near d (kpc)	N_{H_2} $\times 10^{21}$	M ($\times 10^4 M_\odot$)	$n(H_2)$ (cm^{-3})
CO26	5.2	6.5	14.1	608
CO27	5.1	7.4	6.3	56
CO29	5.7	10.6	15	550
CO31	6.1	3.3	2.1	248
CO32	6.2	4.1	2.1	482
CO33	6.1	4.2	2.8	323
CO34	6.1	2.7	0.7	317
CO35	6.0	9.0	25.9	332
CO38	7.1	1.2	0.6	116

Table 5.1: Gas Parameters of CO RoI identified near HESS J1616-508. The column density, N_{H_2}, is in units of cm^{-2}. Errors are listed in the main parameter tables 4.7 and 4.8.

CO RoI Parameters

The near distance, column density, mass and particle density of the CO RoI near identified potential particle accelerators are shown in table 5.1.

5.2 HESS J1614-518

Pismis 22

Pismis 22 is though to be a counterpart to HESS J1614-518 although previous studies have found no evidence of significant overlapping gas towards the cluster using the Nanten CO (1–0) observations (Rowell et al., 2008). With the new Mopra CO (1–) data there is now a more sensitive probe of the molecular gas surrounding the cluster. In addition to the integrated map presented in Figure 5.12 deep pointings were made towards the cluster to attempt to find evidence of CS or ammonia emission.

The integrated maps of CO, HI and the column density show that there is very little molecular emission near the cluster between the integration range of -9 km/s and -19 km/s. The integration range was chosen to span ± 5 km/s either side of the cluster's kinematic distance of -13 km/s, which corresponds to the reported distance of 1 kpc

(Piatti et al., 2000). A column density map of the protons in the region was also made using the Mopra ^{12}CO and HI data. This is presented in Figure 5.13.

There is a reasonable amount of diffuse HI emission near the cluster which interestingly, overlaps with the peaks in the gamma-ray source. It should be noted that a continuum source located to the north of HESS J614-518 has distorted the data surrounding it as possible artefacts can be seen. If the cluster is accelerating particles which are protons, then it would be expected that there should be gas throughout the emission region of the HESS source with denser pockets near the northern and southern peaks. Whilst this morphology is apparent, it is only visible in the diffuse HI emission. The column density, mass and density of identified regions are presented in table 5.2.

The deep pointings towards Pismis 22 resulted in 6 spectra being obtained which contain information about a variety of molecules. In the 7 mm wavelengths, a single spectra looks at CS emission which could indicate dense molecular gas located within the cluster. Five 12 mm observations focus on attempting to detect NH_3 (1,1) which also can be present in stellar clusters. The spectra are presented in Figure 5.14.

The spectra from ammonia and CS towards Pismis 22 indicate that there was no emission. These observations were taken during cloudy conditions which could have influenced the 7 mm observations to a degree although 12 mm observations should not be affected by cloud. It is clear that there is no molecular emission from the cluster. There was no evidence for emission in any of the other 7 mm or 12 mm molecules.

PSR J1613-5211

PSR J1613-5211 is a 3.77×10^5 year old pulsar located at a distance of 6.1 kpc. In relation to the gamma-ray source HESS J1614-518, it is on the edge of the contours near the southern peak. The pulsar is not considered to be a main contributor towards particle acceleration for the gamma-rays due to its distance and it's weaker spin down power of 7.9×10^{33} ergs s^{-1} compared to the TeV luminosity of HESS J1614-518.

The integrated maps of common molecular and atomic gases are presented in Figure 5.15

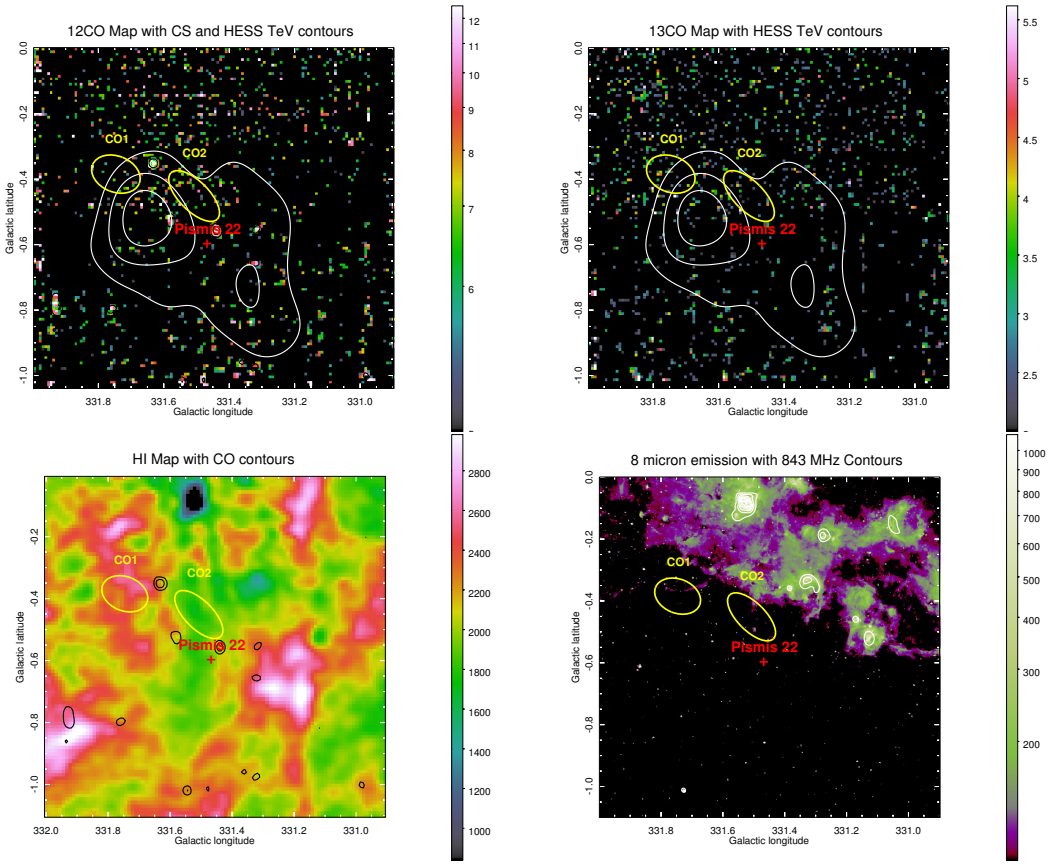

Figure 5.12: The area surrounding the cluster Pismis 22 roughly centered on HESS J1614-518. The top left panel shows the ^{12}CO map with the RoI CO (1–0) regions marked in white. The potential accelerators are shown in yellow. HESS TeV contours are shown in white and CS (1–0) contours are in black. The top right panel shown the ^{13}CO emission presented the same as the ^{12}CO emission omitting the CS (1–0) contours. The bottom left panel shows the HI emission with the ^{12} CO contours in black along with the RoI CO (1–0) in white and the potential accelerators in yellow. The bottom right image shows the 8 μm Spitzer map with the 843 MHz emission as white contours. Again, RoI are shown in white and potential accelerators are marked in yellow. The CO and HI data was integrated between -9 km/s and -19 km/s.

along with 8 μm infrared emission and 843 GHz contours. The data has been integrated over a 10 km/s range from -96 km/s to -106 km/s which incorporates the pulsar's kinematic velocity of -101 km/s and distance of 6.1 kpc. A column density map of the protons in the region was also made using the Mopra ^{12}CO and HI data. This is presented in Figure 5.16.

It is evident from the morphology of the gas that there is only very weak HI emission near the pulsar. There is no molecular gas close to the pulsar. There is some molecular gas found near the northern peak of the gamma-ray source. This is associated with the

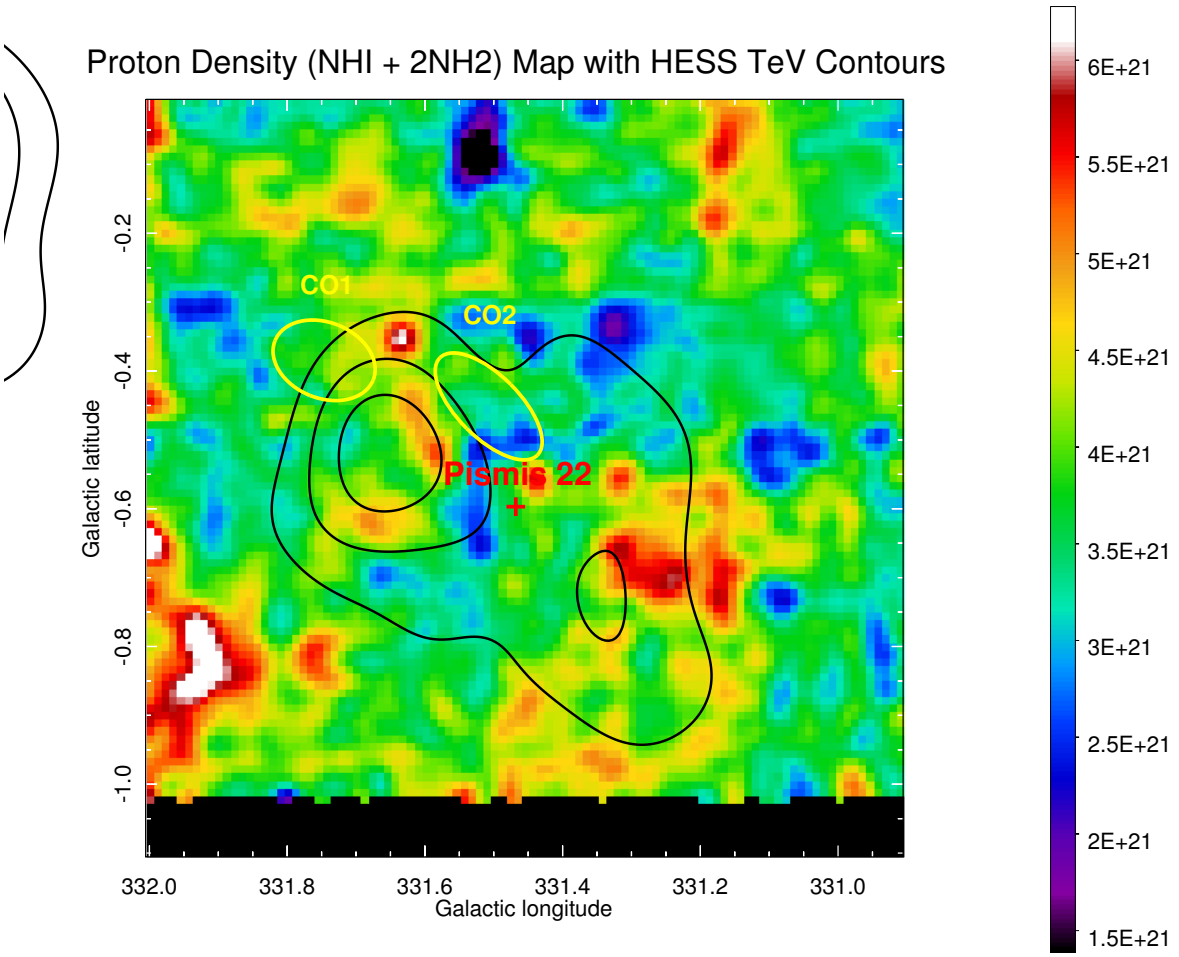

Figure 5.13: The column density map of hydrogen gas towards Pismis 22 and HESS J1614-518. The CO (1–0) RoI are marked as yellow ellipses while the HESS TeV contours are black. Pismis 22 is labelled in red. The map was made from the sum of the HI column density and twice the H_2 column density calculated from CO (1–0).

various star forming regions which are prevalent at this velocity due to the the presence of a spiral arm. Hence this gas might not be related to the gamma-ray emission but further discussion is left to Chapter 6. Similarly there is no thermal or radio continuum emission close to the pulsar. The column density, mass and density of the identified regions are presented in table 5.2.

Due to the lack of interstellar gas near the pulsar coupled with its low spin down power and location, it is thought that PSRJ1613-5211 does not accelerate particles which could then go on to create the observed gamma-ray emission.

WR 73-1

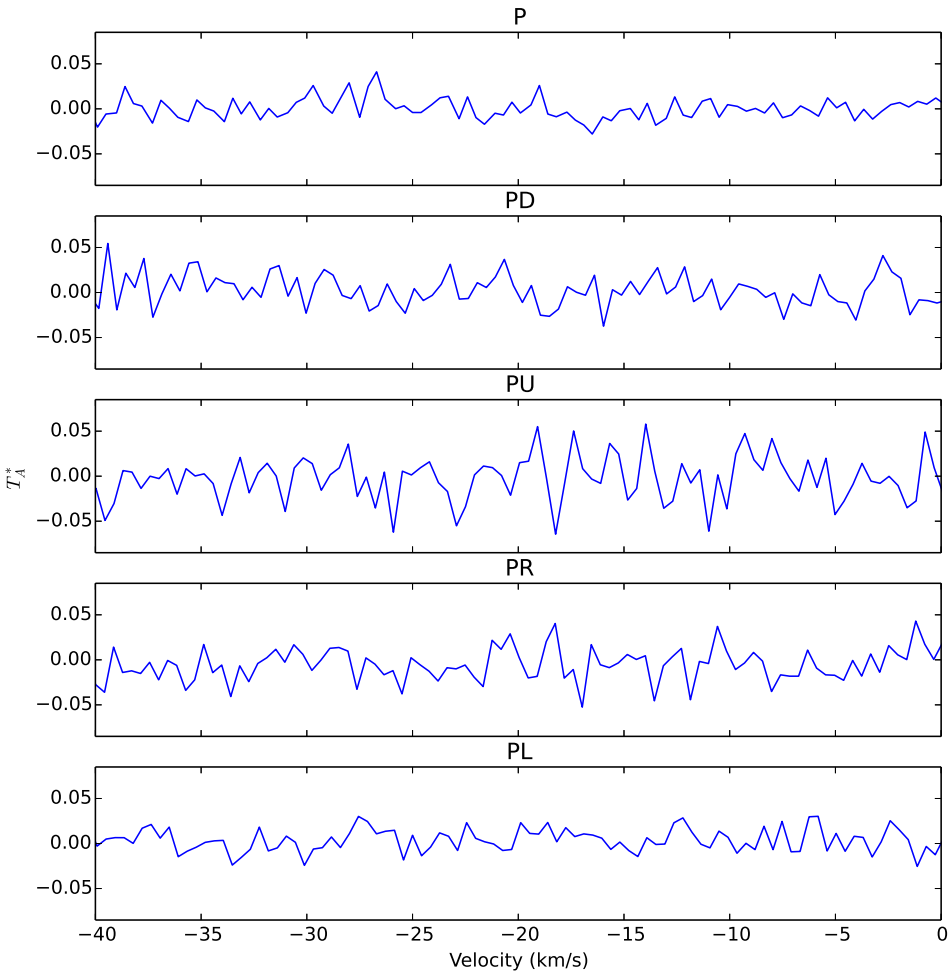

Figure 5.14: NH_3 (1–1) spectra from deep pointings towards Pismis 22. Refer to 3.1 for details of the pointings.

It has been suggested that WR stars should be able to accelerate particles through the shock that forms from their strong stellar winds. However, such a situation is yet to be observed but some non-thermal X-ray and gamma-ray emission is seen towards stellar clusters containing WR binaries such as Westerlund 2 (Carraro et al., 2013). There are two WR stars which are located close to the gamma-ray source HESS J1614-518. One is WR 73-1 which is located at a distance of 10.9 kpc. This is related to a kinematic velocity of −63 km/s where the star would be located at the far distance. WR 73-1 is spatially

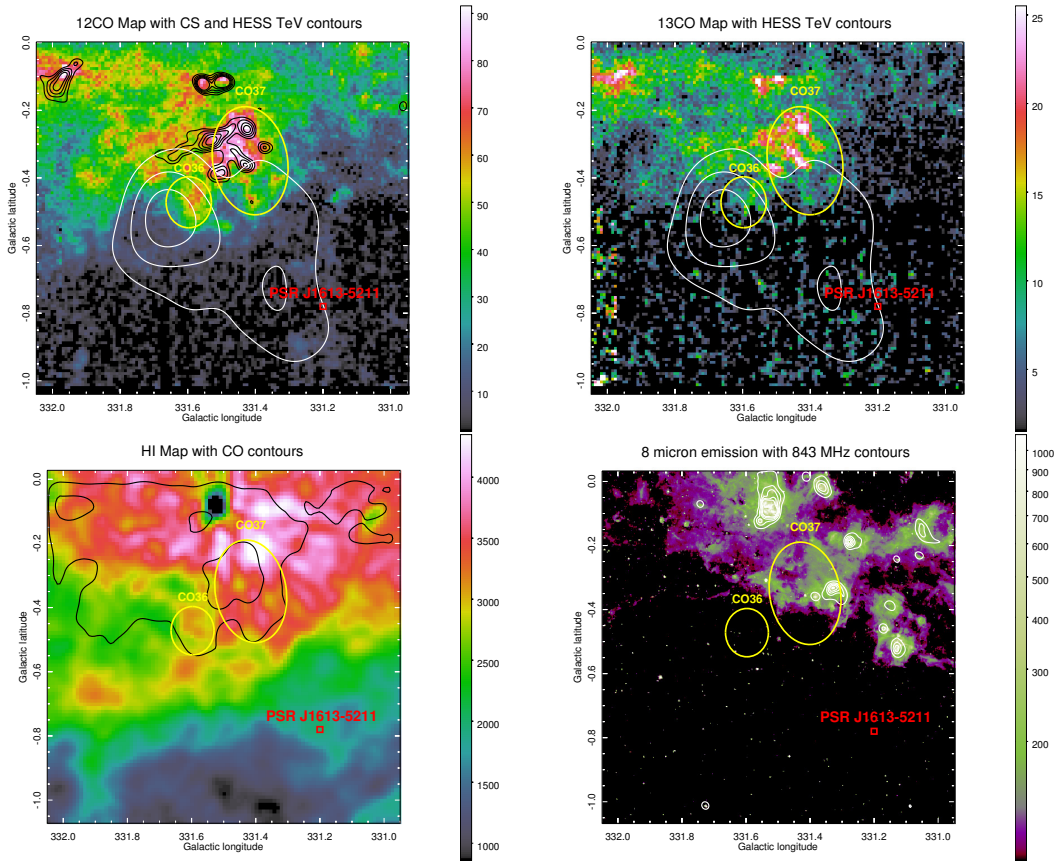

Figure 5.15: The area surrounding the pulsar PSR J1613-5211 roughly centered on HESS J1614-518. The top left panel shows the ^{12}CO map with the RoI CO (1–0) regions marked in white. The potential accelerators are shown in yellow. HESS TeV contours are shown in white and CS (1–0) contours are in black. The top right panel shows the ^{13}CO emission presented the same as the ^{12}CO emission omitting the CS (1–0) contours. The bottom left panel shows the HI emission with the ^{12} CO contours in black along with the RoI CO (1–0) in white and the potential accelerators in yellow. The bottom right image shows the 8 μm Spitzer map with the 843 MHz emission as white contours. Again, RoI are shown in white and potential accelerators are marked in yellow. The CO and HI data was integrated between -96 km/s and -106 km/s.

located outside of the gamma-ray contours near the northern peak of the gamma-ray emission.

The ISM data available towards HESS J1614-518 was integrated over a 10 km/s velocity interval from -59 km/s to -69 km/s which covers the star's distance of -63 km/s. The data is presented in Figure 5.17. A column density map of the protons in the region was also made using the Mopra ^{12}CO and HI data. This is presented in Figure 5.18.

There is some molecular emission located near the star which is encompassed by CO24 including ^{13}CO and CS. There is also diffuse HI present although a continuum source

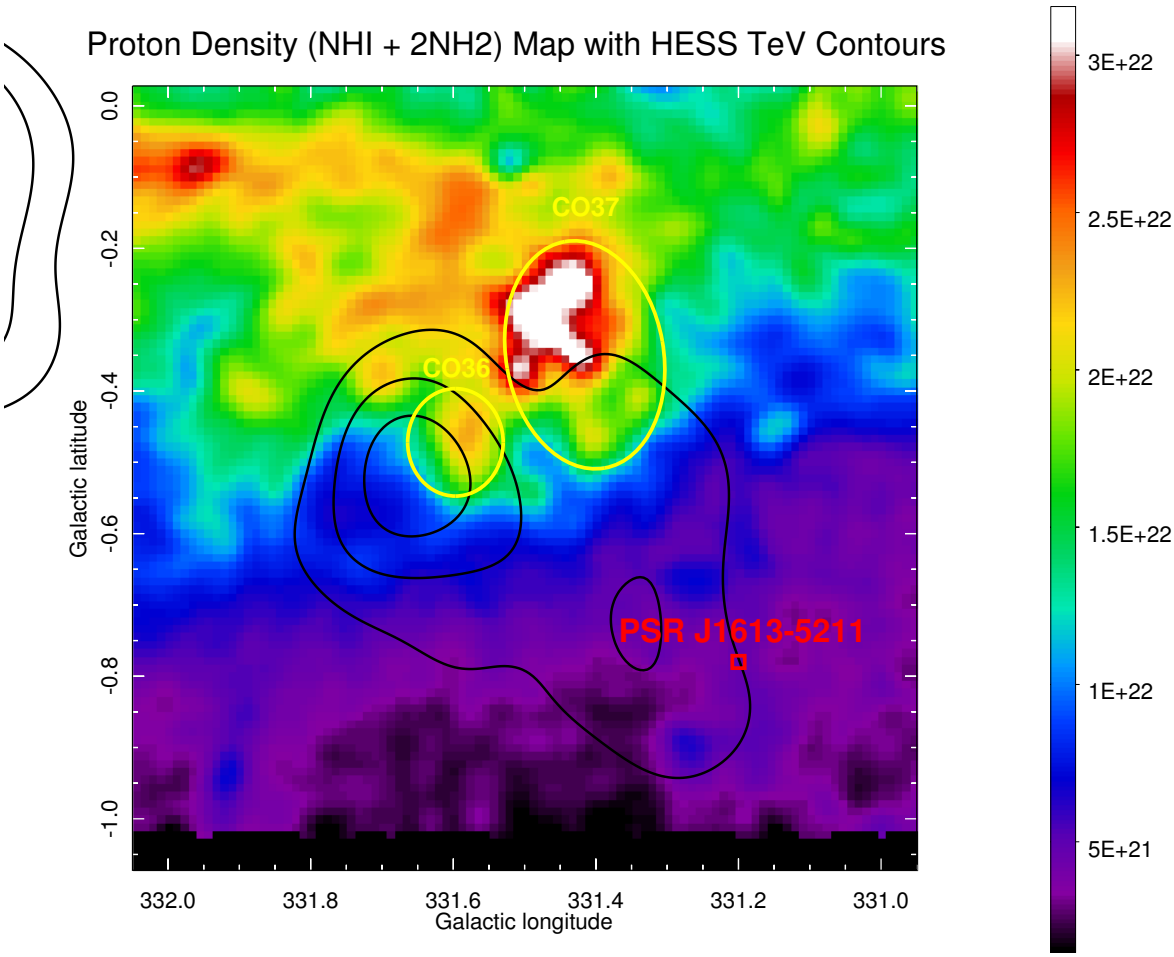

Figure 5.16: The column density map of hydrogen gas towards PSR J1613-5211 and HESS J1614-518. The CO (1–0) RoI are marked as yellow ellipses while the HESS TeV contours are black. PSR J1613-5211 is labelled in red. The map was made from the sum of the HI column density and twice the H_2 column density calculated from CO (1–0).

has contaminated the data as can be seen by the radial streaks. Information about the identified regions is presented in table 5.2.

Since WR stars are born from massive O and occasionally B type stars a shell could be visible in HI resulting from the stellar winds blowing out a bubble. However, there is no bubble visible within this velocity range centred on the WR star although this again could be due to the interference from the continuum source and the large distance to the star.

If WR 73-1 was accelerating protons across a shock from its stellar wind, there should be some gas coincident with the gamma-ray peaks with which the CRs could collide. However, no such feature is seen. Indeed, there are very dense molecular clouds which are

located above the gamma-ray source which if it is assumed that the particles can travel that distance, they should also be bright in gamma-rays if the situation is hadronic. Thus is is unlikely that there is an association between WR 73-1 and the gamma-ray source.

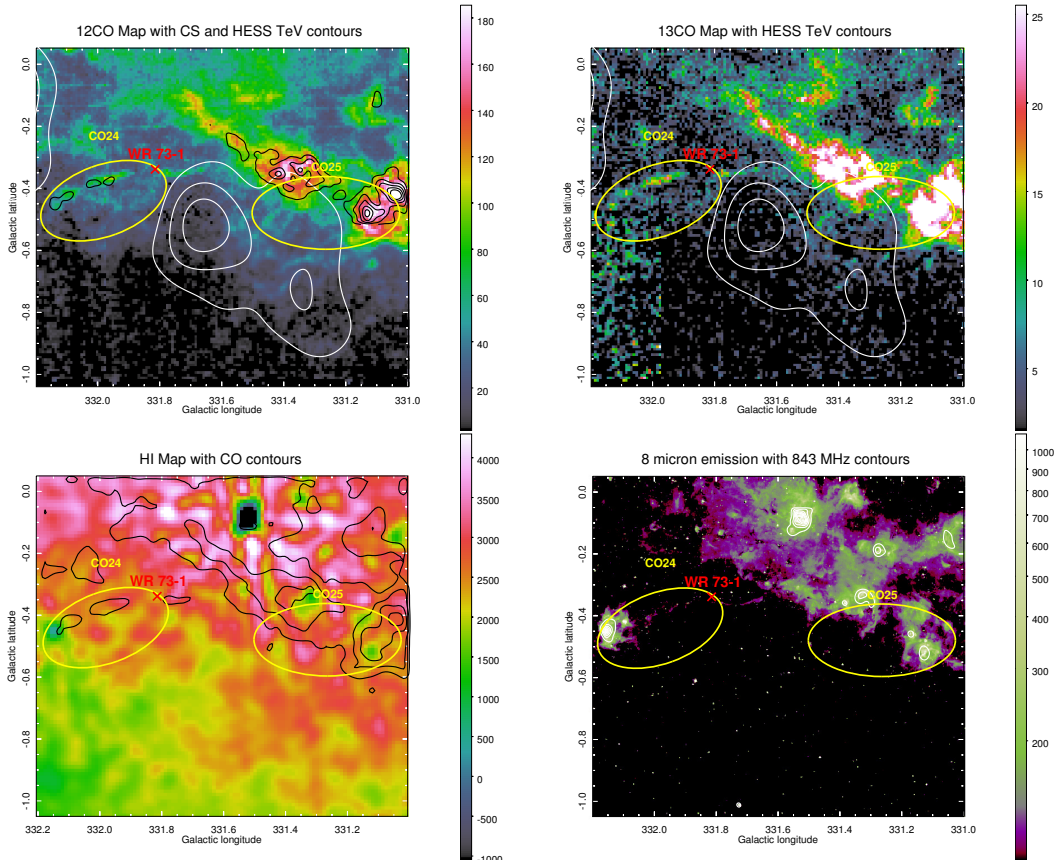

Figure 5.17: The area surrounding the WR star WR 73-1 roughly centered on HESS J1614-518. The top left panel shows the ^{12}CO map with the RoI CO (1–0) regions marked in white. The potential accelerators are shown in yellow. HESS TeV contours are shown in white and CS (1–0) contours are in black. The top right panel shows the ^{13}CO emission presented the same as the ^{12}CO emission omitting the CS (1–0) contours. The bottom left panel shows the HI emission with the ^{12} CO contours in black along with the RoI CO (1–0) in white and the potential accelerators in yellow. The bottom right image shows the 8 μm Spitzer map with the 843 MHz emission as white contours. Again, RoI are shown in white and potential accelerators are marked in yellow. The CO and HI data was integrated between -59 km/s and -69 km/s.

WR 74

WR 74 is another WR star located next to HESS J1614-518. It is located at a distance of 2.6 kpc which corresponds to a kinematic velocity of -35 km/s. The ISM data

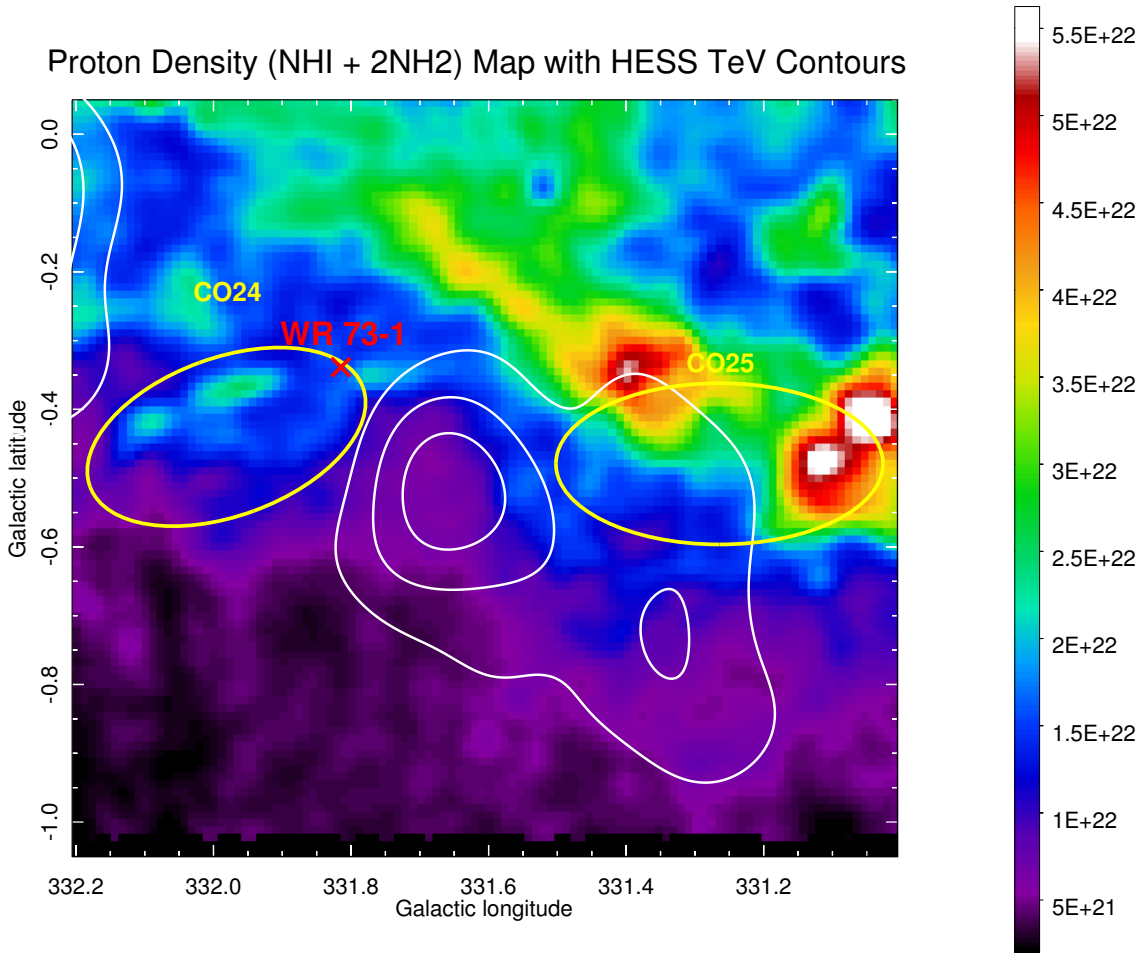

Figure 5.18: The column density map of hydrogen gas towards WR 73-1 and HESS J1614-518. The CO (1–0) RoI are marked as yellow ellipses while the HESS TeV contours are black. WR 73-1 is labelled in red. The map was made from the sum of the HI column density and twice the H_2 column density calculated from CO (1–0).

was integrated over this range and is presented in Figure 5.19 along with the infrared and 843 GHz emission. A column density map of the protons in the region was also made using the Mopra ^{12}CO and HI data. This is presented in Figure 5.20.

Unlike WR 73-1, there is some molecular gas which overlaps the gamma-ray source which corresponds well to CO11. This is diffuse gas since there is no CS and very little ^{13}CO emission towards that region. There is a lot of diffuse HI emission throughout the area which contains a dense concentration to the left of the WR star, away from the gamma-ray source. Additionally, there seems to be what could be a faint shell surrounding the star in the HI emission. The column density, mass and density of CO11 are presented in table 5.2.

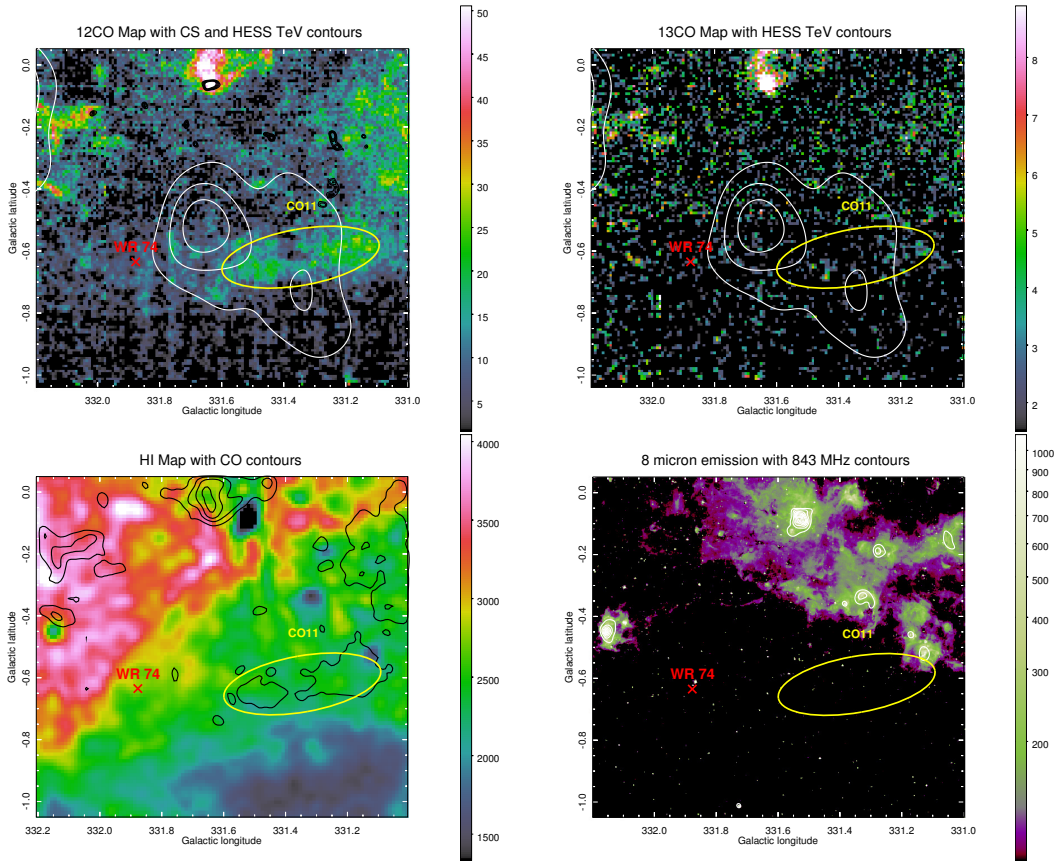

Figure 5.19: The area surrounding the WR star WR 74 roughly centered on HESS J1614-518. The top left panel shows the ^{12}CO map with the RoI CO (1–0) regions marked in white. The potential accelerators are shown in yellow. HESS TeV contours are shown in white and CS (1–0) contours are in black. The top right panel shows the ^{13}CO emission presented the same as the ^{12}CO emission omitting the CS (1–0) contours. The bottom left panel shows the HI emission with the ^{12} CO contours in black along with the RoI CO (1–0) in white and the potential accelerators in yellow. The bottom right image shows the 8 μm Spitzer map with the 843 MHz emission as white contours. Again, RoI are shown in white and potential accelerators are marked in yellow. The CO and HI data was integrated between -30 km/s and -40 km/s.

However, as stated previously, if protons are being accelerated by WR 74 then it would be expected that some gas should coincide with the peaks of the gamma-ray emission. Again this is not the case with most of the emission skirting the peaks. Thus, morphologically it is unlikely that WR 74 is the cause of the gamma-ray emission from HESS J1614-518.

CO RoI Parameters

The near distance, column density, mass and particle density of the CO RoI near identified

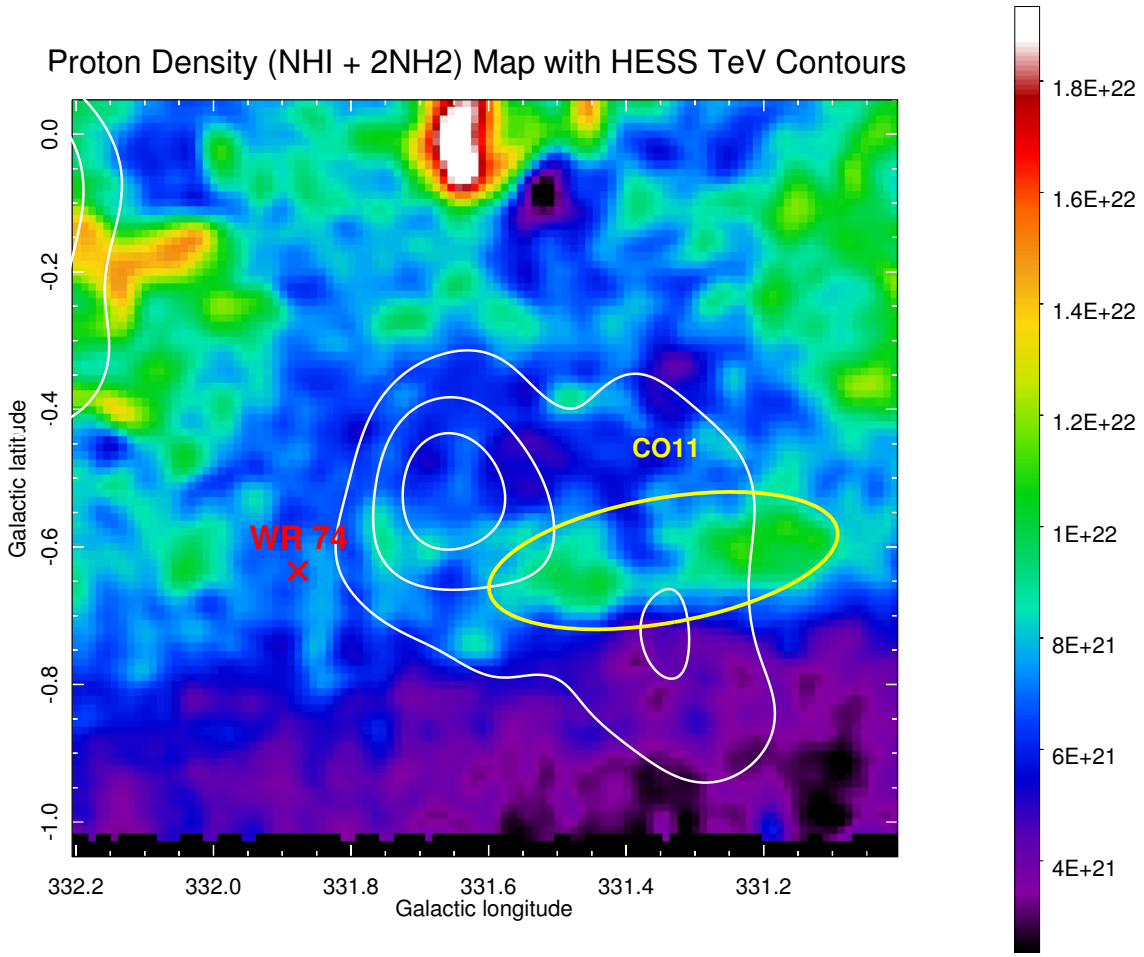

Figure 5.20: The column density map of hydrogen gas towards WR 74 and HESS J1614-518. The CO (1–0) RoI are marked as yellow ellipses while the HESS TeV contours are black. WR 74 is labelled in red. The map was made from the sum of the HI column density and twice the H_2 column density calculated from CO (1–0).

Region	Near d (kpc)	N_{H_2} $\times 10^{21}$	M ($\times 10^4 M_\odot$)	$n(H_2)$ (cm^{-3})
CO1	0.3	2.9	0.002	7258
CO2	0.4	2.7	0.004	6052
CO11	3.0	18.6	7.4	3015
CO24	4.5	7.1	6.4	614
CO25	4.3	11.6	10.8	1035
CO36	6.0	8.4	2.7	929
CO37	6.3	4.1	5.4	262

Table 5.2: Gas Parameters of CO RoI identified near HESS J1614-518. The column density, N_{H_2}, is in units of cm^{-2}. Errors are listed in the main parameter tables 4.7 and 4.8.

potential particle accelerators are shown in table 5.2.

5.3 Summary

This chapter has compared the identified CO RoI and the potential accelerators of CR particles in order to determine which regions need to be investigated further. Of the original 38 CO RoI, nine were associated with potential accelerators towards HESS J1616-508 whilst seven were associated with the potential accelerators towards HESS J1614-518. Morphologically, the WR stars and PSR J1613-5211 were unlikely to be the cause of the gamma-ray source HESS J1614-518 due to the paucity of gas in that region. Pismis 22 remains the most likely counterpart after the morphological study, despite the lack of dense gas tracers such as CS and NH_3.

The pulsar PSR J1614-5048 and the three SNRs; Kes 32, RCW 103 and G332.0+0.2 are all unlikely to be the cause of the gamma-ray emission based on morphological analysis. Note that this has assumed that the SNRs are located at their published distance and not the distance of the coincident HI voids that were identified by the current study. Future research should focus on determining the distances to the SNRs in order to completely eliminated them from being associated with the gamma-ray emission. The study did reveal that the most likely candidate for the production of the gamma-ray emission, based on the morphology of the gas, was the pulsar PSR J1617-5055.

Chapter 6

Modelling the Cosmic Ray Induced Gamma-ray Emissions of the HESS TeV Sources

Using the densities of the interstellar gas calculated in Chapter 4, we will now investigate the possibility that the two TeV gamma-ray sources are a result of accelerated CRs. Here we will derive the CR energy budget required to illuminate the overlapping ISM regions at the level seen by HESS. Then, assuming that nearby SNRs are CR accelerators, the available CR energy budget can be calculated. We assume that the available energy budget at the accelerator is 10^{50} ergs which is typical of a SNR. This assumption was made since we are particularly interested in the hadronic processes which could produce gamma-rays. This energy budget could be an order of magnitude higher if the accelerator is a combination of many accelerators such as several SNRs and high-mass stars as might be expected for a massive stellar cluster. If the energy output of CRs is of the order of 10^{50} ergs then it is plausible that the emission could be produced through hadronic interactions. This study does not focus on leptonic interactions since modelling also requires knowledge of the magnetic field and the interactions are more complex. This is left for future work.

6.1 Modelling a gamma-ray spectrum

The gamma-ray spectrum can be modelled through understanding the interactions of CRs with ISM clouds. This method requires an injected CR spectrum to be assumed by a power law with a maximum energy of E_{max}, a spectral index of α and an exponent $\beta = 1.0$. From Chapter 2, it is known that the index of the power law of a CR spectrum will be approximately equal to the spectral index of the gamma-ray spectrum. The maximum CR energy and the spectral index directly influence the shape of the gamma-ray spectrum. The normalisation can be adjusted by the parameter A where the full parametrisation of the CR spectrum is shown in Equation 6.1:

$$J_P(E_P) = AE_p^{-\alpha} \exp\left[-\left(\frac{E_p}{E_{max}}\right)^{\beta}\right] \tag{6.1}$$

The parameter A can then be found by solving the following equation:

$$\int_{1\text{TeV}}^{\infty} E_p J_p(E_p)\, dE_p = U \text{ erg cm}^{-3} \tag{6.2}$$

where U is the energy density of CRs. Numerical solutions generated by (Kelner et al., 2006) have been employed here for the energy spectrum of gamma-rays and leptons for the interaction of the CRs with the ISM. The number of gamma-ray photons in the energy interval of $(x, x + dx)$ where $x = E_\gamma/E_p$ for a proton of energy E_p per collision is given by:

$$\begin{aligned} F_\gamma(x, E_p) =& B_\gamma \frac{\ln(x)}{x}\left(\frac{1 - x^{\beta_\gamma}}{1 + k_\gamma x^{\beta_\gamma}(1 - x^{\beta_\gamma})}\right)^4 \\ &\times \left[\frac{1}{\ln(x)} - \frac{4\beta_\gamma x^{\beta_\gamma}}{1 - x^{\beta_\gamma}} - \frac{4k_\gamma \beta_\gamma x^{\beta_\gamma}(1 - 2x^{\beta_\gamma}}{1 + k_\gamma x^{\beta_\gamma}(1 - x^{\beta_\gamma}}\right] \end{aligned} \tag{6.3}$$

Kelner et al. (2006) found that the best fit for CRs with energies between 0.1 TeV and 10^5 TeV are given by:

$$B_\gamma = 1.30 + 0.14L + 0.011L^2 \tag{6.4}$$

$$\beta_\gamma = \frac{1}{1.79 + 0.11L + 0.008L^2} \tag{6.5}$$

$$k_\gamma = \frac{1}{0.901 + 0.049L + 0.014L^2} \tag{6.6}$$

where $L = \ln(E_P/1 \text{ TeV})$.

The production rate of gamma-ray photons in the energy range $(E_\gamma, E_\gamma + dE_\gamma)$ was then calculated using Equation 6.7:

$$\Phi_\gamma(E_\gamma) = cn_H \int_{E_\gamma}^{\infty} \sigma_{inel}(E_p) J_p(E_p) F_\gamma(x, E_p) \frac{dE_p}{E_p} \text{ TeV}^{-1} \text{ cm}^{-3} \text{ s}^{-1} \tag{6.7}$$

where c is the speed of light, n_H is the density of ISM hydrogen and σ_{inel} is the inelastic cross-section for CR-ISM collisions given by Equation 6.8:

$$\sigma_{inel}(E_p) = 34.3 + 1.88L + 0.25L^2 \text{ mb} \tag{6.8}$$

The flux of gamma-rays can then be calculated by multiplying by the volume of the region to obtain the total number of gamma-rays produced per energy interval per second and then dividing by the surface area of a sphere with the radius d, equal to the distance between the cloud and the Sun. That is:

$$\mathscr{F}_\gamma(E_\gamma) = \Phi_\gamma(E_\gamma) \left(\frac{ab^2}{3d^2}\right) \text{ photons cm}^{-2} \text{ s}^{-1} \tag{6.9}$$

where a and b are the semi-major and semi-minor axes of the ellipse and $\mathscr{F}$ is the flux of the gamma-rays.

The gamma-ray flux was then calculated for each CO RoI which overlapped the HESS

TeV gamma-ray sources in the velocity range of a potential particle accelerator, resulting in 12 spectral fits. Since the CO RoI which overlapped the HESS TeV contours were smaller than the gamma-ray source, the energy budget was corrected after modelling by the ratio of the area of the CO RoI which overlapped with the area of the HESS TeV outer contour. The errors on the HESS data points were from the publicly available data (Aharonian et al., 2005). The Fermi-LAT upper and lower limits were found using the upper and lower errors on the integrated flux (Acero et al., 2015).

Whilst the HESS J1614-518 fits were able to model both the Fermi-LAT and HESS emission reasonably well, this was not so for HESS J1616-508 where the best fit for the HESS emission results in an excess of emission in the Fermi-LAT energy regime. This would indicate that the TeV and GeV gamma-ray data sets are not well fit by a single power law, suggesting that they could be the result of different particle populations. However, our model was adjusted to primarily fit the HESS data given the focus of our study. Future work would include more sophisticated modelling.

The energy density of the cloud obtained from this modelling assumes that the cloud produces the entire gamma-ray emission. However, we assume that the cloud only produces the gamma-ray emission with which it overlaps. Thus the fractional energy density U_f is given by:

$$U_f = U \frac{A_c}{A_\gamma} \tag{6.10}$$

where A_c is the area of the cloud and A_γ is the area of the gamma-ray source. The gamma-ray source is assumed to be at the same distance of the cloud to the purpose of this calculation.

Furthermore, the energy density at the cloud can be used to find the total CR energy required, W_{CR}. This is given by:

$$W_{CR} = U_f V \tag{6.11}$$

This is the total energy in CRs which the cloud requires in order to be able to produce the gamma-ray emission which overlaps the cloud. This can later be compared to the CR

energy available is a SNR type energy budget is assumed.

6.2 Cosmic Ray Diffusion

The previous section describes the gamma-ray spectrum produced by the cosmic-ray spectrum within the region. However, in order to determine if a SNR can generate the emission possibly produced by a region is is necessary to consider particle propagation from the SNR to the cloud. Thus, a simple estimate using diffusion is made.

The distance travelled by a particle diffusing in three dimensions is given by:

$$d = \sqrt{6Dt} \tag{6.12}$$

where t is the amount of time the particle has been travelling and D is the diffusion coefficient. The maximum time that a CR from a SNR could have spent diffusing to the region is given by the age of the SNR. The diffusion coefficient can be calculated using Equation 6.13 (Gabici et al., 2007):

$$D(E_P, B) = \chi D_0 \left(\frac{E_{max}/GeV}{B/3\mu G} \right)^{0.5} \text{ cm}^2 \text{ s}^{-1} \tag{6.13}$$

where $D_0 = 3 \times 10^{27}$ cm^2 s^{-1}, B is the magnetic field and χ is a diffusion suppression factor given by:

$$\chi = \begin{cases} < 1 & \text{in molecular core,} \\ 1 & \text{outside} \end{cases} \tag{6.14}$$

The CRs are assumed to travel through the diffuse ISM on their way to our RoI, allowing χ to be approximated to 1. Although there are regions of dense gas as evidenced by the presence of CS (1–0) emission, the CRs did not generally have to traverse this gas to arrive at the CO RoI. Additionally, this condition provided an upper limit on the diffusion coefficient. Since the particles are travelling through the diffuse ISM, the magnetic field is assumed to be approximately equal to that of the galactic magnetic field, $B \approx 6$ μG. This

assumption was again made with the aim of calculating the upper limit to the diffusion coefficient. The maximum energy of a proton is given by the cut-off energy E_{max} defined in the previous section. Therefore, it is possible to approximate an upper limit on the diffusion coefficient. This can then be used in Equation 6.12 to determine the maximum distance that the particles can travel for a SNR. Results are discussed in sections 6.4 and 6.5.

6.3 CR energy budget

Another aspect which can be used to test if a potential accelerator is capable of producing the emission is to find the total energy required to generate the gamma-ray emission. An average SNR is expected to output CRs with a total energy of 10^{50} ergs, see for example the review by Dermer and Powale (2013). If our ISM regions require significantly more energy than that, then the SNR is unlikely to power the gamma-ray emission.
If our ISM RoI of radius R_c is at a distance d from the SNR, we can expect a fraction W_E of CRs to reach the RoI as shown in Equation 6.15:

$$W_E = \frac{\pi R_c^2}{4\pi d^2} \times 10^{50} \quad \text{ergs} \tag{6.15}$$

The radius of the region is approximated to be the average of the semi-major and semi-minor axes of the ellipse which defines the RoIs. The distance from the SNR to the cloud is taken from the center of the SNR to the center of the cloud. Thus, if the fractional energy available is approximately equal to the energy required then the SNR could produce the gamma-ray emission from the cloud. We can see this by directly comparing W_{CR} calculated from modelling the gamma-ray flux with the potentially available CR energy, W_E. We now apply this aspect and those from 6.1 and 6.2 to the identified potential CR accelerators towards the two HESS TeV gamma-ray sources.

6.4 HESS J1616-508

The HESS TeV gamma-ray source HESS J1616-508 has five potential particle accelerators including the three SNR G332.0+0.2, RCW 103 and Kes 32 and the two pulsars PSR J1617-5055 and PSR J1614-5048. Each potential accelerator has at least one CO RoI within their kinematic velocity range. The energy spectrum for each region is shown in Figure 6.1. The fit to HESS J1616-508 was done using a cut-off energy of ≈100 TeV. The results from the numerical fitting are summarised for each CO RoI in table 6.1.

RoI	$U \times 10^{-12}$	$U_f \times 10^{-13}$	$W_{CR} \times 10^{46}$	Potential Accelerators
CO26	4.5	26	140	Kes 32
CO27	9.6	7.3	9.0	Kes 32
CO29	5.2	10	32	PSR J1617-5055, RCW 103
CO31	38	31	32	PSR J1617-5055, RCW 103, G332.0+0.2
CO32	42	6.6	3.3	PSR J1617-5055, RCW 103, G332.0+0.2
CO33	30	40	41	PSR J1617-5055, RCW 103, G332.0+0.2
CO34	130	66	17	PSR J1617-5055, RCW 103, G332.0+0.2, PSR J1614-5048

Table 6.1: The energy density required by the RoI if they are to produce the entire gamma-ray flux is given by U in ergs cm^{-3}. The energy density of CR required by the RoI if they are to only produce the gamma-ray emission with which they overlap is given by the U_f, also in units of ergs cm^{-3}, which is inferred by the Kelner modelling. The total energy in CR required at the cloud W_{CR} is in units of ergs. Each RoI's associated potential CR accelerators are also listed.

The energy budget required at the cloud could then be calculated. The fractional energy density U_f was converted into the total energy required, W_{CR}, through the multiplication of the volume of the RoI. The total CR energy requirement, W_{CR} at each RoI surrounding HESS J1616-508 is again shown in table 6.1. It is clear that the energy required at each RoI is significantly less than the CR energy budget of 10^{50} ergs from a typical SNR. Thus, it is possible that all of these clouds could be involved in the production of gamma-rays from hadronic interactions between CRs and the ISM, provided that the clouds interact with a sufficient number of CRs.

The next step was to find the diffusion radius of each potential CR accelerator. Since the cut-off energy found to fit the spectrum of the HESS and Fermi-LAT data is $E_{max} = 100$ TeV, this energy can be used in the equation for the diffusion coefficient such that $D = 7\times10^{28}$ cm^2 s^{-1}. The diffusion radius for each of the potential accelerators is given in table 6.2. The distances from the centres of the five potential accelerators to the center of each

Name	Distance (kpc)	Age (kyr)	Diffusion Radius (pc)
G332.0+0.2	7.4	10	365
RCW 103	6.7	2	163
Kes 32	5.5	3	200
PSR J1617-5055	6.5	8.1	329
PSR J1614-5048	7.2	7.4	314

Table 6.2: The diffusion radii of the CRs from potential accelerator surrounding HESS J1616-508

RoI were then calculated. The results are shown in appendix C. Assuming a maximum energy of 100 TeV, a minimum magnetic field of 6 μG and a diffusion suppression factor of $\chi = 1$, the maximum diffusion radii of CRs from potential accelerators are all an order of magnitude smaller than the distances to the clouds. Thus, while the required CR energy budget, W_{CR} is suitable for gamma-ray production, the CRs probably would not yet have reached them from our considered accelerators. This suggests that the known SNRs are not associated with HESS J1616-508.

6.5 HESS J1614-518

The 40 Myr old stellar cluster Pismis 22 (Piatti et al., 2000) and the WR stars WR73-1 and WR74 are potentially accelerators of cosmic-rays which may produce the gamma-ray spectrum of HESS J1614-518. Additionally, the pulsar PSR J1613-5211 could accelerate electrons which could produce gamma-rays or indicate the presence of a yet undetected SNR. The energy spectrum for each of the regions is shown in Figure 6.2. It was found that all regions surrounding HESS J1614-518 were best fit with a cut-off energy of $\approx$15 TeV. The results from the numerical fitting are summarised for each CO RoI in table 6.3.

RoI	$U \times 10^{-12}$	$U_f \times 10^{-13}$	$W_{CR} \times 10^{43}$	Associated Accelerators
CO1	130	34	1.3	Pismis 22
CO2	140	75	6.4	Pismis 22
CO11	14	30	8700	WR 74
CO25	4.8	8.6	12000	WR 73-1
CO37	21	17	41000	PSR J1613-5211

Table 6.3: The energy density required by the RoI if they are to produce the entire gamma-ray flux is given by U in ergs cm^{-3}. The energy density of CR required by the RoI if they are to only produce the gamma-ray emission with which they overlap is given by the U_f, also in units of ergs cm^{-3} which was inferred from the Kelner modelling. The total energy in CR required by the cloud W_{CR} is in units of ergs. Each RoI's associated potential CR accelerators are also listed.

The energy budget required at the cloud could then be calculated. The fractional energy density U_f was converted into the total energy required, W_{CR}, through the multiplication of the volume of the RoI. The total CR energy requirement, W_{CR} at each RoI surrounding HESS J1614-518 is again shown in table 6.3.

All of the RoI identified overlapping HESS J1614-508 had a required energy budget that is less than the typical CR energy budget of a SNR which is 10^{50} ergs. Thus, each cloud could be involved in the production of gamma-rays from interactions between the clouds and CRs.

We then calculate the distance that CRs from each potential accelerator could have travelled. The cut-off energy found to fit a spectrum to the HESS and Fermi data is given by $E_{max} = 15$ TeV. Thus the upper limit of the diffusion coefficient, $D = 3 \times 10^{29}$ cm^{-2}s^{-1} was calculated. This also assumes a diffusion suppression factor $\chi = 1$ and a magnetic field of $B = 6$ μG. The diffusion radii for the three potential accelerators are shown in table 6.4.

The age of the WR stars is not known, thus an average lifespan of a WR star of 500 kyr was used as an upper limit (Worthey, 2015). The distances to each identified RoI from the location of the three sources are listed in appendix C. There are no ISM RoI within the diffusion radius of WR 73-1, again indicating that the star is not associated with the

Name	Distance (kpc)	Age (kyr)	Diffusion Radius (pc)
Pismis 22	1	40,000	14,000
WR 73-1	10.9	<500	1600
WR 74	2.55	<500	1600
PSR J1613-5211	6.1	377	1400

Table 6.4: The diffusion radii for the three potential CR accelerators near HESS J1614-518.

gamma-ray emission. Similarly, the pulsar PSR J1613-5211 also has no RoI within the diffusion radius. However, CO1 and CO2 are within the diffusion radius of Pismis 22 and CO25 is within the diffusion radius of WR 74.

The RoI within the diffusion radii of the potential accelerators have reasonable required energy budgets assuming that all of the CR energy from a SNR is incident on the cloud. To improve this estimate, we now calculate the energy budget available to the clouds, W_E, assuming that the source has an CR energy budget of 10^{50} ergs. The energy available at each cloud from its associated potential CR accelerator is shown in table 6.5.

RoI	Associated CR Accelerator	d (kpc)	R_c (pc)	W_E ergs
CO1	Pismis 22	0.8	0.4	5.4×40^{42}
CO2	Pismis 22	0.7	0.6	1.6×10^{43}
CO25	WR 74	1.9	13.2	1.2×10^{43}

Table 6.5: The energy budget available for each of the CO RoI within the diffusion radius of the potential CR accelerators.

Potential CRs from Pismis 22 could diffuse to a radius of approximately 14 kpc due to its old age of 40 Myr. The distances from the cluster to the regions presented in appendix C show that protons could have reached all of the selected RoI regardless of whether they are at the near or far distance and indeed, could have traversed several kpc from the cluster.

Each of the RoI required a CR energy budget W_E less than the energy budget available at their distance from the CR accelerator assuming that there is initially 10^{50} ergs available. Thus WR 74 and Pismis 22 are both capable of producing the gamma-ray spectrum at each of the RoI if only hadronic interactions are considered.

6.6 Summary

This chapter used basic modelling methods derived from Kelner et al. (2006) to determine if the potential accelerators were capable of producing gamma-ray emission from accelerated CRs, which were incident on the identified CO RoI. The calculated spectrum for each cloud was fitted to both HESS and Fermi-LAT data. Each identified RoI had a required energy budget that was less than the energy in CRs available from a supernova. However, an estimate of the upper limit of the diffusion radius for each potential accelerator indicated that in many cases, the RoI were too distance from the potential accelerators to be responsible for the gamma-ray emission.

The high energy analysis of HESS J1616-508 found that all three of the known SNRs towards the gamma-ray region were too far from the RoI to cause any emission. Similarly, the diffusion radius for the two pulsars indicate that CRs would not have had time to travel to the emission regions. Thus, it is very unlikely that HESS J1616-508 is the result of high energy CRs. Future research should consider the possibility that the gamma-ray emission is due to leptonic processes.

A similar analysis performed on HESS J1614-518 did not eliminate the possibility of CRs causing the gamma-ray emission. WR 73-1 and PSR J1613-5211 both had diffusion radii which did not encompass any CO RoI. Thus, any accelerated CRs would not yet have interacted with any dense gas to produce gamma-rays. However, WR 74 did contain CO25 within its diffusion radii. Pismis 22's diffusion radii also contained CO1 and CO2. The three RoI also had an require energy budget less than the CR energy provided by a supernova. Thus, it is still possible for the gamma-ray emission to be due to hadronic processes. Future research, using the optical spectra of the stars, is needed to determine if the cluster, Pismis 22 is able to accelerate particles to the energies required to produce the gamma-ray emission.

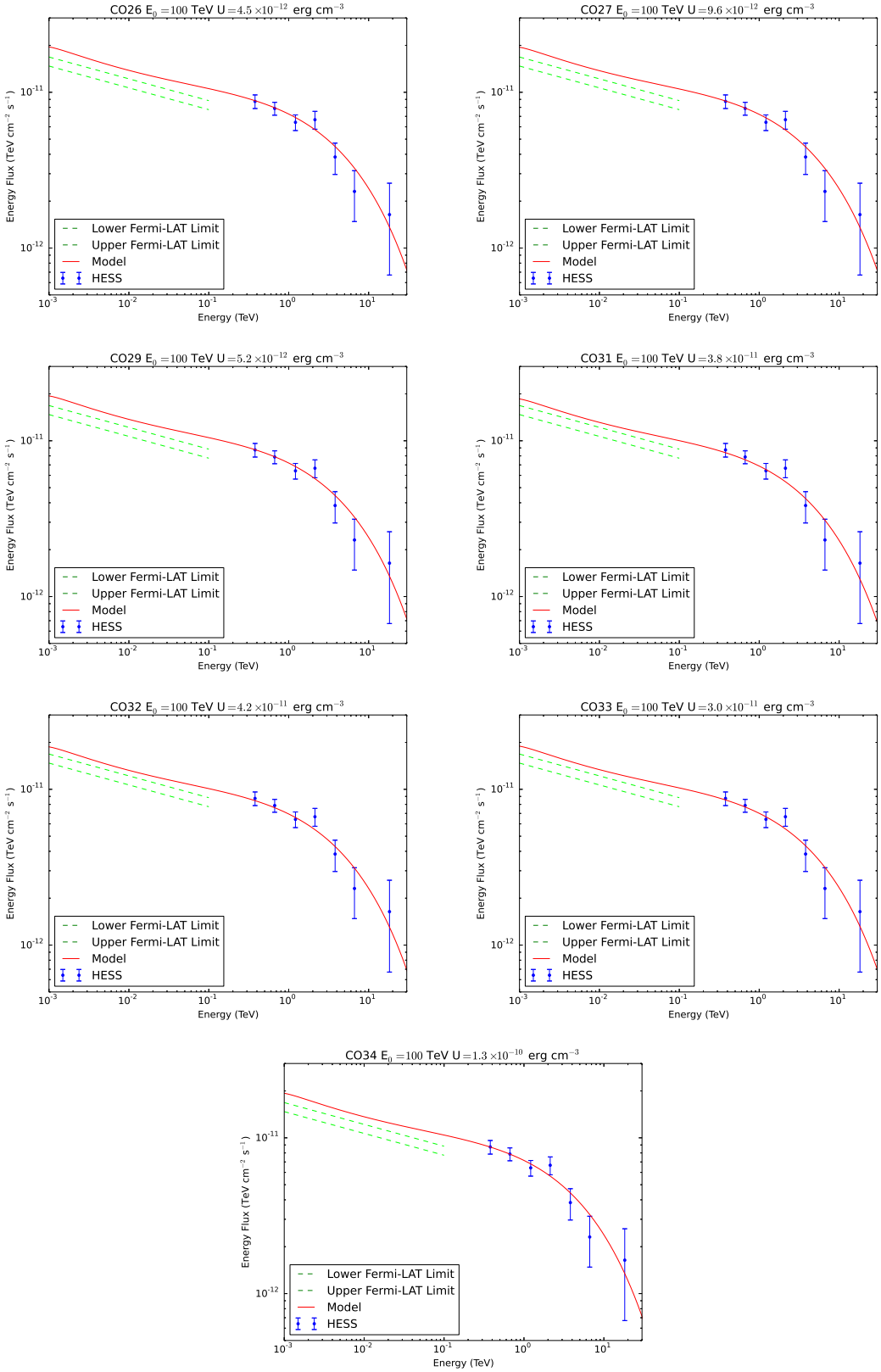

Figure 6.1: Energy flux of gamma-rays from HESS J1616-508. Blue points are the measured HESS spectrum (Aharonian et al., 2005) while the green lines indicate the 1σ boundaries of the Fermi-LAT detection (Acero et al., 2015). The red line shows the modelled spectrum.

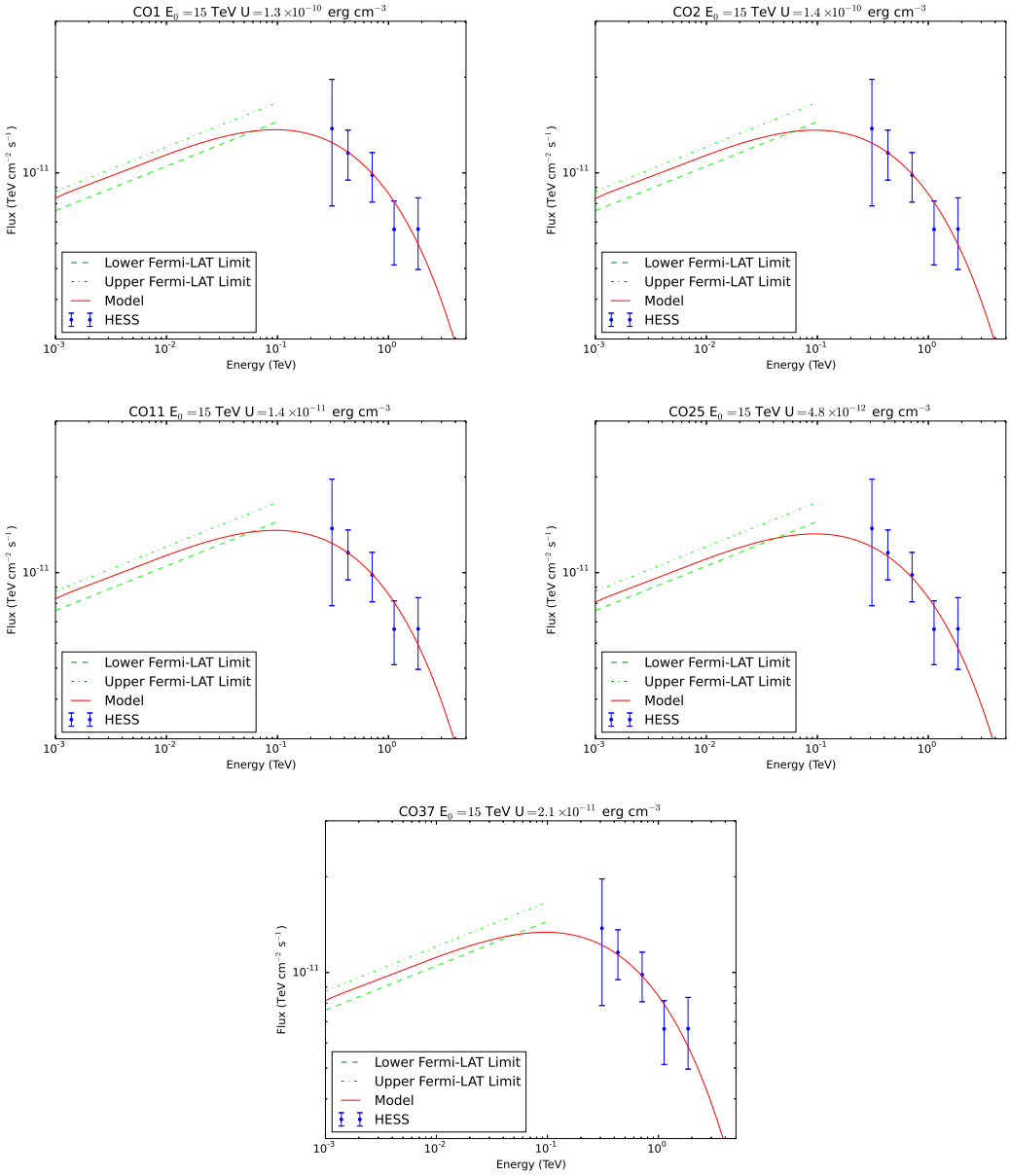

Figure 6.2: Energy flux of gamma-rays from HESS J1614-518. Blue points are the measured HESS spectrum (Aharonian et al., 2005) while the green lines indicate the 1σ boundaries of the Fermi-LAT detection (Acero et al., 2015). The red line shows the modelled spectrum.

Chapter 7

Conclusions and Future Work

The study of high energy gamma-rays by observatories such as HESS is important in attempting to understand the most energetic processes that take place within the Milky Way. The production of gamma-rays through CR-ISM interactions requires detailed knowledge of the gas in the environment of HESS sources. The focus of this study has been to determine if such interactions are capable of producing the gamma-ray spectra that are observed from HESS J1614-518 and HESS J1616-508. This has been done in greater detail than previous studies due to the availability of higher resolution data from the Mopra CO Survey and the MALT-45 Survey. We were able to determine the CR origin of the dark TeV gamma-ray sources.

The source HESS J1614-518 still remains mysterious in nature. However, it is clear that the nearby star WR 73-1 and the pulsar J1613-5211 are not associated with the gamma-ray emission. Simple diffusion calculations revealed that protons would not yet have reached the center of the emission region. Analysis of ISM clouds which overlapped the TeV gamma-ray emission in the velocity range of the stellar cluster Pismis 22 and WR 74 found that there was a sufficient CR energy budget available for interactions between the CRs and the CO RoI CO1, CO2 and CO25 to produce the gamma-rays which overlap the regions. This identified Pismis 22 and WR 74 as potential accelerators of CRs which may generate the observed gamma-ray emission of HESS J1614-518.

The possibility of HESS J1616-508 being associated with any surrounding SNR was excluded. Similarly to the WR stars around HESS J1614-518, the upper limits of all values in the diffusion calculations still indicated that protons accelerated by the SNR would not have travelled further than 400 pc. In all cases, the regions identified were separated by distances greater than 1 kpc from the accelerator. Thus the SNRs Kes 32, RCW 103 and G332.0+0.2 are not associated with the gamma-ray emission. However, this conclusion assumes that the SNRs were located at their published distance. Each SNR has a HI shell coincident with their position but at a different kinematic distance. Since there is a large uncertainty in the published SNR distances, the relation between the SNRs and the HI void warrants further investigation.

This study only modelled simple energy requirements and briefly calculated the diffusion radius of various potential accelerators. Future work would aim to improve the modelling of the propagation of the CRs through the ISM. The excellent spatial resolution of the Mopra CO survey and MALT-45 survey would enable a very detailed CR propagation simulation to be built. Such a simulation could assist in determining the nature of the two HESS TeV gamma-ray sources. In addition, it is also possible to calculate the neutrino flux in the high energy analysis. This could be compared with the neutrino flux detected by instruments such as Icecube to complete the high energy understanding of the sources.

This study has concentrated on the production of gamma-rays through interaction of ISM with CRs. Further study would concentrate on investigating the various interactions of leptonic particles from objects such as PWN and the diffusion of CRs through the ISM. Indeed, further investigation into the association of PSR J1617-5055 with HESS J1616-508 should be done. Additionally, investigation of the many PSRs surrounding HESS J1614-518 could be performed.

There are some future optical observations planned towards Pismis 22 which would allow the individual stellar classifications of each of the stars in the cluster. This would determine if the cluster contains sufficiently powerful stars to generate gamma-rays through

the interactions of stellar winds. Additionally, this could determine if the stars in the cluster have evolved past the main sequence. If a significant proportion of the stars have evolved and there are indications that the cluster contained high mass stars then it is possible that the cluster could contain a number of undetected SNRs or pulsars.

Bibliography

F. Acero, F. Aharonian, A. G. Akhperjanian, et al. Localizing the VHE γ-ray source at the Galactic Centre. *Monthly Notices of the Royal Astronomical Society*, 402:1877–1882, Mar. 2010. doi: 10.1111/j.1365-2966.2009.16014.x.

F. Acero, M. Ackermann, M. Ajello, et al. Constraints on the galactic population of tev pulsar wind nebulae using fermi large area telescope observations. *The Astrophysical Journal*, 773:77–104, June 2013.

F. Acero, M. Ackermann, M. Ajello, et al. Fermi Large Area Telescope Third Source Catalog. *The Astrophysical Journal Supplement Series*, 218:23, June 2015. doi: 10.1088/0067-0049/218/2/23.

F. Aharonian. Very high and ultra-high-energy gamma-rays from giant molecular clouds. *Astrophysics and Space Science*, 180(2):305–320, 1991. ISSN 0004-640X. doi: 10.1007/BF00648185. URL `http://dx.doi.org/10.1007/BF00648185`.

F. Aharonian, A. G. Akhperjanian, K.-M. Aye, et al. A New Population of Very High Energy Gamma-Ray Sources in the Milky Way. *Science*, 307:1938–1942, Mar. 2005. doi: 10.1126/science.1108643.

F. A. Aharonian, L. O. Drury, and H. J. Voelk. GeV/TeV gamma-ray emission from dense molecular clouds overtaken by supernova shells. *Astronomy and Astrophysics*, 285:645–647, May 1994.

R. Aloisio, V. Berezinsky, and P. Blasi. Ultra high energy cosmic rays: implications of

auger data for source spectra and chemical composition. *Journal of Cosmology and Astro-Particle Physics*, 10:020, Oct. 2014. doi: 10.1088/1475-7516/2014/10/020.

A. Bell. The acceleration of cosmic rays in shock fronts. i. *Monthly Notices of the Royal Astronomical Society*, 182:147–156, Jan. 1978.

P. Bhattacharjee. Origin and propagation of extremely high energy cosmic rays. *Physics Reports*, 327:109–247, Mar. 2000. doi: 10.1016/S0370-1573(99)00101-5.

C. Braiding, M. G. Burton, R. Blackwell, et al. The Mopra Southern Galactic Plane CO Survey - Data Release 1. *Publications of the Astronomical Society of Australia*, 32:e020, May 2015. doi: 10.1017/pasa.2015.20.

J. Brand and L. Blitz. The Velocity Field of the Outer Galaxy. *Astronomy and Astrophysics*, 275:67, Aug. 1993.

M. G. Burton, C. Braiding, C. Glueck, et al. The Mopra Southern Galactic Plane CO Survey. *Publications of the Astronomical Society of Australia*, 30:e044, Aug. 2013. doi: 10.1017/pasa.2013.22.

G. Carraro, D. Turner, D. Majaess, and G. Baume. The distance to the young open cluster Westerlund 2. *Astronomy & Astrophysics*, 555:A50, July 2013. doi: 10.1051/0004-6361/201321421.

S. Carrigan, F. Brun, R. C. G. Chaves, et al. Charting the TeV Milky Way: H.E.S.S. Galactic plane survey maps, catalog and source populations. In *Proceedings of the 48th Rencontres de Moriond*, July 2013.

S. Carrigan, F. Brun, R. C. G. Chaves, et al. Charting the tev milky way: H.e.s.s. galactic plane survey maps, catalog and source populations. In *4th Recontres de Moriond on Very High Energy Phenomena in the Universe*, July 2013.

E. Churchwell, B. L. Babler, M. R. Meade, et al. The Spitzer/GLIMPSE Surveys: A New

View of the Milky Way. *Publications of the Astronomical Society of the Pacific*, 121: 213–230, Mar. 2009. doi: 10.1086/597811.

T. M. Dame, D. Hartmann, and P. Thaddeus. The Milky Way in Molecular Clouds: A New Complete CO Survey. *The Astrophysical Journal*, 547:792–813, Feb. 2001. doi: 10.1086/318388.

A. De Luca, R. P. Mignani, S. Zaggia, et al. Deep Infrared Observations of the Puzzling Central X-Ray Source in RCW 103. *The Astrophysical Journal*, 682:1185–1194, Aug. 2008. doi: 10.1086/588600.

C. D. Dermer and G. Powale. Gamma rays from cosmic rays in supernova remnants. *Astronomy & Astrophysics*, 553:A34, May 2013. doi: 10.1051/0004-6361/201220394.

J. M. Dickey and F. J. Lockman. H I in the Galaxy. *Annual review of astronomy and astrophysics*, 28:215–261, 1990. doi: 10.1146/annurev.aa.28.090190.001243.

B. Draine and C. McKee. Theory of interstellar shocks. *Annual Review of Astronomy and Astrophysics*, 31:373–432, 1993. doi: 10.1146/annurev.aa.31.090193.002105.

A. Einstein. On the electrodynamics of moving bodies. *Annalen der Physik*, 17:891, 1905. URL `http://www.fourmilab.ch/etexts/einstein/specrel/specrel.pdf`.

R. Engel, D. Heck, and T. Pierog. Extensive air showers and hadronic interactions at high energy. *Annual Review of Nuclear and Particle Science*, 61:467–489, 2011. doi: 10.1146/annurev.nucl.012809.104544. URL `http://dx.doi.org/10.1146/annurev.nucl.012809.104544`.

E. Fermi. Galactic magnetic fields and the origin of cosmic radiation. *The Astrophysical Journal*, 119:1, Jan. 1954. doi: 10.1086/145789.

M. A. Frerking, R. W. Wilson, R. A. Linke, and P. G. Wannier. Isotopic abundance ratios in interstellar carbon monosulfide. *Astrophysical Journal*, 240:65–73, Aug. 1980. doi: 10.1086/158207.

S. R. Furlanetto, S. P. Oh, and F. H. Briggs. Cosmology at low frequencies: The 21 cm transition and the high-redshift Universe. *Physics Reports*, 433:181–301, Oct. 2006. doi: 10.1016/j.physrep.2006.08.002.

S. Gabici. Gamma Ray Astronomy and the Origin of Galactic Cosmic Rays. In *Proceedings of the XXI European Cosmic Ray Symposium*, Nov. 2008.

S. Gabici, F. A. Aharonian, and P. Blasi. Gamma rays from molecular clouds. *Astrophysics and Space Science*, 309:365–371, June 2007. doi: 10.1007/s10509-007-9427-6.

A. J. Green, L. E. Cram, M. I. Large, and T. Ye. The Molonglo Galactic Plane Survey. I. Overview and Images. *The Astrophysical Journal Supplement Series*, 122:207–219, May 1999. doi: 10.1086/313208.

K. L. I. Gunawardhana, K. P. S. C. Jayaratne, and J. Adassuriya. A method to estimate the cooling time of ultra-relativistic electrons in pulsar wind nebulae. *American Journal of Astronomy and Astrophysics*, 3:63–69, 2015.

M. Haverkorn, B. M. Gaensler, N. M. McClure-Griffiths, J. M. Dickey, and A. J. Green. The Southern Galactic Plane Survey: Polarized Radio Continuum Observations and Analysis. *The Astrophysical Journal Supplement Series*, 167:230–238, Dec. 2006. doi: 10.1086/508467.

A. M. Hillas. The Origin of Ultra-High-Energy Cosmic Rays. *Annual review of astronomy and astrophysics*, 22:425–444, 1984. doi: 10.1146/annurev.aa.22.090184.002233.

J. A. Hinton and W. Hofmann. Teraelectronvolt astronomy. *Annual review of astronomy and astrophysics*, 47:523–565, June 2009.

C. H. Jordan, A. J. Walsh, V. Lowe, et al. MALT-45: a 7 mm survey of the southern Galaxy - I. Techniques and spectral line data. *Monthly Notices of the Royal Astronomical Society*, 448:2344–2361, Apr. 2015. doi: 10.1093/mnras/stv178.

O. Kargaltsev, G. G. Pavlov, and J. A. Wong. Young energetic psr j1617-5055, its underluminous nebula and unidentified tev source hess j1616-508. *The Astrophysical Journal*, 690:891–901, May 2009.

V. M. Kaspi, F. Crawford, R. N. Manchester, et al. The 69 Millisecond Radio Pulsar near the Supernova Remnant RCW 103. *The Astrophysical Journal*, 503:L161–L165, Aug. 1998. doi: 10.1086/311550.

S. R. Kelner, F. A. Aharonian, and V. V. Bugayov. Energy spectra of gamma rays, electrons, and neutrinos produced at proton-proton interactions in the very high energy regime. *Physical Review D*, 74(3):034018, Aug. 2006. doi: 10.1103/PhysRevD.74.034018.

R. Landi, A. D. Rosa, A. J. Dean, et al. Hess j1616-508: likely powered by psr j1617-5055. *Monthly Notices of the Royal Astronomical Society*, 380:926–937, July 2007.

A. Lemiere, R. Terrier, and A. Djannati-Ataï. Multi-resolution analysis of the h.e.s.s. galactic survey sources and search for counterparts in co and hi data. In *Dans Proceedings of the 29th International Cosmic Ray Conference*, pages 105–108, 2005.

R. N. Manchester, G. B. Hobbs, A. Teoh, and M. Hobbs. The Australia Telescope National Facility Pulsar Catalogue. *The Astrophysical Journal*, 129:1993–2006, Apr. 2005. doi: 10.1086/428488.

H. Matsumoto, H. Uchiyama, M. Sawada, et al. Discovery of extended x-ray emission from the unidentified tev source hess j1614-518 using the suzaku satellite. *Publications of the Astronomical Society of Japan*, 60:163–172, Dec. 2007.

N. M. McClure-Griffiths, J. M. Dickey, B. M. Gaensler, et al. The Southern Galactic Plane Survey: H I Observations and Analysis. *The Astrophysical Journal Supplement Series*, 158:178–187, June 2005. doi: 10.1086/430114.

T. Mizukami, H. Kubo, T. Yoshida, et al. Cangaroo-iii observation of tev gamma rays from the unidentified gamma-ray source hess j1614-518. *The Astrophysical Journal*, 740:78–87, July 2011.

A. Mizuno and Y. Fukui. Physical properties of molecular clouds as revealed by NANTEN CO survey: from the galactic center to the galactic warp. In D. Clemens, R. Shah, and T. Brainerd, editors, *Milky Way Surveys: The Structure and Evolution of our Galaxy*, volume 317 of *Astronomical Society of the Pacific Conference Series*, page 59, Dec. 2004.

N. Ouellette, S. Desch, and J. Hester. Interaction of supernova ejecta with nearby protoplanetary disks. *Astrophysical Journal*, 662:1268–1281, June 2007. doi: 10.1086/518102.

M. Z. Pavlovic, A. Dobardzic, B. Vukotic, and D. Urosevic. Updated Radio Sigma-D Relation for Galactic Supernova Remnants. *Serbian Astronomical Journal*, 189:25–40, Dec. 2014. doi: 10.2298/SAJ1489025P.

A. Piatti, J. Claria, and E. Bica. Photometric and integrated spectral study of the young open clusters pismis 22, ngc 6178, ngc 6216 and ruprecht 130. *Astronomy and Astrophysics*, 360:529–538, 2000.

Pierre Auger Collaboration. Correlation of the highest-energy cosmic rays with nearby extragalactic objects. *Science*, 318:938–, Nov. 2007. doi: 10.1126/science.1151124.

Pierre Auger Collaboration. Correlation of the highest-energy cosmic rays with the positions of nearby active galactic nuclei. *Astroparticle Physics*, 29:188–204, Apr. 2008. doi: 10.1016/j.astropartphys.2008.01.002.

R. Protheroe. Honours astrophysics iv lectures. Adelaide University Honours Astrophysics IV Lecture Notes.

J. Quinn, C. W. Akerlof, S. Biller, et al. Detection of Gamma Rays with $E > 300$ GeV from Markarian 501. *Astrophysical Journal Letters*, 456:L83, Jan. 1996. doi: 10.1086/309878.

G. Rowell, D. Horns, Y. Fukui, and Y. Moriguchi. A closer look at the unidentified tev source hess j1614-518. In F. Aharonian, W. Hofmann, and F. Rieger, editors, *American Institute of Physics Conference Series*, volume 1085 of *American Institute of Physics Conference Series*, pages 241–244, 2008. doi: 10.1063/1.3076650.

O. E. H. Rydbeck, A. Sume, A. Hjalmarson, et al. Hyperfine structure of interstellar ammonia in dark clouds. *Astrophysical Journal, Part 2 - Letters to the Editor*, 215: L35–L40, July 1977. doi: 10.1086/182471.

M. Sakai, Y. Yajima, and H. Matsumoto. Nature of the unidentified tev source hess j1614-518, revealed by suzaku and xmm-newton observations. *Publications of the Astronomical Society of Japan*, 63:879–887, Oct. 2011.

C. L. Sarazin. The Energy Spectrum of Primary Cosmic-Ray Electrons in Clusters of Galaxies and Inverse Compton Emission. *The Astrophysical Journal*, 520:529–547, Aug. 1999. doi: 10.1086/307501.

R. Simon, J. M. Jackson, D. P. Clemens, T. M. Bania, and M. H. Heyer. The structure of four molecular cloud complexes in the bu-fcrao milky way galactic ring survey. *The Astrophysical Journal*, 551(2):747, 2001. URL `http://stacks.iop.org/0004-637X/551/i=2/a=747`.

A. W. Strong, I. V. Moskalenko, O. Reimer, S. Digel, and R. Diehl. The distribution of cosmic-ray sources in the Galaxy, γ-rays and the gradient in the CO-to-H_2 relation. *Astronomy and Astrophysics*, 422:L47–L50, July 2004. doi: 10.1051/0004-6361:20040172.

L. Szűcs, S. C. O. Glover, and R. S. Klessen. The ^{12}CO/^{13}CO ratio in turbulent molecular clouds. *Monthly Notices of the Royal Astronomical Society*, 445:4055–4072, Dec. 2014. doi: 10.1093/mnras/stu2013.

The HESS Collaboration. The h.e.s.s. survey of the inner galaxy in very high-energy gamma-rays. *Astrophysical Journal*, 636:777–797, 2006.

The HESS Collaboration. Extending the h.e.s.s. galactic plane survey. *International Cosmic Ray Conference*, 1:2, July 2009.

The HESS Collaboration. Performance of hess-ii in multi-telescope mode with a multivariate analysis. In *AIP Conference Proceedings*, 2012.

J. S. Urquhart, M. G. Hoare, C. R. Purcell, et al. Characterisation of the Mopra Radio Telescope at 16-50GHz. *Publications of the Astronomical Society of Australia*, 27:321–330, Sept. 2010. doi: 10.1071/AS10002.

K. A. van der Hucht. The VIIth catalogue of galactic Wolf-Rayet stars. *New Astronomy Reviews*, 45:135–232, Feb. 2001. doi: 10.1016/S1387-6473(00)00112-3.

J. Vink. Revealing the Obscured Supernova Remnant Kesteven 32 with Chandra. *The Astrophysical Journal*, 604:693–699, Apr. 2004. doi: 10.1086/381930.

G. Worthey. Precision age indicators that exploit chemically peculiar stars. *Astronomy & Astrophysics*, 580:L5, Aug. 2015. doi: 10.1051/0004-6361/201526588.

Appendix A

Derivations

A.1 CR Acceleration Derivation

The force on a charged particle is given by the equation for Lorentz force:

$$\vec{F} = q\vec{\mathscr{E}} + q\vec{v} \times \vec{B} \tag{A.1.1}$$

The electric field is represented by $\vec{\mathscr{E}}$, q is the charge of the particle, $\vec{v}$ is the velocity and $\vec{B}$ is the magnetic field. The change in energy of a charged particle is given by the dot product of the velocity of the particle and the Lorentz force:

$$\frac{dE}{dt} = \vec{v} \cdot \vec{F} = q\vec{v} \cdot \vec{\mathscr{E}} \tag{A.1.2}$$

In many situations in space, there are not enough particles to form a strong electrostatic field due to charge separation since the particle can freely flow to neutralise the field. However, if a plasma is tied to a magnetic field, free movement can be inhibited. In such cases, Faraday's law can be used for a plasma travelling at velocity v_p relative to the laboratory frame:

$$\oint \vec{\mathscr{E}} \cdot d\vec{l} = \oint \vec{v_p} \times \vec{B} \cdot d\vec{l} \tag{A.1.3}$$

Hence, the maximum electric field occurs along the same direction as the magnetic field and when the plasma is travelling perpendicular to both fields. That is:

$$|\vec{\mathscr{E}_{max}}| = v_p|\vec{B}| \tag{A.1.4}$$

The maximum electric field can be substituted back into the equation for the change in energy to obtain the maximum rate of energy change:

$$\frac{dE}{dt}_{max} = q|v||v_p||B| \tag{A.1.5}$$

The upper limit on the change in energy occurs when both the velocity of the particle and the velocity of the plasma approach the speed of light. That situation is the upper limiting case:

$$\frac{dE}{dt}_{max} < qc^2B \tag{A.1.6}$$

The change in energy of any particle then must be some fraction of the maximum change in energy. Thus the acceleration rate parameter, $\xi < 1$ is introduced. Then the change of energy of a particle is given by Equation A.1.7:

$$\frac{dE}{dt}_{max} = \xi Zec^2B \tag{A.1.7}$$

A.2 Fermi's Theory of Acceleration Derivation

The Lorentz factors of the cloud are given by Equations A.2.8 and A.2.9:

$$\beta_c = \frac{V_c}{c} \tag{A.2.8}$$

$$\gamma_c = \frac{1}{\sqrt{1-\beta_c^2}} \tag{A.2.9}$$

Thus the Lorentz transform of the particle's initial conditions to the cloud frame is described by Equation A.2.10:

$$E_1' = \gamma_c E_1(1 - \beta_c \cos\theta_1) \tag{A.2.10}$$

The Lorentz transform of the particle's final conditions in the cloud frame to the laboratory frame is given by:

$$E_2 = \gamma_c E_2'(1 + \beta_c \cos\theta_2') \tag{A.2.11}$$

Then, using the assumption that scattering is collisionless so the particle's energy does not change in the cloud frame, the final conditions of the particle in the cloud frame is given by:

$$E_2' = \gamma_c E_1(1 - \beta_c \cos\theta_1) \tag{A.2.12}$$

Thus the final energy of the particle in the laboratory frame can be written as:

$$E_2 = \gamma_c^2 E_1(1 - \beta_c \cos\theta_1)(1 + \beta_c \cos\theta_2') \tag{A.2.13}$$

$$E_2 = \gamma_c^2 E_1(1 - \beta_c \cos\theta_1 + \beta_c \cos\theta_2' - \beta_c^2 \cos\theta_1 \cos\theta_2') \tag{A.2.14}$$

The energy that the particle gained in the interaction with the cloud is then:

$$\frac{\Delta E}{E} = \frac{\gamma_c^2 E_1(1 - \beta_c \cos\theta_1 + \beta_c \cos\theta_2' - \beta_c^2 \cos\theta_1 \cos\theta_2') - E_1}{E_1} \tag{A.2.15}$$

$$\frac{\Delta E}{E} = \frac{\beta_c^2 - \beta_c \cos\theta_1 + \beta_c \cos\theta_2' - \beta_c^2 \cos\theta_1 \cos\theta_2'}{1 - \beta_c^2} \tag{A.2.16}$$

This result provides information about the fractional energy gained by a single particle in a collision with a cloud. However, it is highly dependent on the angle which the CR enters and exits the cloud. The average fractional change in energy per collision is of more interest since it represents the typical behaviour of a CR particle population. It is

given by:

$$\left\langle \frac{\Delta E}{E} \right\rangle = \frac{\beta_c^2 - \beta_c \langle \cos\theta_1 \rangle + \beta_c \langle \cos\theta_2' \rangle - \beta_c^2 \langle \cos\theta_1 \rangle \langle \cos\theta_2' \rangle}{1 - \beta_c^2} \tag{A.2.17}$$

Since the scattering processes which the CR undergoes within the cloud result in a random exit angle in the cloud frame the average exit angle will be zero ($\langle \cos\theta_2' \rangle$). Thus the average fraction change in energy per collision becomes:

$$\left\langle \frac{\Delta E}{E} \right\rangle = \frac{\beta_c^2 - \beta_c \langle \cos\theta_1 \rangle}{1 - \beta_c^2} \tag{A.2.18}$$

To obtain an expression for $\langle \cos\theta_1 \rangle$ consider a situation where a population of CRs with a speed v travel in a direction that is at an angle θ_1 to the cloud's direction of travel. Suppose at $t = 0$, a CR is at position P and the cloud is at O. After a certain amount of time t, the particle collides with the cloud at position C at an angle of θ_1. The distance travelled by the CR and the cloud will be vt and $V_c t$ respectively. Any other particles which started along the line between P and O, length L, will have collided with the cloud during the time interval t. Using the cosine rule, the length of L can be found.

$$L = \sqrt{v^2 + V_c^2 - 2V_c v \cos\theta_1}\, t \tag{A.2.19}$$

Assuming that the velocity of the cloud is much less than the velocity of the CR and by applying the binomial expansion of the square root, the length of L can be approximated as:

$$L \approx (v - V_c \cos\theta_1)t \tag{A.2.20}$$

Thus, if the number density of CRs is n_{CR} and the cross-sectional area of the cloud is assumed to be spherical then the collision rate of CRs on the cloud along a line is given by R:

$$R = \frac{n_{CR} L \sigma}{t} = n_{CR}(v - V_c \cos\theta_1)\sigma \tag{A.2.21}$$

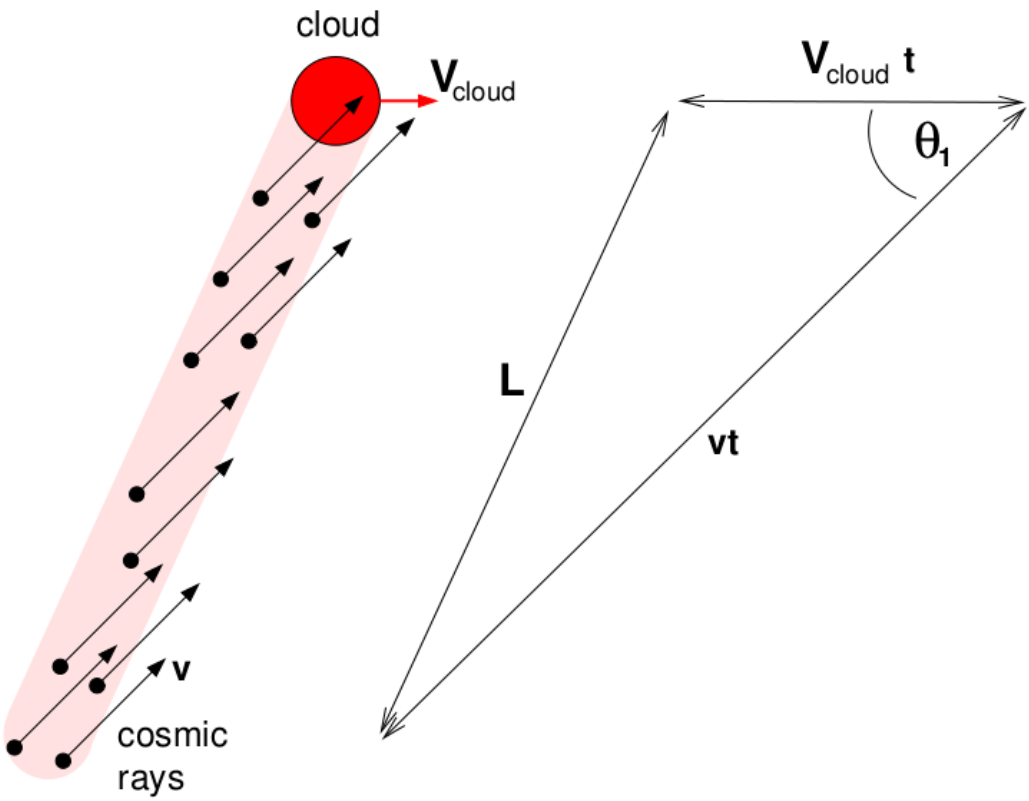

Figure 1.1: CR collision with cloud image (Protheroe)

This can then be extended to an isotropic distribution of CRs represented by:

$$\frac{dn_{CR}}{d\cos\theta_1} = \frac{n_{CR}}{2} \tag{A.2.22}$$

while $-1 < \cos\theta_1 < 1$. Taking this to be the number density of CRs and integrating the result from the linear distribution of CRs, the collision rate for an isotropic distribution can be derived:

$$R = \frac{n_{CR}}{2}\sigma \int_{-1}^{1} (v - V_c \cos\theta_1)\, d\cos\theta_1 \tag{A.2.23}$$

Assuming that the velocity of the particle tends towards the speed of light and that $V_c = \beta_c c$, the probability distribution $P(\cos\theta_1)$ of $\cos\theta_1$ can be written as:

$$P(\cos\theta_1) \propto 1 - \beta_c \cos\theta_1, \qquad -1 < \cos\theta_1 < 1 \tag{A.2.24}$$

Thus, it is possible to derive the average value of $\cos\theta_1$:

$$\langle\cos\theta_1\rangle = \frac{\int_{-1}^{1}\cos\theta_1 P(\cos\theta_1)\ d\cos\theta_1}{\int_{-1}^{1}P(\cos\theta_1)\ d\cos\theta_1} \tag{A.2.25}$$

$$\langle\cos\theta_1\rangle = \frac{\int_{-1}^{1}\cos\theta_1(1-\beta_c\cos\theta_1)\ d\cos\theta_1}{\int_{-1}^{1}(1-\beta_c\cos\theta_1)\ d\cos\theta_1} \tag{A.2.26}$$

$$\langle\cos\theta_1\rangle = -\frac{\beta_c}{3} \tag{A.2.27}$$

This result can then be substituted back into the average fractional change in energy per collision to obtain:

$$\left\langle\frac{\Delta E}{E}\right\rangle = \frac{\beta_c^2+\frac{\beta_c^2}{3}}{1-\beta_c^2} \tag{A.2.28}$$

A.3 Diffusive Shock Acceleration Theory Derivation

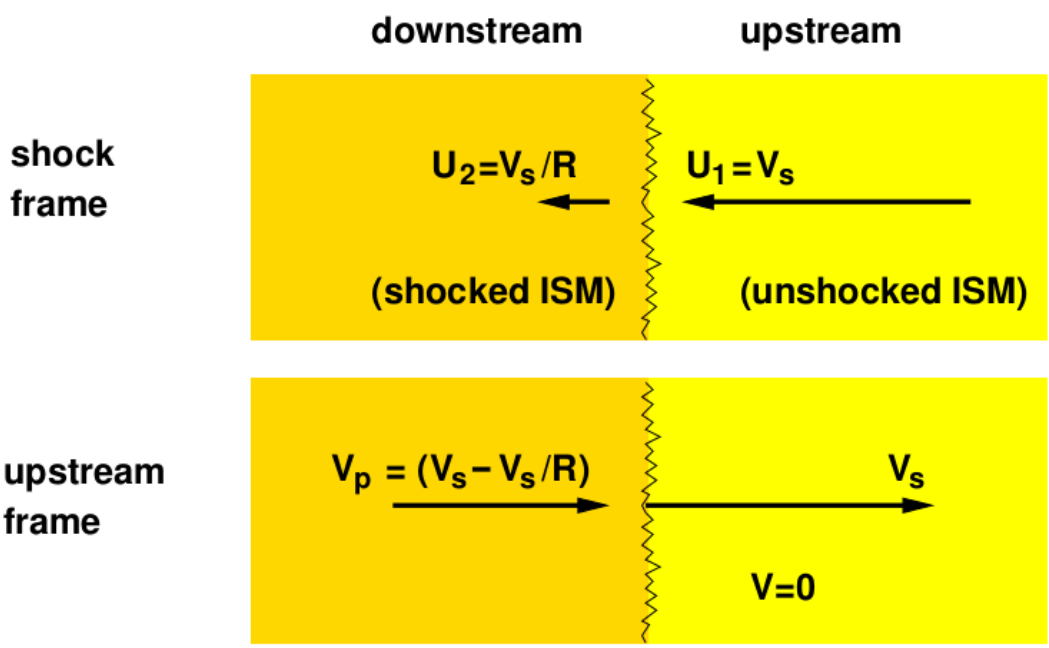

Figure 1.2: Diffusive shock acceleration for shock front (Protheroe).

Consider the reference frames of the shock and the unshocked ISM. An observer would be positioned in the unshocked frame assuming there is negligible bulk motion of the ISM. In the unshocked frame, the shock travels at a speed V_S while the ISM has no overall

velocity. In the shock frame, the ISM (density of ρ_{ISM}) moves towards the shock with a velocity $U_1 = V_S$. The shocked medium (density of ρ_s) moves away from the shock (in the same direction as the ISM) at velocity U_2. Applying conservation of momentum on either side of the shock implies:

$$\rho_s U_2 = \rho_{ISM} U_1 \tag{A.3.29}$$

$$U_1 = \frac{\rho_{ISM}}{\rho_s} U_2 = R U_2 \tag{A.3.30}$$

Thus the velocity of the shocked ISM is given by:

$$U_2 = \frac{V_S}{R} \tag{A.3.31}$$

In the unshocked frame, the velocity of the shocked ISM is given by:

$$V_P = U_1 - U_2 \tag{A.3.32}$$

The expressions for U_1 and U_2 can be substituted into this equation:

$$V_P = V_S - \frac{V_S}{R} \tag{A.3.33}$$

Thus the ratio of the shocked ISM to the pre-shocked ISM can be written:

$$\frac{V_S}{V_P} = \frac{R}{R-1} = \frac{4}{3} \; (R = 4) \tag{A.3.34}$$

Now, suppose there are magnetic irregularities on either side of the shock which the CRs can scatter off. These could be objects such as magnetised clouds, similar to the situation in Fermi's original theory. It is assumed that the shocked matter is moving at speeds less than the speed of light ($V_P << c$). This is a reasonable assumption since it it not possible for a supernova to accelerate particles to such high energies based on the explosion mechanism alone (Ouellette et al., 2007). In the ISM frame, any scattering events of CRs off of the magnetised clouds will result in no change in energy due to the

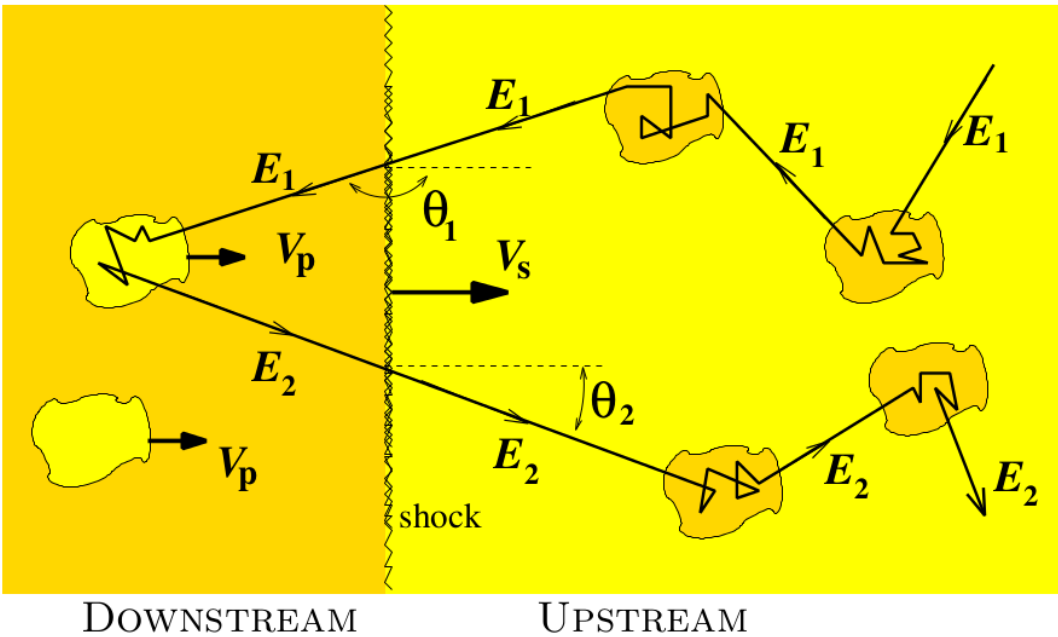

Figure 1.3: Diffusive shock acceleration with magnetic irregularities. (Protheroe)

collisionless nature of the interaction. The CR crosses the shock at an angle of θ_1 and exits at an angle of θ_2. Scattering events in the shocked frame will result in a change in energy since the interaction is no longer elastic. For a CR number density of n_{CR} and speed v, the rate at which the particles from the unshocked ISM (upstream) into the shocked region (downstream) is given by:

$$R_{u\to d}(\theta_1)d\cos\theta_1 \approx -n_{CR}v\cos\theta_1 d\cos\theta_1 \tag{A.3.35}$$

Similarly, the rate which particles cross from downstream to upstream is given by:

$$R_{d\to u}(\theta_2')d\cos\theta_2' \approx n_{CR}v\cos\theta_2' d\cos\theta_2' \tag{A.3.36}$$

Thus, the probability density functions, $P(\cos\theta_1)$ and $P(\cos\theta_2')$ are proportional to $-\cos\theta_1$ and $cos\theta_2'$. Then the average angle which CRs cross downstream of the shock for an isotropic distribution is derived in the following method:

$$\langle\cos\theta_1\rangle = \frac{\int_{-1}^{0} P(\cos\theta_1)\cos\theta_1\ d\cos\theta_1}{\int_{-1}^{0} P(\cos\theta_1)\ d\cos\theta_1} \tag{A.3.37}$$

$$\langle \cos\theta_1 \rangle = \frac{-\int_{-1}^{0} \cos^2\theta_1 \; d\cos\theta_1}{-\int_{-1}^{0} \cos\theta_1 \; d\cos\theta_1} \tag{A.3.38}$$

$$\langle \cos\theta_1 \rangle = -\frac{2}{3} \tag{A.3.39}$$

Similarly, the average angle of an isotropic distribution of CRs crossing upstream of the shock is given by:

$$\langle \cos\theta_2' \rangle = \frac{2}{3} \tag{A.3.40}$$

Recalling the equation for the average fractional change in energy per collision from Fermi's original theory, the average angles from diffusive shock acceleration can be substituted in along with the Lorentz factor of the shocked clouds, $\beta_P = \frac{V_P}{c}$:

$$\left\langle \frac{\Delta E}{E} \right\rangle = \frac{\beta_P^2 - \beta_P \langle \cos\theta_1 \rangle + \beta_P \langle \cos\theta_2' \rangle - \beta_P^2 \langle \cos\theta_1 \rangle \langle \cos\theta_2' \rangle}{1 - \beta_P^2} \tag{A.3.41}$$

$$\left\langle \frac{\Delta E}{E} \right\rangle = \frac{\frac{4}{3}\beta_P + \frac{13}{9}\beta_P^2}{1 - \beta_P^2} \tag{A.3.42}$$

A.4 Neutral Pion Derivations

Assuming that the low energy proton is at rest, the minimum energy of the cosmic-ray proton can be calculated using conservation of momentum. The 4-momentum of the stationary proton is $(m_p c,\ 0,\ 0,\ 0)$ while the 4-momentum of the cosmic-ray proton is $\left(\frac{E_p}{c},\ \vec{p}_p\right)$:

$$\Rightarrow E = (m_p c^2 + E_p)^2 - \vec{p}_p^{\,2} c^2 \tag{A.4.43}$$

$$\Rightarrow E = E_p^2 + 2 m_p c^2 E_p + m_p^2 c^4 - \vec{p}_p^{\,2} c^2 \tag{A.4.44}$$

$$\Rightarrow E = m_p^2 c^4 + 2 m_p c^2 E_p + m_p^2 c^4 \tag{A.4.45}$$

$$\Rightarrow E = 2 m_p c^2 (E_p + m_p c^2) \tag{A.4.46}$$

$$\Rightarrow E_{th} < 2 m_p c^2 (E_p + m_p c^2) \tag{A.4.47}$$

$$\Rightarrow E_p > \frac{E_{th}}{2m_pc^2} - m_pc^2 \tag{A.4.48}$$

$$\Rightarrow E_p > 1.218\ GeV \tag{A.4.49}$$

For a proton travelling a a speed of v, where the density is n_H and the inelastic cross section is σ_{pp} which is dependent on the momentum (p) of the proton, the rate inelastic interactions will be given by $n_H\sigma_{pp}(p)\beta c$. The inelastic cross section increases as the energy of the cosmic-ray proton increases since there is more energy available in an interaction to create a pion. Therefore, the interaction rate increases as the proton has more energy. Note that the number of neutral pions produced in an interaction increases once the energy of the CR proton is large enough. This means that the rate at which neutral pions are produced is the product of the rate of inelastic interactions and the multiplicity or mean number of pions produced. This is incorporated into the cross section which becomes $\sigma_{\pi^o,inclusive}$. This cross section still increases at the proton momentum increases. Assuming that there is a number density, n_H, of stationary hydrogen atoms and that the energy distribution of neutral pions of energy E_π produced by a single CR proton of energy E_p is given by $f(E_\pi,\ E_p)$, an equation for the rate of neutral pions produced by a proton can be derived:

$$R_{\pi_o}(E_\pi,\ E_p) \approx n_H\sigma_{\pi^o,inclusive}(E_p)\beta_p c f(E_\pi,\ E_p) \tag{A.4.50}$$

Then the rate of production of neutral pions per unit energy per unit volume is derived by assuming that there are $N_p(E_p)dE_p$ CR protons per unit volume with energies in the range of E_p to $E_p + dE_p$:

$$\Rightarrow Q_{\pi^o}(E_\pi) = \int_{E_p^{th}}^{\infty} R_{\pi_o}(E_\pi,\ E_p)N_p(E_p)\ dE_p \tag{A.4.51}$$

$$\Rightarrow Q_{\pi^o}(E_\pi) \approx n_H \int_{E_p^{th}}^{\infty} \sigma_{\pi^o,inclusive}(E_p)\beta_p c f(E_\pi,\ E_p)N_p(E_p)\ dE_p \tag{A.4.52}$$

The neutral pions produced by the interaction then will decay after a short time period. The preferred decay channel is through the production of two gamma-rays. Therefore, the production rate of gamma-rays is double the production rate of neutral pions. The decay of a neutral pion must result in at least two gamma-rays since momentum needs to be conserved. Thus if the pion is at rest, two gamma-rays of equal energy are emitted in opposite directions. The energy of the gamma-rays produced in this scenario is half that of the rest mass energy of the neutral pion ($m_{\pi^o}c^2 = 135$ MeV). Therefore, the energy of the gamma-rays is $E_\gamma = \frac{1}{2}m_{\pi^o}c^2 = 67.5$ MeV.

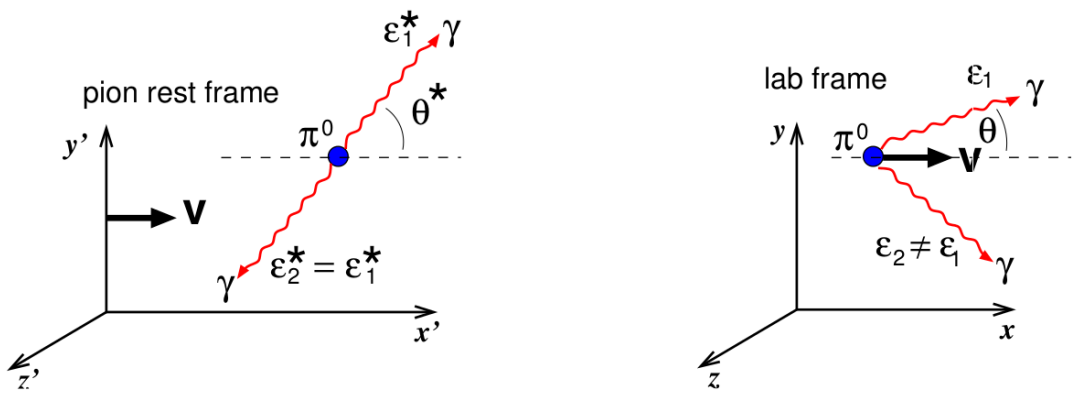

Figure 1.4: Neutral Pion decay into gamma-rays at rest. (Protheroe)

In the case that the pion is not at rest the gamma-rays no longer need to be emitted in opposite directions with equal energy in order to conserve momentum. It is assumed that the pion has an energy of $E_\pi = \gamma_\pi m_{\pi^o}c^2$ travelling in the x direction with a velocity of $v_\pi = \beta_\pi c$. In the rest frame of the pion, it decays into two gamma-rays each with an energy E'_{γ^1} and E'_{γ^2} which are equal. One of the gamma-rays is emitted at an angle of θ' above the x axis. Therefore, to conserve momentum, the second gamma-ray must be emitted at an angle of $\pi - \theta'$ with respect to the x axis. The energies of the gamma-rays in the observer's frame are E_{γ^1} and E_{γ^2} with angles of θ_1 and θ_2 respectively.

When taking the Lorentz transform of the momenta in the primed frame, only the component of momentum in the direction of the pion's velocity needs to be considered. Hence, the energy of the first gamma-ray that is transformed will be $E'_{\gamma^1 x} = E'_{\gamma^1}\cos\theta'$. Therefore,

the energy of the gamma-ray in the observer's frame is the Lorentz transform of this:

$$E_{\gamma^1} = \gamma_\pi (E'_{\gamma^1} + \beta_\pi E'_{\gamma^1} \cos\theta') \tag{A.4.53}$$

In the rest frame of the pion, the decay process is isotropic since the spin of the pion is zero. Thus, the spectrum of gamma-rays produced is symmetric around a central energy ϵ_γ. The probability density for an isotropic distribution is described by the following equation:

$$\frac{dP}{d\Omega'} = \frac{dP}{\sin\theta' d\theta' d\phi'} \tag{A.4.54}$$

$$\Rightarrow \frac{dP}{d\Omega'} = \frac{1}{2\pi}\frac{dP}{d\cos\theta'} \tag{A.4.55}$$

$$\Rightarrow \frac{dP}{d\Omega'} = \frac{1}{4\pi} \tag{A.4.56}$$

$$\Rightarrow \frac{dP}{d\cos\theta'} = \frac{1}{2} \tag{A.4.57}$$

Then the energy distribution in the observer's frame can be derived using the probability distribution of gamma-rays in the pion's rest frame. To account for the production of two gamma-rays, a factor of 2 needs to be included in the equation:

$$\frac{dP}{dE_\gamma} = 2\frac{dP}{d\cos\theta'}\left(\frac{d\cos\theta'}{dE_\gamma}\right) \tag{A.4.58}$$

Recalling the expression for the energy of the gamma-rays in the observer's frame, $E_\gamma = \gamma_\pi(E'_\gamma + \beta_\pi E'_\gamma \cos\theta')$ the derivative with respect to $d\cos\theta'$ can be found:

$$\frac{dE_\gamma}{d\cos\theta'} = \gamma_\pi \beta_\pi E'_\gamma \tag{A.4.59}$$

The energy of the pion in the observer's frame will vary between $\gamma_\pi E'_\gamma(1-\beta_\pi)$ and $\gamma_\pi E'_\gamma(1+\beta_\pi)$ since $\cos\theta'$ takes on values in $[-1, 1]$:

$$\Rightarrow \frac{dP}{dE_\gamma} = 2\frac{1}{2}\frac{1}{\gamma_\pi\beta_\pi E'_\gamma} = \frac{1}{\gamma_\pi\beta_\pi E'_\gamma}, \qquad \gamma_\pi E'_\gamma(1+\beta_\pi) < E_\gamma < \gamma_\pi E'_\gamma(1-\beta_\pi) \tag{A.4.60}$$

$$\Rightarrow \frac{dP}{dE_\gamma} = \frac{1}{\gamma_\pi \beta_\pi E'_\gamma}, \qquad E'_\gamma \sqrt{\frac{1-\beta_\pi}{1+\beta_\pi}} < E_\gamma < E'_\gamma \sqrt{\frac{1+\beta_\pi}{1-\beta_\pi}} \tag{A.4.61}$$

The minimum pion energy required to produce gamma-rays with energies greater than 67.5 MeV can be found using the energy range requirements:

$$E_\gamma < E'_\gamma \sqrt{\frac{1+\beta_\pi}{1-\beta_\pi}} \tag{A.4.62}$$

$$\Rightarrow \beta_\pi^{min}(E_\gamma) = \frac{|E_\gamma^2 - E_\gamma'^2|}{E_\gamma^2 + E_\gamma'^2} \tag{A.4.63}$$

$$\Rightarrow \gamma_\pi^{min} = \frac{1}{\sqrt{1 - [\beta_\pi^{min}(E_\gamma)]^2}} \tag{A.4.64}$$

$$\Rightarrow E_\pi^{min}(E_\gamma) = \gamma_\pi^{min} m_{\pi^o} c^2 \tag{A.4.65}$$

Thus, the spectrum of gamma-rays produced by pions with energies greater than E_π^{min} is given by the integral over pion energy of the energy distribution of gamma-rays multiplied by the production spectrum of pions:

$$Q_\gamma(E_\gamma) = \int_{E_\pi^{min}}^{\infty} \frac{1}{\gamma_\pi(E_\pi)\beta_\pi(E_\pi)E'_\gamma} Q_{\pi^o}(E_\gamma)\ dE_\pi \tag{A.4.66}$$

A.5 Equation of Radiative Transfer

Emission which travels through space can encounter many gaseous features before it is observed. Thus, a theory is needed which describes the process of radiation absorption and emission when a gas feature is encountered. It is assumed that the initial radiation has an intensity of I_ν. This radiation then encounters a gas feature which is approximated by a cylinder of length ds and circular area of dA. Thus, the volume of this feature is $dV = dA\ ds$. Within the cylinder, there gas has a number density of n which means that the number of particles is $N = n\ dV$. Each of the particles can absorb the incident radiation where the cross section of such an event occurring is given by σ_ν.

It is assumed that the length of the cylinder is small enough so that none of the cross

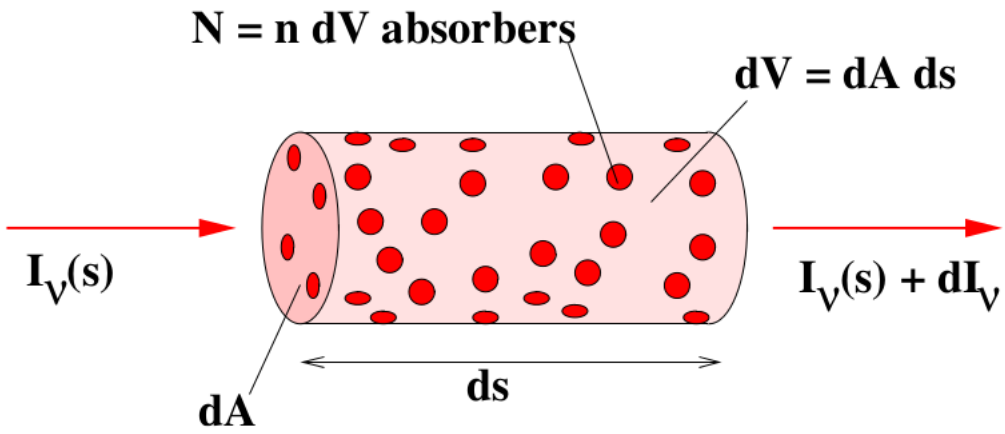

Figure 1.5: Diagram showing radiation being absorbed by cloud

sectional area of the particles overlap on a two dimensional projection onto the plane perpendicular to the direction of the radiation. Thus, the area where the radiation is absorbed is given by $N\sigma_\nu = n\ ds\ dA\ \sigma_\nu$. The fraction of the incident radiation absorbed is then given by the ratio of the absorbing area and the total area:

$$\frac{N\sigma_\nu}{dA} = n\sigma_\nu ds \tag{A.5.67}$$

Therefore, the change in intensity due to absorption within the cylinder is given by:

$$dI_\nu = -n\sigma_\nu I_\nu ds \tag{A.5.68}$$

Some other quantities can be defined from this equation. The absorption coefficient which measures the area of the target per unit volume is defined as:

$$\kappa_\nu = n\sigma_\nu \tag{A.5.69}$$

The absorption coefficient can also be expressed as a function of the Einstein coefficients and the line profiles of the absorbed and emitted spectral lines. These line profiles are

assumed to be equal and are normally described by a Gaussian function:

$$\kappa_\nu = \frac{h\nu_{ul}}{4\pi}(n_l B_{lu} - n_u B_{ul})\varphi(\nu) \tag{A.5.70}$$

The emission coefficient can also be defined in terms of the Einstein coefficients:

$$\epsilon_\nu = \frac{h\nu_{ul}}{4\pi} n_u A_{ul}\varphi(\nu) \tag{A.5.71}$$

The average length that the radiation will travel before it undergoes an interaction is given by the absorption mean free path and it defined as:

$$l_\nu = \frac{1}{\kappa_\nu} = \frac{1}{n\sigma_\nu} \tag{A.5.72}$$

In addition to the absorption of the radiation by the particles within the cylinder, they also may emit radiation. The amount of energy that the particles radiate can be quantified using a quantity called the emission coefficient. It is defined as the amount of energy that travels through an volume $dV = s^2 d\Omega ds$ in a certain amount of time in a set velocity range over a solid angle where previous definitions of the terms remain true:

$$j_\nu = \frac{dE}{dV\ dt\ d\nu\ d\Omega} = \frac{dI_\nu}{ds} \tag{A.5.73}$$

That is, the emission coefficient represents the positive change in the intensity due to emission by the particles within the cylinder. Hence the equation which describes the change in intensity per distance through the cylinder is:

$$\frac{dI_\nu}{ds} = -\kappa_\nu I_\nu + j_\nu \tag{A.5.74}$$

This relation is known as the equation of radiative transfer since it described how radiation in interchanged between the environment and the cylinder of gas.

Appendix B

Integrated Gas Maps

^{13}CO

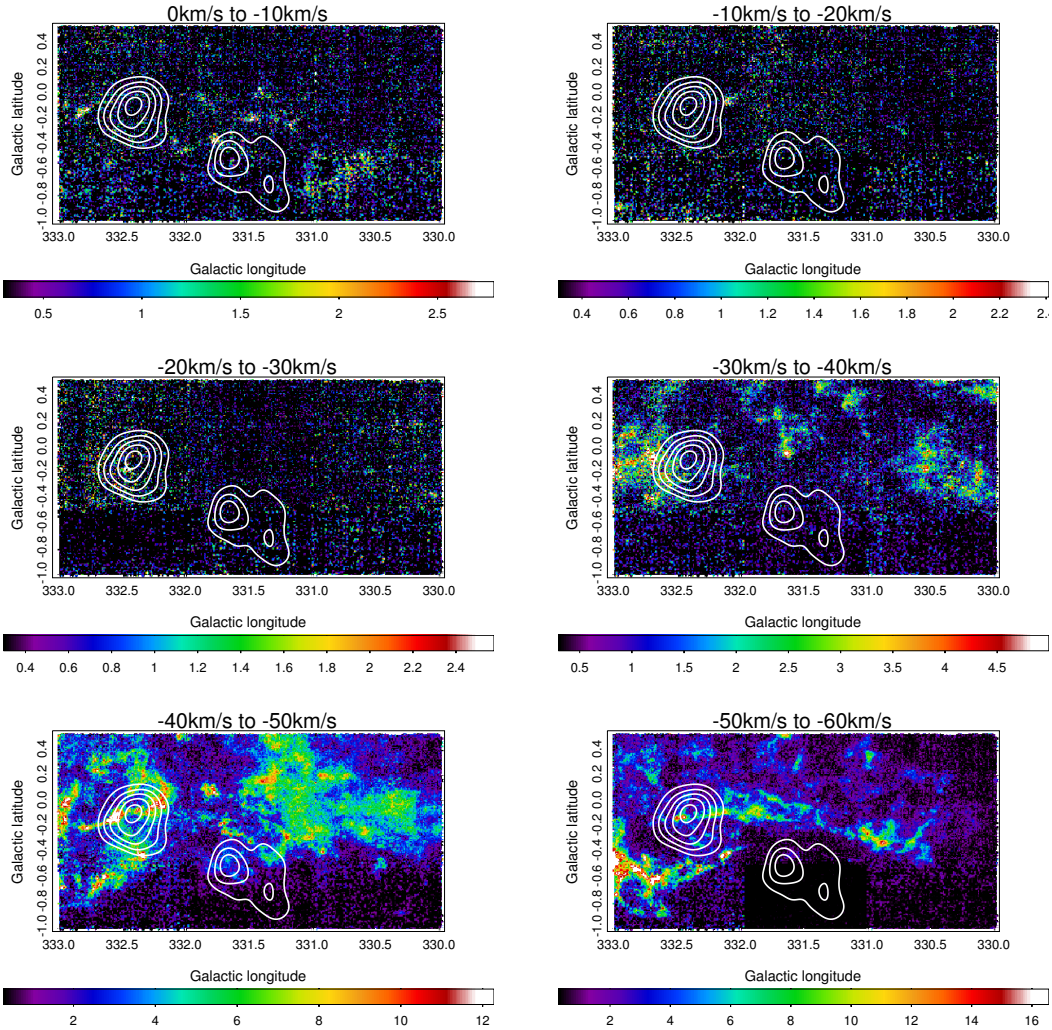

Figure 2.1: Mosaic of ^{13}CO data from the Mopra telescope.

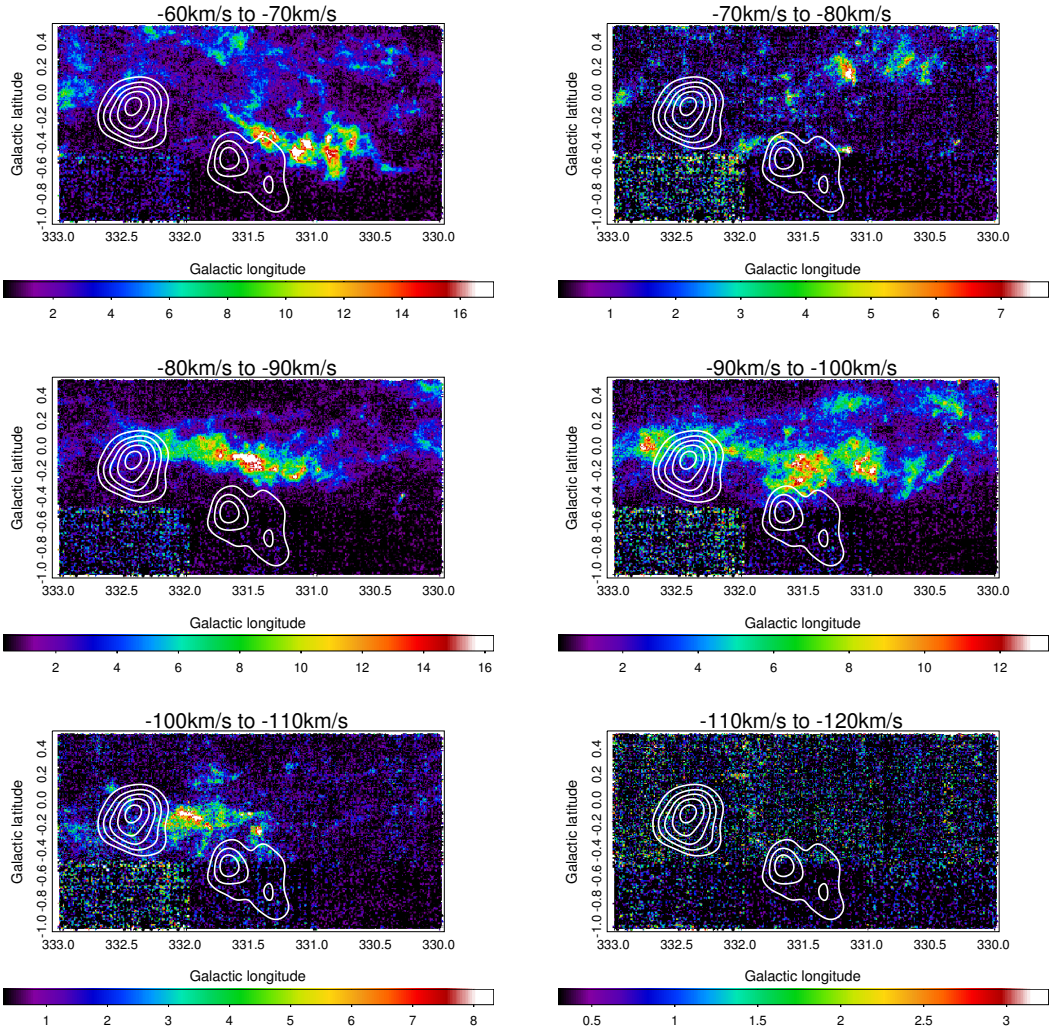

Figure 2.2: Mosaic of ^{13}CO data from the Mopra telescope.

$C^{18}O$

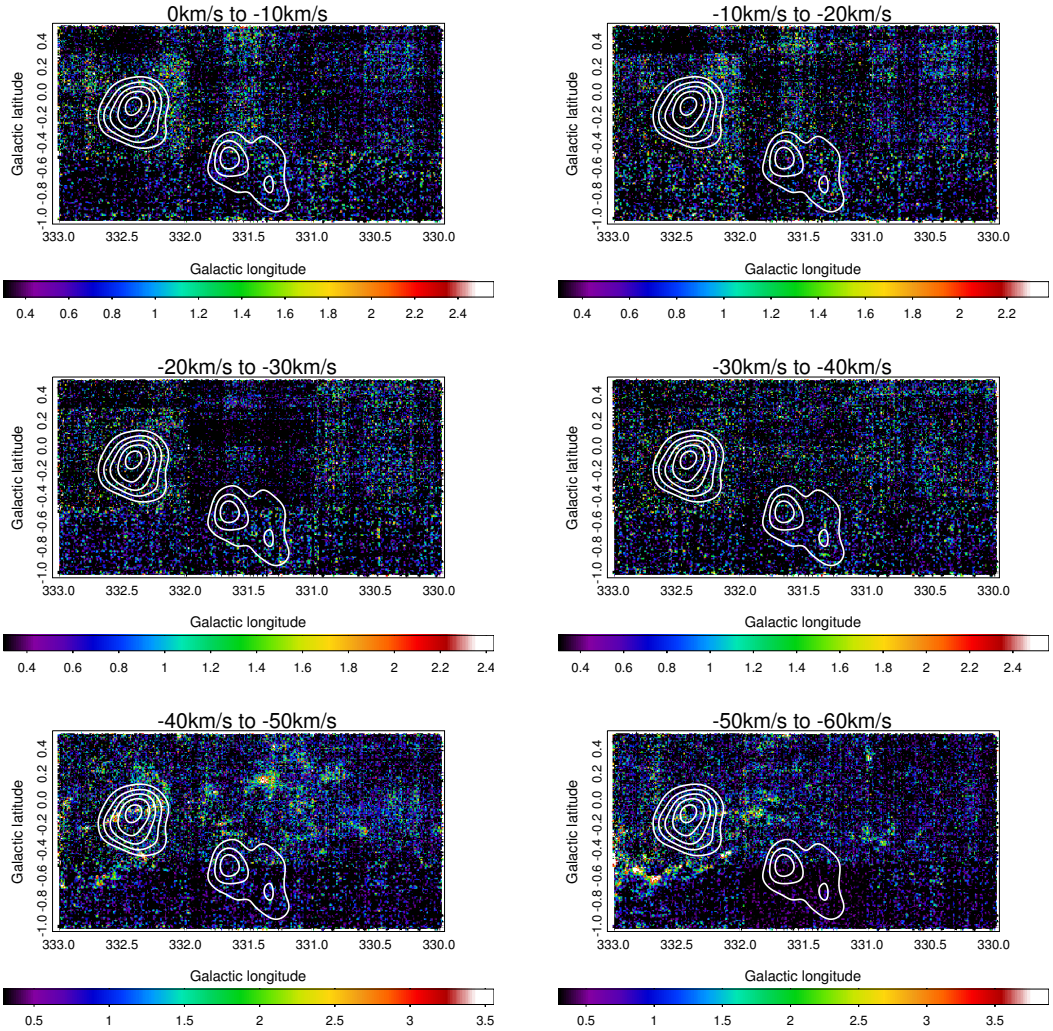

Figure 2.3: Mosaic of $C^{18}O$ data from the Mopra telescope.

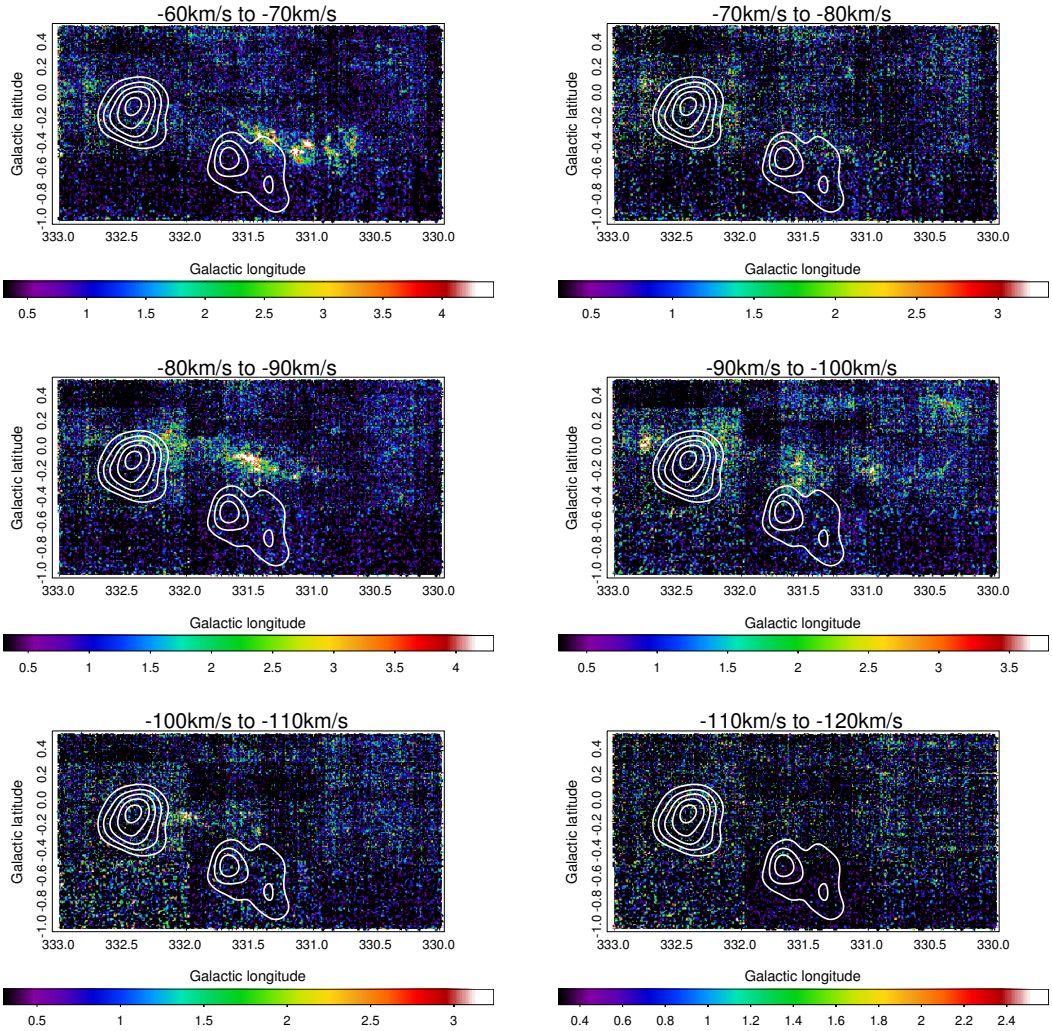

Figure 2.4: Mosaic of $C^{18}O$ data from the Mopra telescope.

$C^{34}S$ 1-0 MALT-45

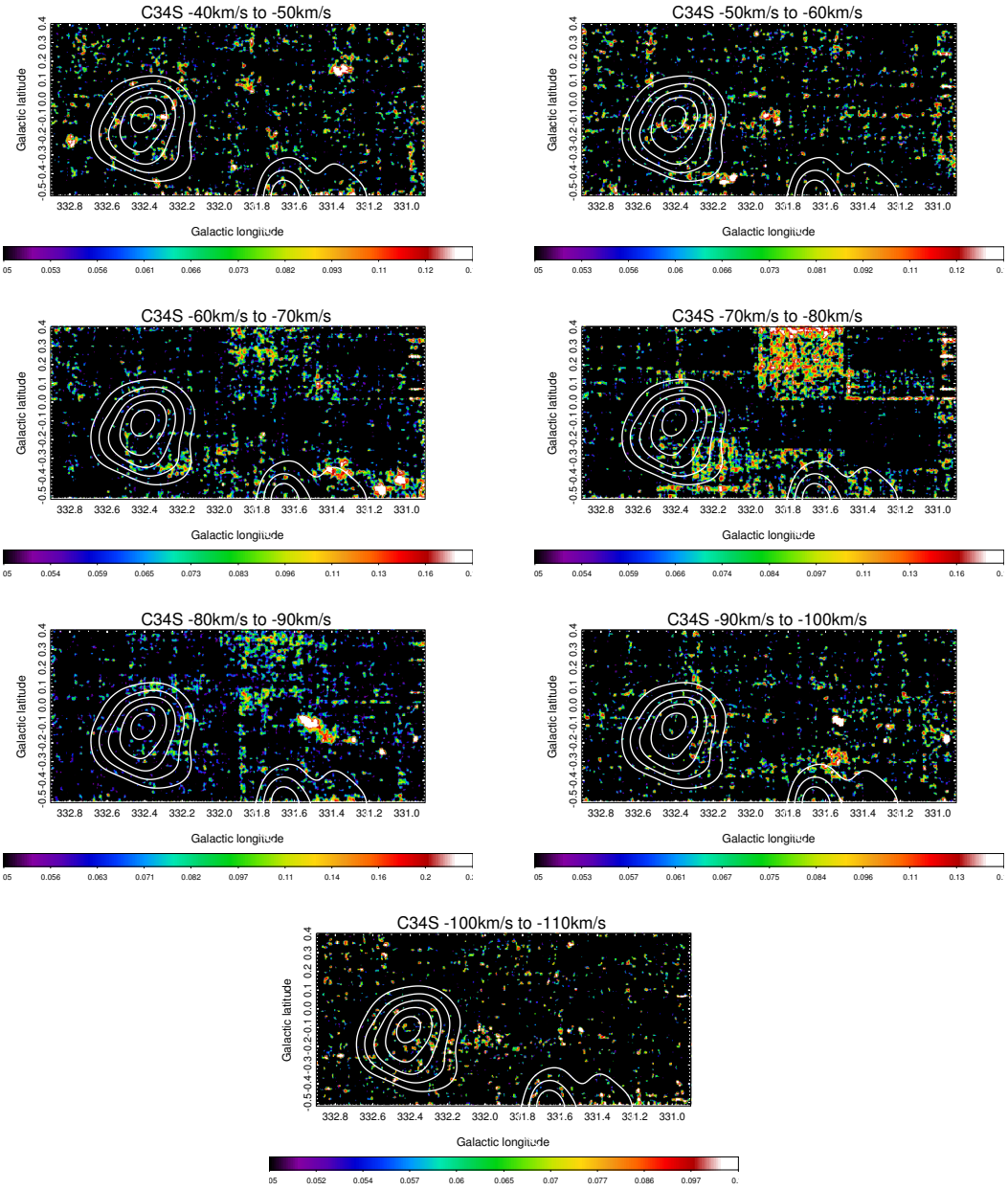

Figure 2.5: Mosaic of $C^{34}S$ data from the MALT-45 Survey.

$C^{34}S$ 1-0

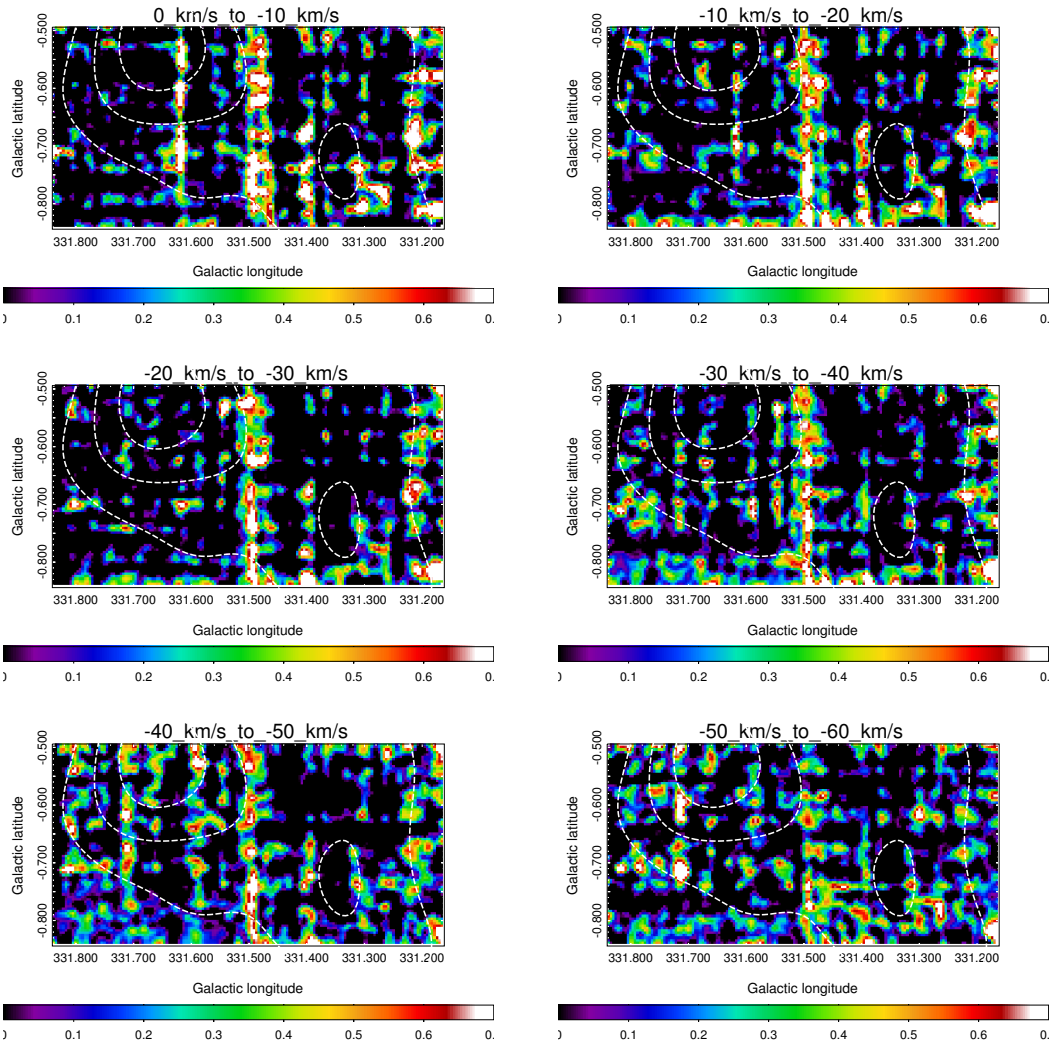

Figure 2.6: Mosaic of $C^{34}S$-1-0 data from the Mopra telescope.

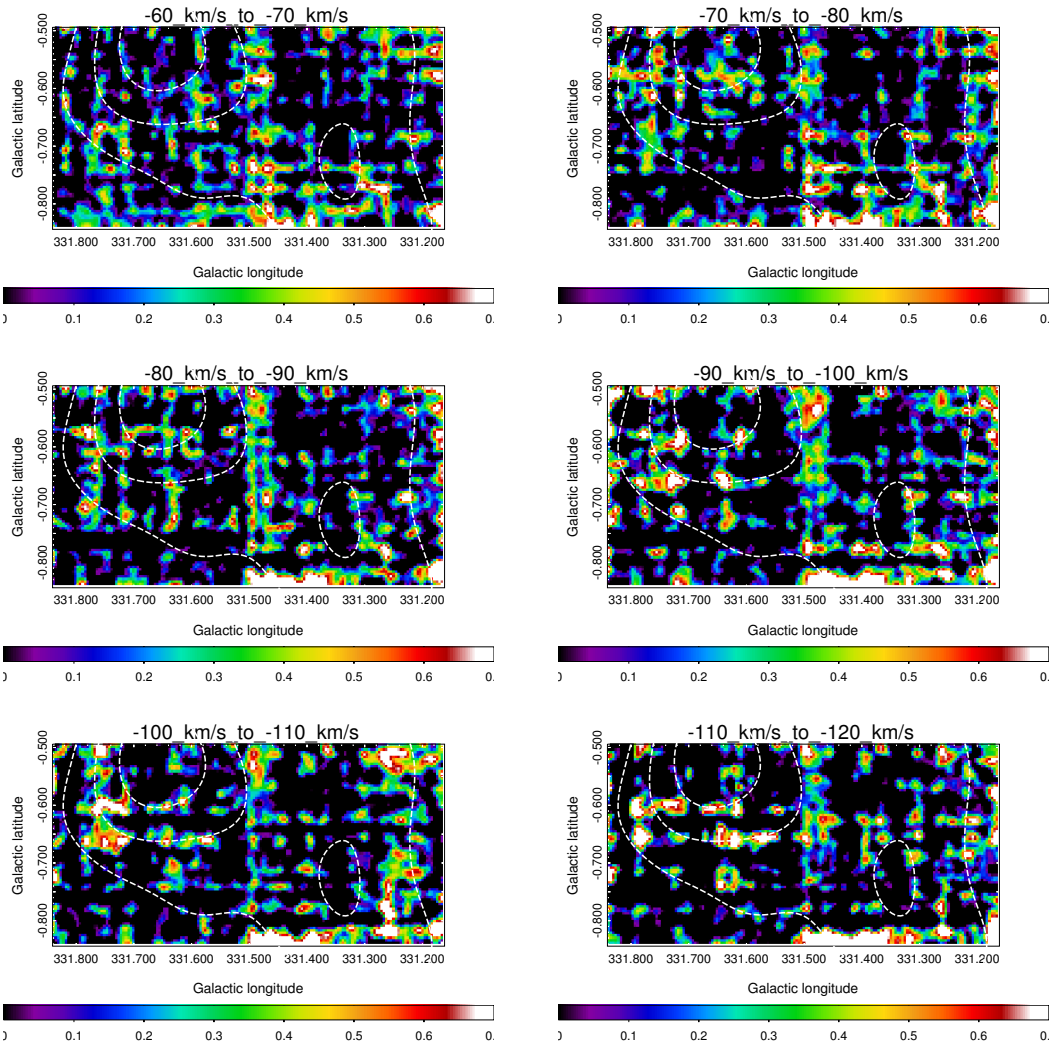

Figure 2.7: Mosaic of $C^{34}S$-1-0 data from the Mopra telescope.

SiO 1-0 MALT-45

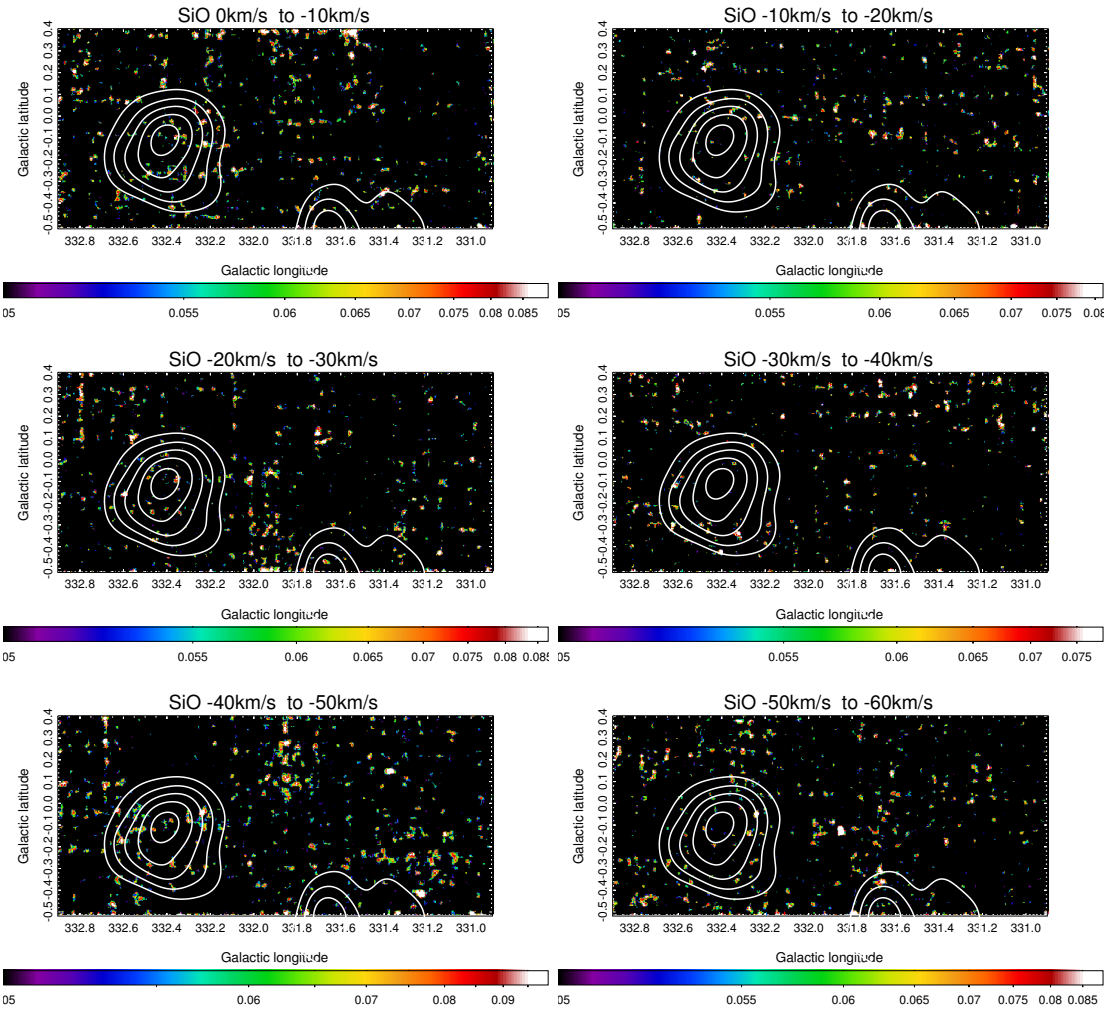

Figure 2.8: Mosaic of SiO 1-0 data from the MALT-45 Survey.

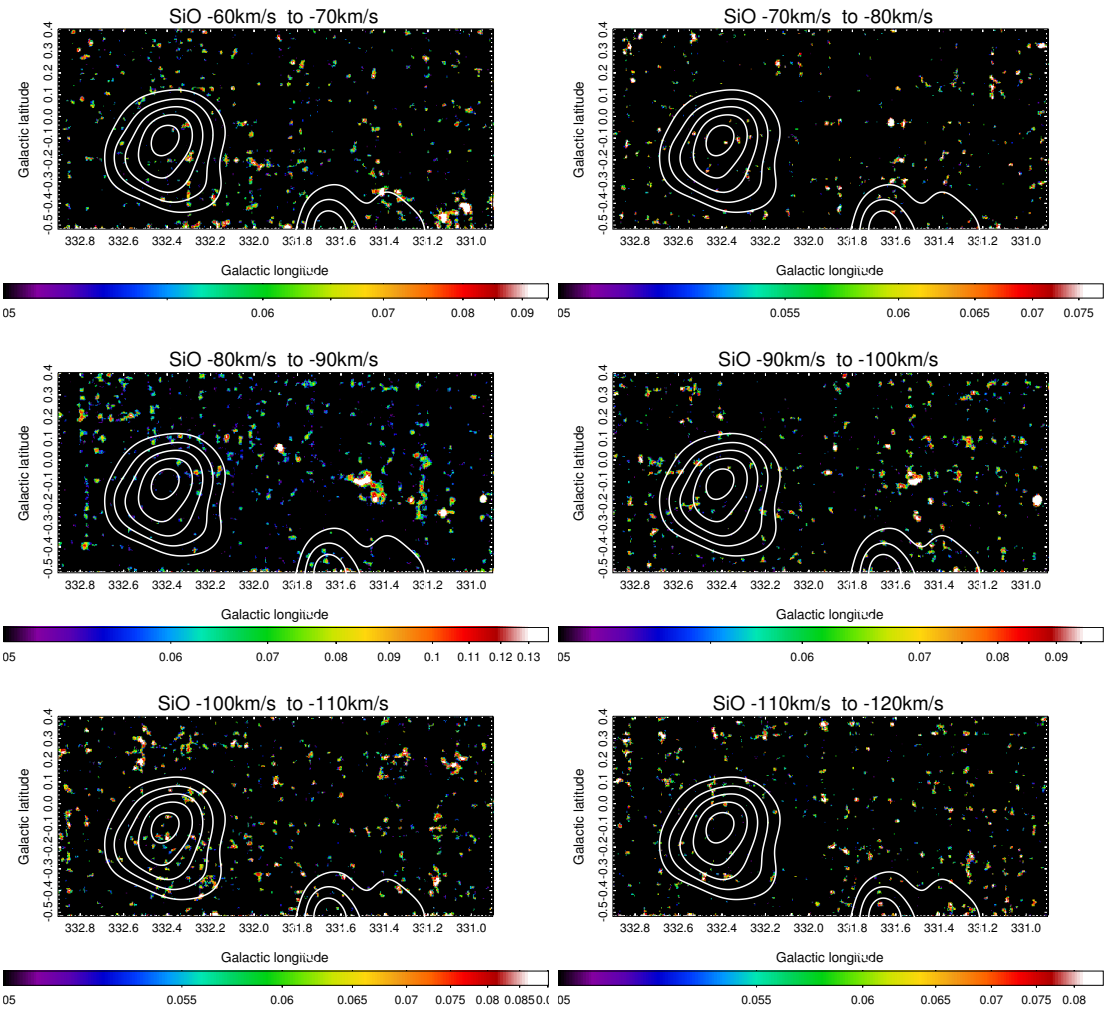

Figure 2.9: Mosaic of SiO 1-0 data from the MALT-45 Survey.

NH_3 1-1

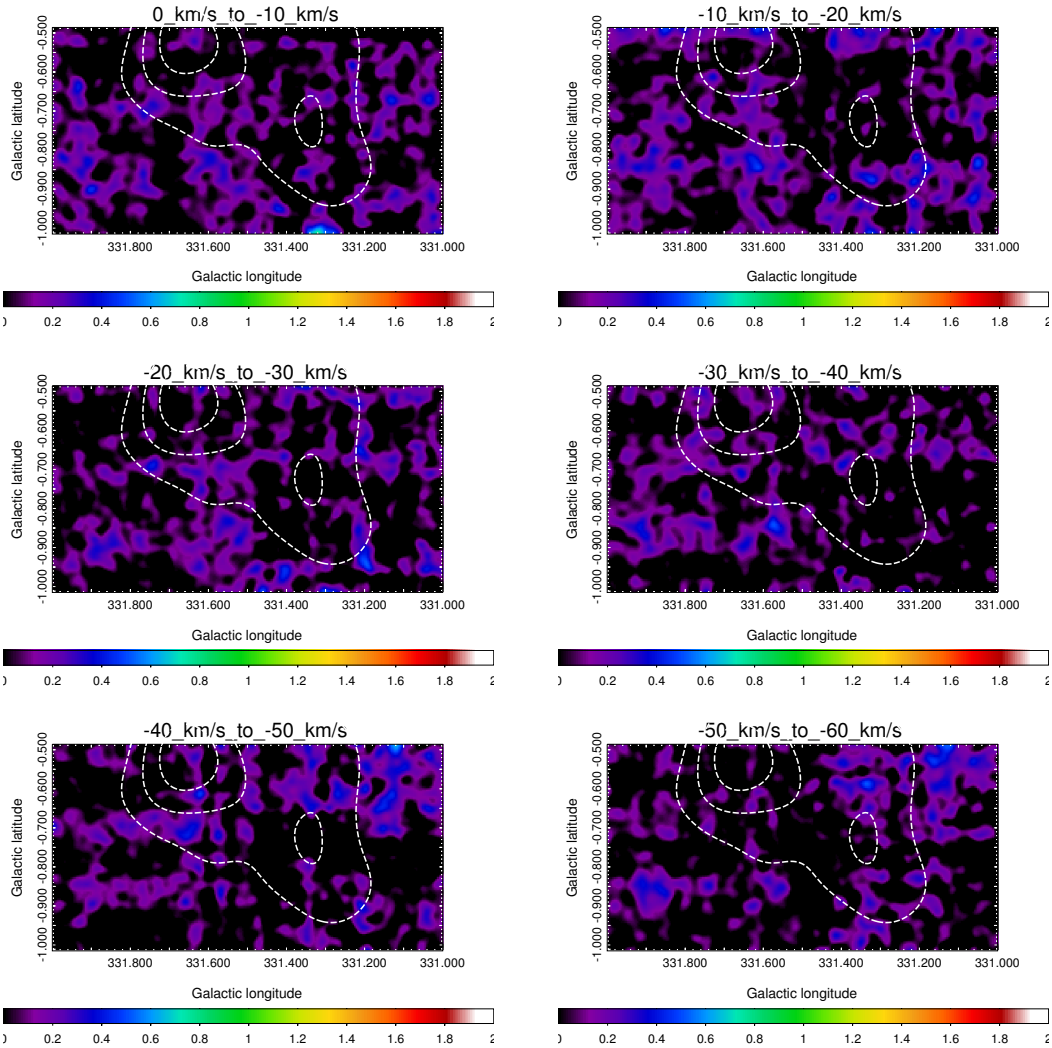

Figure 2.10: Mosaic of NH_3 1-1 data from the Mopra telescope.

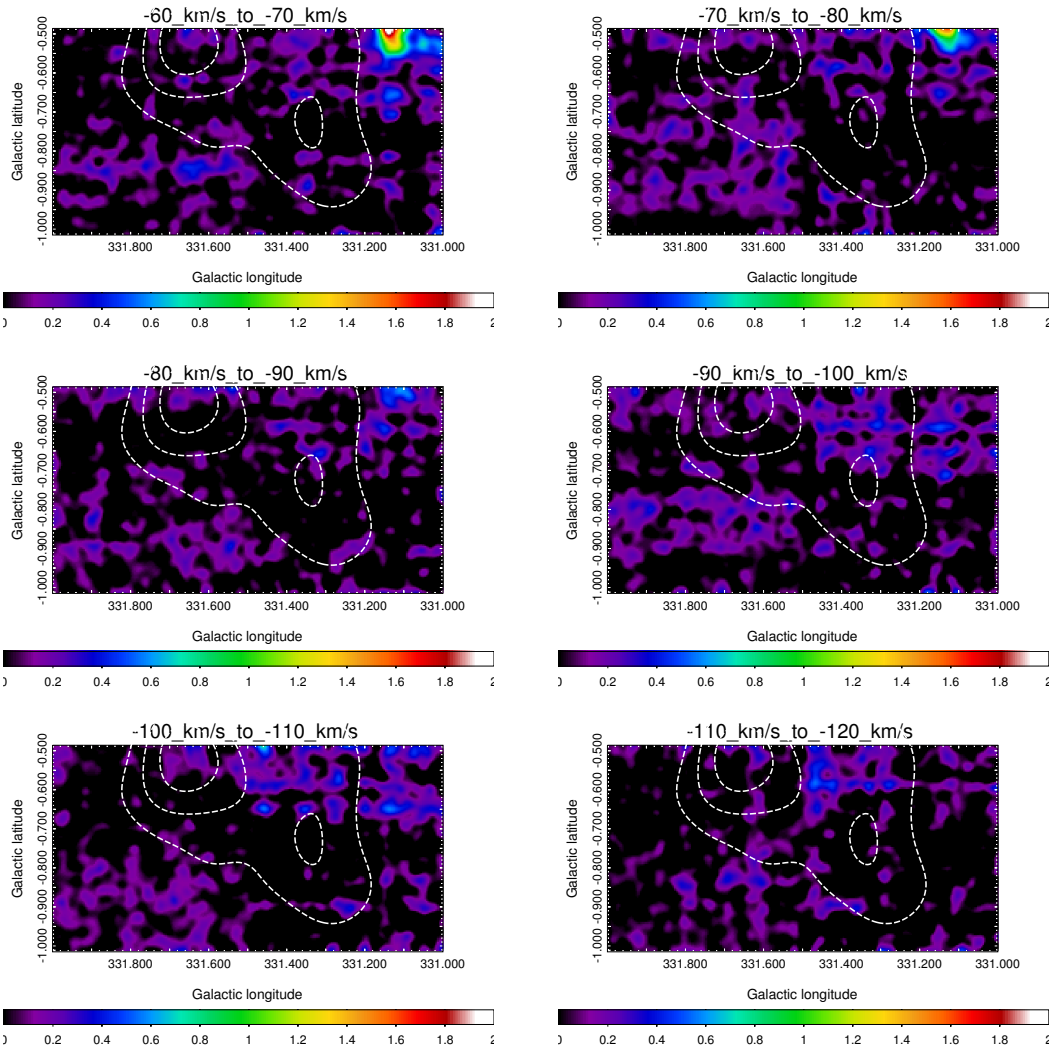

Figure 2.11: Mosaic of NH_3 1-1 data from the Mopra telescope.

Appendix C

Distances from Accelerators to Regions

C.1 Distances between RCW 103 and CO regions

The table below shows the distances between RCW 103 and the CO regions in its velocity range assuming that they are either at the near distance or the far distance.

Region	Near Distance Separation (kpc)	Far Distance Separation (kpc)
29	4.2	5.8
31	4.2	5.6
32	4.3	5.5
33	4.2	5.6
34	4.2	5.6

C.2 Distances between G332.0+0.2 and CO regions

The table below shows the distances between G332.0+0.2 and the CO regions in its velocity range assuming that they are either at the near distance or the far distance.

Region	Near Distance Separation (kpc)	Far Distance Separation (kpc)
31	4.6	5.6
32	4.6	5.5
33	4.6	5.6
34	4.6	5.6

C.3 Distances between Kes 32 and CO regions

The table below shows the distances between Kes 32 and the CO regions in its velocity range assuming that they are either at the near distance or the far distance.

Region	Near Distance Separation (kpc)	Far Distance Separation (kpc)
26	3.5	6.5
27	3.5	6.6

C.4 Distances between PSR J1617-5055 and CO regions

The table below shows the distances between PSR J1617-5055 and the CO regions in its velocity range assuming that they are either at the near distance or the far distance.

Region	Near Distance Separation (kpc)	Far Distance Separation (kpc)
29	4.1	5.8
31	4.1	5.6
32	4.2	5.5
33	4.1	5.6
34	4.1	5.6

C.5 Distances between PSR J1614-5048 and CO regions

The table below shows the distances between PSR J1614-5048 and the CO regions in its velocity range assuming that they are either at the near distance or the far distance.

Region	Near Distance Separation (kpc)	Far Distance Separation (kpc)
34	4.5	5.6

C.6 Distances between Pismis 22 and CO regions

The table below shows the distances between Pismis 22 and the CO regions in its velocity range assuming that they are either at the near distance or the far distance.

Region	Near Distance Separation (kpc)	Far Distance Separation (kpc)
1	0.8	13.9
2	0.7	13.7

C.7 Distances between WR 73-1 and CO regions

The table below shows the distances between WR 73-1 and the CO regions in its velocity range assuming that they are either at the near distance or the far distance.

Region	Near Distance Separation (kpc)	Far Distance Separation (kpc)
25	8.1	7.3

C.8 Distances between WR 74 and CO regions

The table below shows the distances between WR74 and the CO regions in its velocity range assuming that they are either at the near distance or the far distance.

Region	Near Distance Separation (kpc)	Far Distance Separation (kpc)
11	1.9	10.0

C.9 Distances between PSR J1613-5211 and CO regions

The table below shows the distances between PSR J1613-5211 and the CO regions in its velocity range assuming that they are either at the near distance or the far distance.

Region	Near Distance Separation (kpc)	Far Distance Separation (kpc)
36	4.1	5.8
37	4.2	5.5